UNIVERSITY OF CALIFORNIA
RIVERSIDE

Synthesis, Structural Characterization, and Transport Properties of Metastable Phases in the Mg-Sn System

A Dissertation submitted in partial satisfaction
of the requirements for the degree of

Doctor of Philosophy

in

Mechanical Engineering

by

Anthony Yun-Ming Fong

June 2016

Dissertation Committee:
Dr. Javier Garay, Chairperson
Dr. Reza Abbaschian
Dr. Lorenzo Mangolini

The Dissertation of Anthony Yun-Ming Fong is approved:

_____

_____

_____
Committee Chairperson

University of California, Riverside

Acknowledgements

I dedicate this thesis to my family for their unwavering support in my educational endeavors. None of this would be possible without them.

I thank my thesis advisor, Dr. Javier Garay, for his support in shaping my scientific outlook and approach. I would also like to thank my collaborators at: Los Alamos National Laboratory, Drs. Xu, Dirmeyer, and Obrey; The National Institute of Advanced Industrial Science and Technology, Dr. Murata; and Oak Ridge National Laboratory, Dr. Page. Finally, I thank my labmates with whom we have shared many academic struggles and triumphs together and are always stronger because of them.

This work was supported by the Department of Energy, without which, none of these studies would be possible. Chapter 3 contains work (Synthesis and structural characterization of dense polycrystalline Mg_9Sn_5, a metastable Mg-Sn phase) previously published (2014) in the Journal of Alloys and Compounds.

ABSTRACT OF THE DISSERTATION

Synthesis, Structural Characterization, and Transport Properties of Metastable Phases in the Mg-Sn System

by

Anthony Yun-Ming Fong

Doctor of Philosophy, Graduate Program in Mechanical Engineering
University of California, Riverside, June 2016
Dr. Javier Garay, Chairperson

Mg-Sn alloys have many uses due to their relative elemental abundance, low toxicity and low densities. Some applications include thermoelectric energy conversion, hydrogen storage, and enhancement of structural alloys. The thermoelectric application is of particular interest because Mg-Sn-Si based materials have shown promise in recent years.

It is well accepted that materials structure-property relationships are at the root of the improvement of a device's performance. Due to the interdependence of the transport properties, research for efficient thermoelectric conversion has focused on synthesizing materials with novel microstructures and compositions. Metastable structures present a unique opportunity in this regard. The Mg-Sn material system has a relatively unknown metastable phase which remains largely unstudied.

My work represents one of the first studies of the metastable Mg-Sn phase in a polycrystalline bulk form. I present a new synthesis route using a combination of high

energy ball milling (powder synthesis) and current activated pressure assisted densification (CAPAD) (powder densification). This method allowed for the synthesis of the metastable trigonal phase at 600 °C and 112 MPa, significantly lower pressures and temperatures than have been demonstrated previously. This method produces samples large enough for the first neutron diffraction study allowing for Rietveld structural refinements to a high degree of accuracy.

Through careful control of the synthesis process, I have also studied and characterized the densification and transformation kinetics for the trigonal phase. Analysis of the real time deformation data during CAPAD processing reveals that the transformation mechanisms can be isolated from the densification mechanisms. The transformation process is analyzed using the KJMA model modified for constant heating and shows an activation energy of 74 kJ/mol. Transformation under isothermal conditions follows a second order rate law with a higher activation energy (448 kJ/mol) caused by differing degrees of transformation completion.

The amount of metastable phase can be controlled by varying the CAPAD processing parameters. Incorporating the metastable phase into the microstructure changes the thermal, electrical and Seebeck coefficient behavior. The first measurements of this trigonal phase show bipolar diffusion behavior at much lower temperatures than the previously reported Mg-Sn based materials without the metastable trigonal phase.

Table of Contents

List of Figures

List of Tables

Chapter 1 Introduction and Motivation

1.1 Processing-Property-Structure Relationships

Materials science and engineering is a multidisciplinary field incorporating many individual fields, including, but not limited to, condensed matter physics, physical chemistry, metallurgy, as well as the ceramic, biological, electrical, and mechanical engineering fields. The idea of a multidisciplinary materials science field has been around as early as the 1960s. In 1974 the COSMAT (Committee on the Survey of Materials Science and Engineering) report was compiled in order to provide administrators and scientists with the overall nature and scope of materials science and engineering. Because of the ideas presented in that report, materials science and engineering has become its own unique field, incorporating the collective ideas and scientific views from traditionally separate fields.

The goal of materials science and engineering is to discover and develop novel materials and devices for the use of mankind. In order to achieve this, the central paradigm of materials science and engineering is to investigate the materials processing, structure, properties, and performance. These four areas and their interdependence are best illustrated in what is known as the materials science tetrahedron (Figure 1.1). While investigating each of these four areas is essential towards materials development, each is

sufficiently unique enough where collaboration with fellow scientists is required in order to satisfy the science.

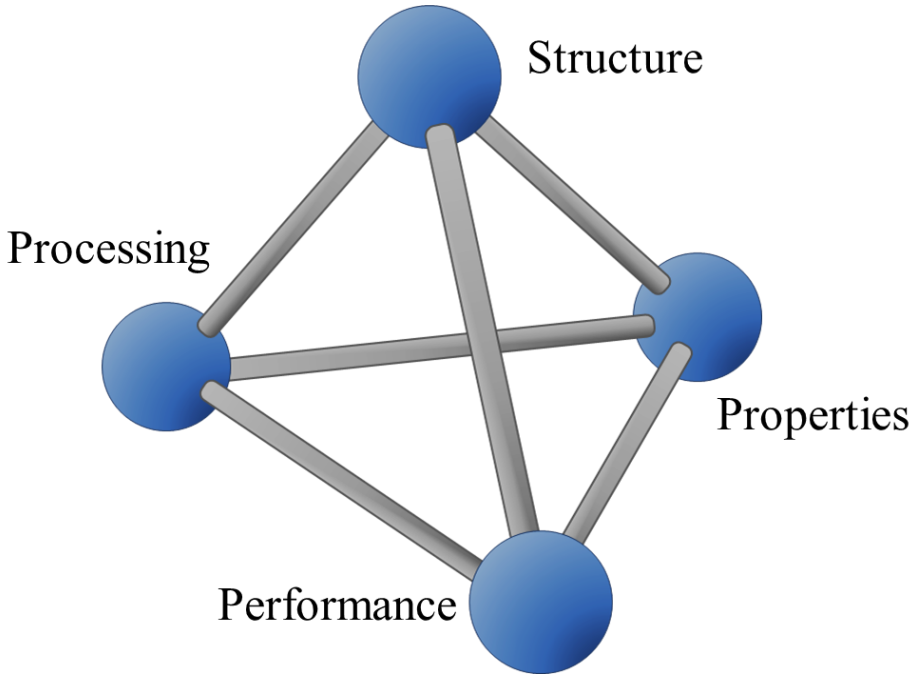

Figure 1.1 The materials science tetrahedron emphasizes the interdisciplinary research between materials processing, structure, properties, and performance.

1.2 The Magnesium-Tin (Mg-Sn) System

Magnesium based materials are attractive due to the high elemental abundance of magnesium in the earth's crust. The magnesium and tin material system is of particular interest because the two metals form a semiconducting compound, Mg_2Sn. Mg_2Sn is actively being studied for many applications including, but not limited to, structural [1], [2], hydrogen storage [3], and thermoelectric applications [4]–[8].

The Mg-Sn binary phase diagram (Figure 1.2) shows Mg_2Sn to be a line compound with little solubility of Mg or Sn in the crystal structure and a congruent melting temperature of 770.5 °C [9]–[14]. The crystal structure of Mg_2Sn was first discussed in 1904 by Sustschinsky [15]. Mg_2Sn crystallizes in the cubic anti-fluorite structure, where the Sn atoms occupy the face centered positions and the Mg atoms occupy the tetrahedral positions (Figure 1.3). The lattice parameter has been measured through x-ray diffraction analysis and is reported to be in the range of 6.75 to 6.77 Å with a theoretical density of 3.57-3.59 g/cm^3 [16]–[18]. Powdered magnesium and tin have been reported to form Mg_2Sn with an exothermic reaction at temperatures above 540 °C [19] with a reported heat of formation of 71 to 76 kJ/mol [20]–[23].

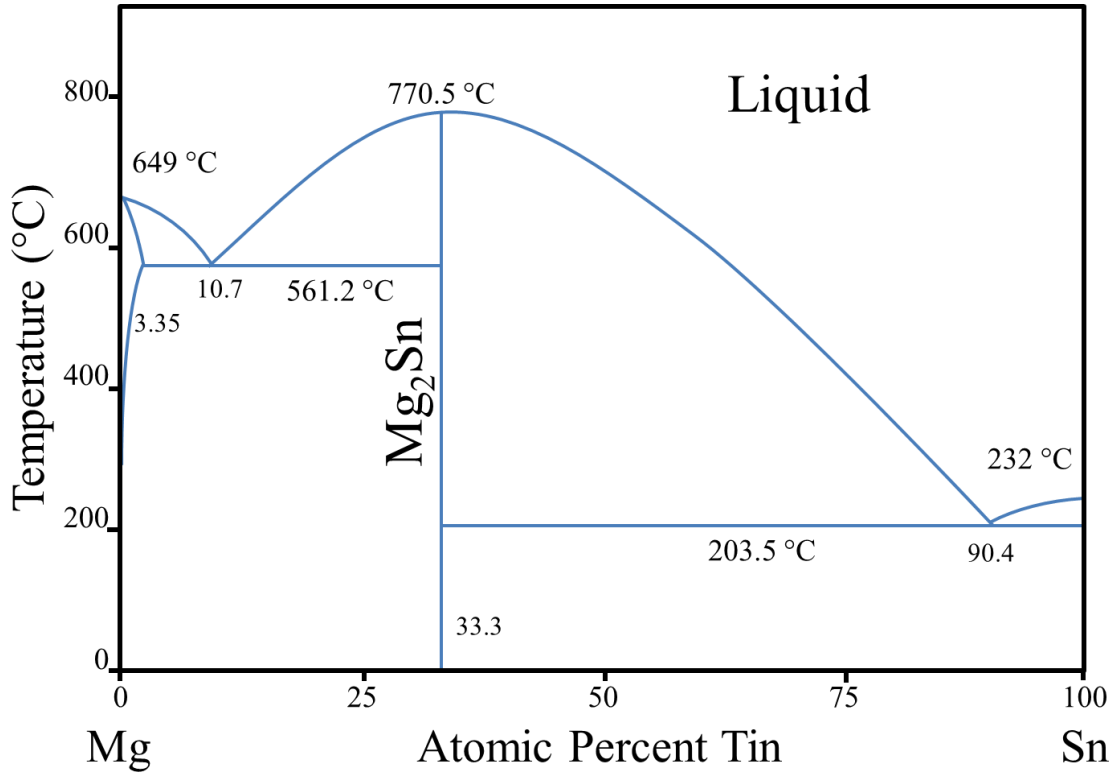

Figure 1.2 Magnesium and tin binary phase diagram (Re-drawn from [14]). Mg_2Sn is a line compound with a congruent melting temperature of 770.5 °C.

Much work has been done to characterize the transport and physical properties of Mg_2Sn. Theoretical calculations indicate that the intrinsic carrier concentration (n_i) is 2.76×10^{17} cm^{-1} [17], [24], [25]. Single crystal thermal conductivity measurements were carried out by Martin and showed a room temperature thermal conductivity of 10 W/m.K [26], [27]. The thermal conductivity temperature behavior showed a T^{-1} dependence above 150 K which is characteristic of phonon conduction in semiconductor solids [27].

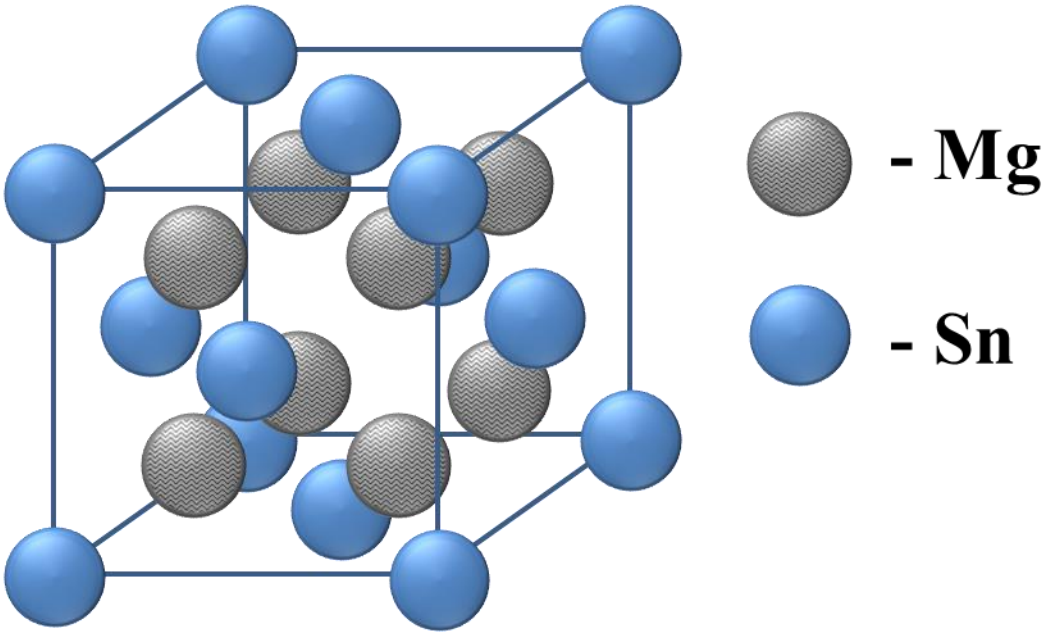

Figure 1.3 Mg_2Sn crystallizes under standard conditions in the cubic anti-fluorite structure (Fm-3m). The tin atoms (anions) occupy the face centered positions while the magnesium ions (cations) occupy the tetrahedral positions.

Mg_2Sn also has a high pressure polymorph first reported by Canon and Conlin [28]. Since it is not found on the equilibrium phase diagram at ambient pressure, it is metastable at ambient pressures. The transformation between the high pressure crystal structure and the cubic was investigated by Dyuzheva *et al.* [29]. The crystal structure of the high pressure polymorph was finally calculated by Range *et al.* [30] and assigned the trigonal R3 space group. These materials were synthesized using high pressure belt apparatus' using processing conditions exceeding 1 GPa of pressure and temperatures ranging from 600 to 1400 °C. The only reports on the transport properties of the trigonal metastable polymorph state that the material has a semiconducting electronic behavior [28], [31].

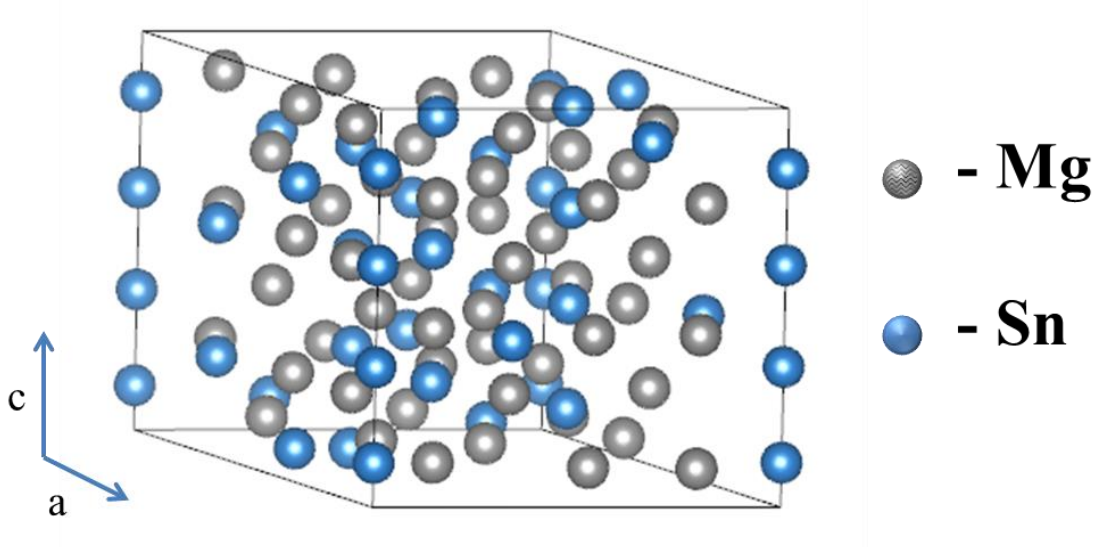

Figure 1.4 The trigonal (R3) high pressure and temperature polymorph of Mg_2Sn.

1.3 My Research Focus and Goals

The work presented in my dissertation is focused on studying the processing and transformation behavior of a metastable phase in the Mg-Sn material system and its effects on the transport properties of the material. This metastable phase has never been studied in depth due to the extreme pressure and temperature conditions for which it was first synthesized. My work is the first reported instance where the metastable trigonal Mg_2Sn has been made through powder processing and consolidation methods, yielding dense polycrystalline materials.

My dissertation is organized as follows: Chapter 1 is a general introduction to the core philosophy and views of materials science, a scientific history of the magnesium-tin

(Mg-Sn) material system including synthesis methods and properties, and a brief introduction to my motivations and goals for working on this project. Chapter 2 discusses some of the core scientific concepts, processing methods, and analysis techniques which I have applied towards this material system. Chapters 3, 4, and 5 constitute my core experimental work and results which include studying the synthesis, processing, and transformation behaviors as well as the transport properties of the material. Chapter 6 will conclude my work and I will present some ongoing work and ideas for the future of the project.

Chapter 2 Background and Theory

This chapter discusses some background information regarding the thermodynamics, processing and analysis techniques. Knowledge of classical thermodynamics is essential towards understanding material systems and phase behavior. Materials processing is the application of available tools to change the properties of a material to better suit the application. All of this is confirmed and validated through the analysis techniques.

2.1 Thermodynamics and Processing

2.1.1 Thermodynamics Background

A single solid phase can be defined as having a uniform structure and chemical composition. Phases are normally separated from other phases by boundaries, or discontinuities in the structure and/or composition. A phase undergoes a transition to another product phase when the thermodynamic conditions favor the product phase.

The Gibbs free energy of a system is used to determine the thermodynamic stability of a phase within a material system. The Gibbs free energy can be expressed as:

$$G = H - TS = E + PV - TS \tag{2.1}$$

where G is the Gibbs free energy (J), H is the enthalpy (J), T is the temperature (K), S is the entropy (J/K), E is the internal energy (J), P is pressure (Pa), and V is the volume

(m^3). A phase is considered thermodynamically stable if its free energy has a lower value than other possible phases under the same conditions. An example of this is Figure 2.1 where free energy curves for a material system with two phases are shown. The phase with the lower free energy under certain conditions is considered the stable phase. In this case, if $T<T_{transition}$, G_1 has the lower value and is therefore the more stable phase. If $T>T_{transition}$, G_2's value is lower and is considered the more stable phase.

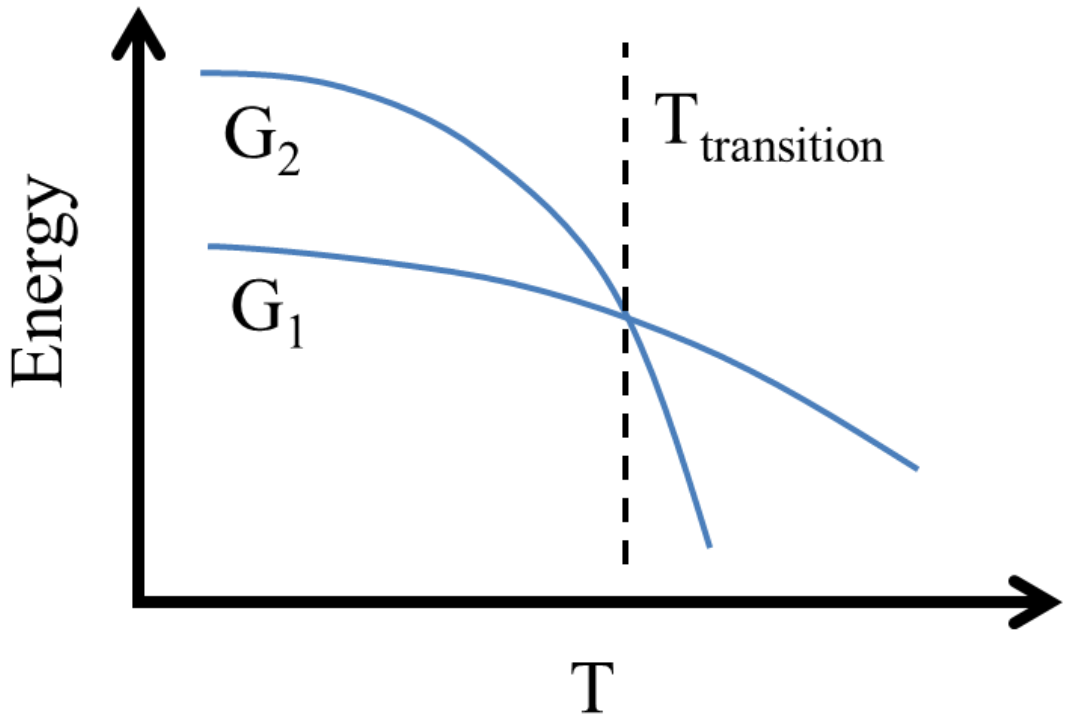

Figure 2.1 Two free energy curves (G_1 and G_2) intersecting at a transition temperature ($T_{transition}$). Phase G_1 is the more stable phase at temperatures below $T_{transition}$ while G_2 is more stable at temperatures above $T_{transition}$.

Some materials are not always found to be in their most stable phase for the conditions of temperature, pressure, and composition. They remain in a metastable phase

because of an activation energy barrier which is required for the system to convert into the more stable phase. Figure 2.2 is an example of an energy relationship of a system with two phases, phase 1 and phase 2. Phase 2 is the most stable phase; however, the rate at which phase 1 transforms into phase 2 is determined by the activation energy. Higher activation energies lead to slower transformations. Diamond (an allotrope of carbon) is a common example of a metastable phase at ambient pressures. Generally, the required temperature and pressure conditions for growing diamonds are in the range of 1300 – 1700 °C and 5.0 – 6.5 GPa [32]. The synthesized diamonds retain their structure at room temperature and pressure, the conditions where graphite is the more stable form. The transformation to graphite is slow due to its high activation energy (7.6 eV/atom [33]).

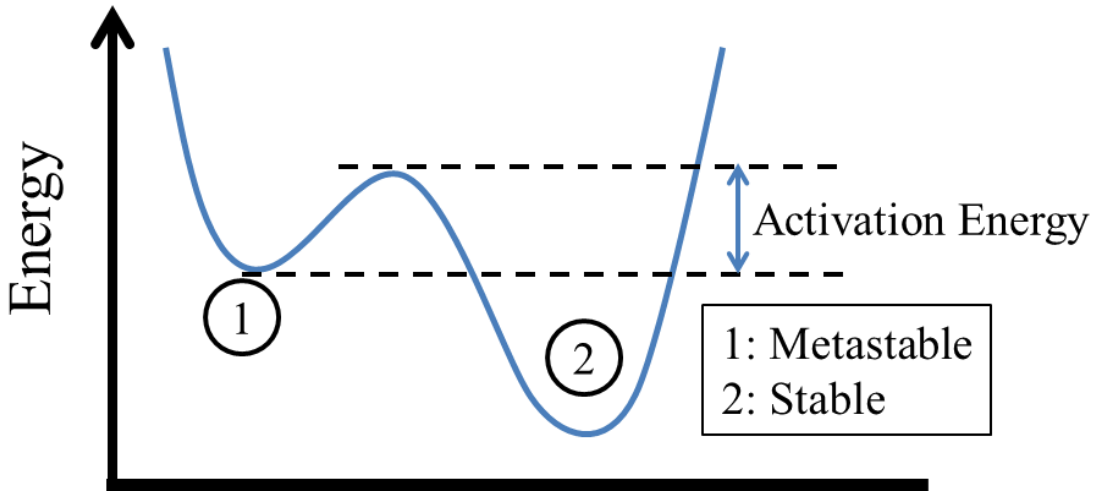

Figure 2.2 Energy diagram demonstrating a system with two local minima phases (labeled 1 and 2). Phase 1 is metastable which is less stable than phase 2.

2.1.2 Processing Kinetics

As discussed in the previous section, the rate of transformation from a metastable phase to the stable phase is determined by the activation energy. These transformation rates can be exploited through innovative processing techniques. For example, certain steel microstructures and phases are impossible to form without the processing technique known as quenching. The cooling rate of the steel allows for the optimal formation of different phases (martensite, pearlite, etc) to create a material with the desired properties.

2.2 Powder Processing Techniques

2.2.1 Ball Milling

Ball milling techniques are powder milling techniques used for mechanical alloying, powder mixing, and powder grinding. Powder and the milling media (balls) are loaded into cylindrical jars and rotated around an axis. The rotational forces allow the balls and powder to grind together resulting in breaking down powder agglomerates.

Tumble milling, or low energy ball milling, typically uses gravity as the main force for ball and powder interaction. The jars are rotated around its cylindrical axis at speeds to allow for the balls to travel up the jar wall until they fall back down and impact the powder, as shown in Figure 2.3. This type of motion involves two distinct categories of ball and powder interactions: grinding and impact.

The amount of energy from each ball impacting on the powder can be described using the following kinetic energy equation:

$$KE_1 = \frac{1}{2} mv^2 \tag{2.2}$$

where, *m* is the mass of the ball (g) and *v* is its impact velocity (m/s). The velocity of impact can be determined from the RPM, jar radius, and the mass of the balls. The kinetic energy imparted by these ball impacts are generally not high enough to influence major reactions, but are suitable for grinding down the particulate size of the powders.

The grinding energy can be related to the difference in hardness between the milling media and powder material, mass of the balls, jar rotation speed, and ball to powder weight ratio.

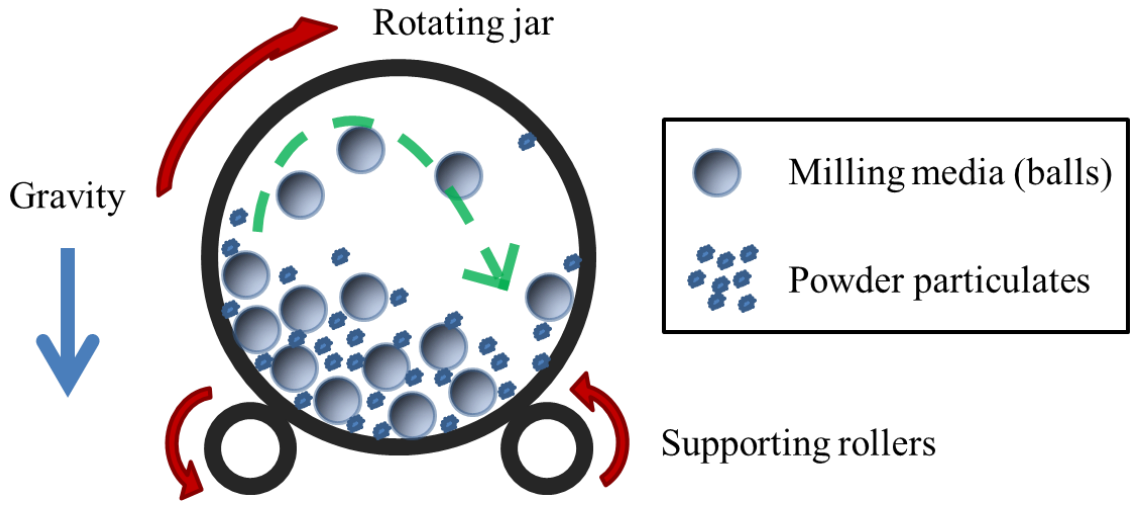

Figure 2.3 Side view schematic of a typical tumble mill apparatus. The jar rests upon two supporting rollers which drive the rotation. The green dashed arrow helps visualize the path of the ball as it travels up the wall of the jar and falls back down.

High energy ball milling is a more vigorous form of low energy ball milling. In contrast to low energy milling, where the main contributing force is gravity, high energy ball mills can run at higher RPMs and take advantage of increased centrifugal forces for higher energy ball and powder interactions. The type of high energy ball mill used in this work is a planetary ball mill. The planetary ball mill is named for the planetary style gearing where the jars rotate around their own axis (planet gears) in addition to rotating around a central offset axis (sun gear) illustrated in Figure 2.4. The centrifugal force produced from the rotating jars and the rotation around the machine's central axes allow for large amounts of kinetic energy to be transferred from the milling media (balls) and the powder. The ball and powder interactions can be separated into two categories: grinding and impact.

The amount of kinetic energy from the balls can be described using Abdellaoui and Gaffet's derivation [34]:

$$KE_2 = \frac{1}{2}m\left[(R\Omega)^2 + (r - r_b)^2\omega^2\left(1 + \frac{2\omega}{\Omega}\right)\right] \tag{2.3}$$

where, m is the mass of the ball (g), R is the radius of the system rotation disk (m), Ω is the rotational speed of the system's rotation (RPM), r is the radius of the jar (m), r_b is the radius of the balls (m), and ω is the rotational speed of the jar's rotation (RPM).

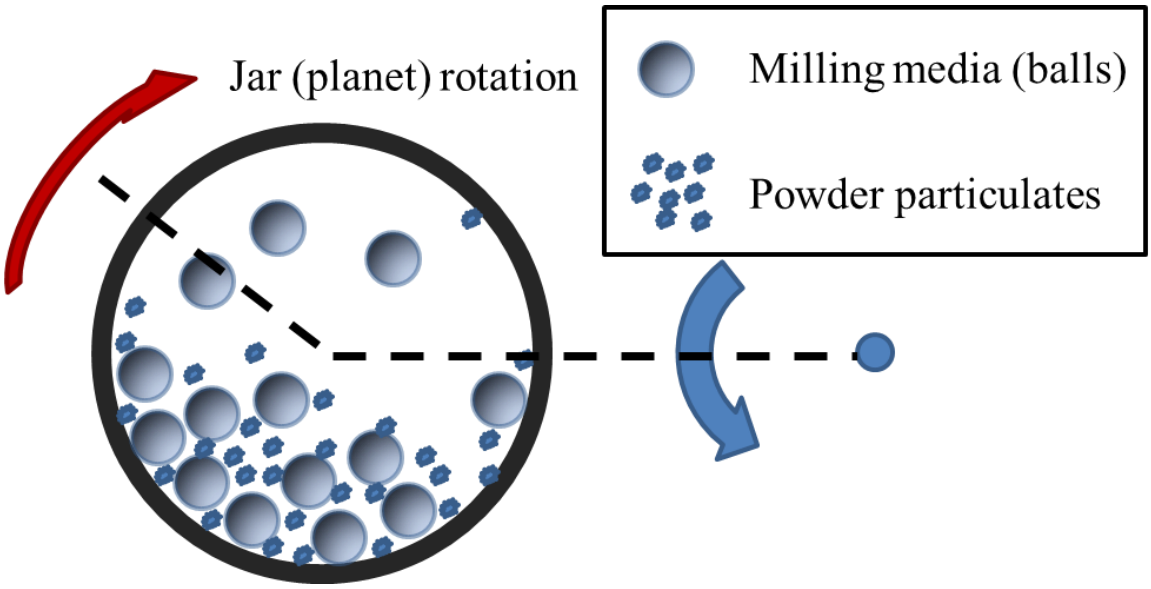

Figure 2.4 Top view (bird's eye view) of a planetary ball milling

2.2.2 Current Activated Pressure Assisted Densification (CAPAD)

Current activated pressure assisted densification (CAPAD), also known as spark plasma sintering (SPS), is a powder consolidation and molding process for polycrystalline materials. Powders are loaded into a graphite plunger and die set to form a cylindrical pellet as shown in Figure 2.5. The consolidation process, or densification process, takes place through a few broad mechanisms: sintering, particle rearrangement, and plastic deformation [35]. Typical processing considerations are: temperature, temperature rate, pressure, pressure rate, heating current, and atmosphere conditions.

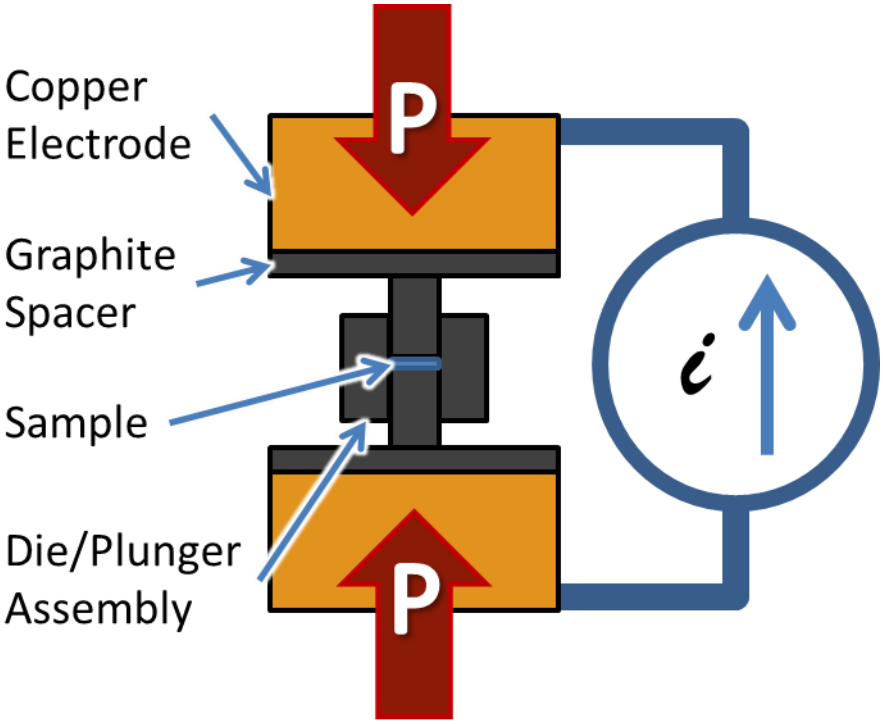

Figure 2.5 Cross section schematic of the custom CAPAD apparatus used in this study.

Processing at higher temperatures allows for a higher amount of diffusion and sintering between the particles. Temperatures required for most materials to sinter are generally above half of the melting temperature, or T_h (homologous temperature) is ~0.5, as shown in Equation (2.4):

$$T_h = \frac{T}{T_m} \cong 0.5 \tag{2.4}$$

where, T is the processing temperature (K) and T_m is the material's melting temperature (K).

Higher heating rates allow for less time spent at lower temperatures. Higher temperatures tend to promote more lattice and grain boundary diffusion mechanisms for densification [36]. Lower temperatures generally promote more surface diffusion which leads to more grain growth and less densification. This means that, while the grain growth cannot be avoided, the material can be brought to the ideal densification temperature efficiently.

The processing pressure is essential for efficient densification of powders. Consolidating powders at higher pressure have been shown to lower processing temperatures and increase the densification rate [35], [37], [38]. The processing pressure or stress can also be thought of as establishing a potential field to provide an extra driving force for diffusion [38].

Since the graphite die and plungers act as both mold and heating element, the heating current also plays a role in the densification process. Electrical currents have been shown to increase the activation energies of the formation of intermetallic materials [39]–[41]. This effect is more prevalent in material systems with electrical conductivities on the same order of magnitude or higher than the graphite.

The real time density of the material as it is being processed can be measured using the axial deformation data. The cylindrical dies allow for the density, *D*, to be calculated using the following relation:

$$D = \frac{m}{V} = \frac{m}{A(l_0 - l)} \tag{2.5}$$

where m is the mass of the sample (g), V is the volume (m^3), A is the cross sectional area (m^2), l_0 is the initial height of the sample, and l is the displacement during the experiment. Tracking the in-situ density, and the rate of change of density, allows for the ability to determine the optimum densification processing conditions.

2.3 Materials Analysis and Characterization

Materials analysis and characterization is what makes materials science possible. It forms the core concept behind materials development and discovery. This section covers some of the key methods and concepts behind the analysis techniques used in this dissertation.

2.3.1 Diffraction

Diffraction occurs when radiation (light) is scattered by a periodic array of scattering sites with spacing similar to the wavelength of the light. For the case of materials science, diffraction is used for the identification of unknown crystalline materials.

2.3.1.1 Diffraction Theory

X-ray diffraction of crystals of copper sulfate was first performed by Dr. Von Laue in 1912 [42]. His discovery of these diffraction patterns confirmed two things: that

these crystals had a periodic distribution of atoms which acted as scattering sites for x-rays and that x-rays were a form of light. However, it was not until the father and son team, William Henry Bragg and William Lawrence Bragg, conducted their own experiments in 1913 and formulated an equation to relate the wavelength of the light (x-rays) with the angle of the diffraction and atomic plane spacing (d-spacing). The resulting equation (Equation (2.6)) is known as Bragg's Law:

$$n\lambda = 2d\ sin(\Theta) \tag{2.6}$$

where, n is the order of reflection, λ is the wavelength of the x-rays (Å), d is the atomic plane spacing (Å), Θ is the diffraction angle. The

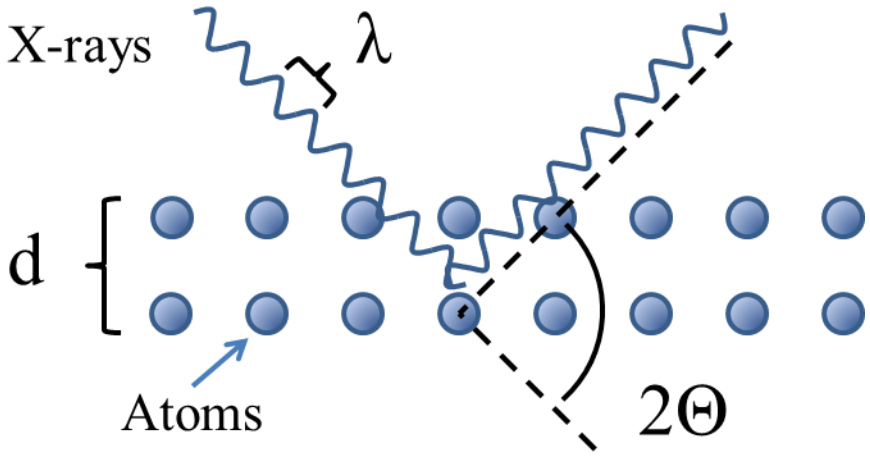

Figure 2.6 Diagram showing an atomic plane with a plane spacing (d) and incoming x-rays with wavelength (λ) diffracting off the surface at angle (2Θ).

2.3.1.2 Techniques

X-ray powder diffractometers (example, Figure 2.7) have three main components, an x-ray generation source, a specimen holder, and an x-ray detector. X-rays are normally generated using a cathode ray tube to bombard a target with high energy electrons. The electrons have enough energy to eject an inner shell target electron and produce x-rays with characteristic wavelengths specific to the target material. Copper targets produce two characteristic wavelengths: $\lambda_{K\alpha1}$=1.54056 Å and $\lambda_{K\alpha2}$=1.54440 which are used for the diffraction. These x-rays are collimated and aimed at the sample. A goniometer is used to rotate the x-ray source and detector around the sample.

Figure 2.7 PANalytical Empyrean x-ray diffractometer

Neutron diffractometers use the same concepts as their x-ray counterparts. There are two major types of neutron sources, a spallation source or a reactor source. A spallation source is typically used in junction with a linear particle accelerator where ions are accelerated to very high velocities (up to 90% the speed of light) and strike a spallation target causing neutrons to be expelled. These neutrons pass through a thermal moderator in order to be used for diffraction experiments. A reactor source creates neutrons from radioactive decay.

Neutrons, while being a subatomic particle, also exhibit wave behavior. The wavelength of a neutron can be expressed using De Broglie's equation:

$$\lambda = \frac{h}{mv} \tag{2.7}$$

where λ is the neutron wavelength (Å), h is Plank's constant (J·s), m is the mass of the neutron (kg), and v is the velocity (m/s). Some neutron sources are polychromatic (spectrum of wavelengths) instead of monochromatic. The neutrons have different wavelengths and therefore different velocities according to Equation (2.7). The wavelength of a neutron can be determined by positioning a detector at a set distance from the source and measuring the amount of time the neutron takes to travel the path. This concept is the time of flight (TOF) concept and is used for many neutron diffraction experiments. Instead moving the detectors around the sample, a stationary detector at a specific angle (Θ) can be used and record the time of the neutron detection.

2.3.1.3 Rietveld Refinement

Rietveld refinement is a method of analyzing the Bragg diffraction patterns created by materials. It was first made popular by Dr. Hugo Rietveld in the 1960s [43]–[45]. The method provides a quantitative set of equations to compare the model of a material's crystal structure's diffraction pattern with that of the observed experimental pattern. The pattern can be expressed as:

$$y_t = I_k exp[-b_k(2\Theta_i - 2\Theta_k)^2] \tag{2.8}$$

where y_t is the measured intensity, I_k is the calculated intensity (taking into account the crystal structure factor, multiplicity of the reflection, the Lorentz factor, and the full width at half max), b_k takes into account the full width at half max (deg.), Θ_i is the position of diffraction signal (deg.), and Θ_k is the calculated position of the Bragg peak (deg.). Other corrections such as the angle dependent broadening of the diffraction peaks are considered as well as preferred orientations (over-representation of certain planes due to the microstructure).

The calculated pattern is compared to the observed pattern using a least squares method to minimize any difference between the two (Equation (2.9)).

$$M = \sum_i W_i \left\{ y_i(obs) - \frac{1}{c} y_i(calc) \right\}^2 \tag{2.9}$$

where M is the function to be minimized, W_i is a weighting factor, c is a scale factor, $y_i(obs)$ is the observed pattern, and $y_i(calc)$ is the calculated pattern.

There are many free programs available for carrying out the least squares refinement including the General Structure Analysis System (GSAS) [46], Material Analysis Using Diffraction (MAUD) [47], and FullProf [48].

2.3.2 Transport Properties

Two forms of transport properties will be discussed, the transportation of electric charge and the transportation of heat. A material's electrical conductivity takes into account the amount of charge carriers (ions, electrons, and holes) which can move freely in a material. A material's thermal conductivity is primarily driven by the amount of quantized lattice vibrations (phonons) and heat carrying charge carriers.

2.3.2.1 Electrical Conductivity

A material's ability to transport charge is described by its electrical conductivity. Charge can be transported through a material by any charge carrying species such as ions and electrons. A material's resistance is related to its electrical conductivity and physical dimensions as described in Equation (2.14).

$$\sigma = \frac{1}{\rho} = \frac{l}{RA} \tag{2.10}$$

where σ is the electrical conductivity (S/m), ρ is the resistivity (Ωm), l is the length (m), R is the resistance (Ω), and A is the cross sectional area (m^2).

Generally, charge is transported in a semiconducting material by two carriers: electrons and holes. The electrical conductivity of a material takes into account both types of carriers and is given by:

$$\sigma = n_n q_n \mu_n + n_p q_p \mu_p \tag{2.11}$$

where n_n and n_p are the carrier concentrations (m^{-3}), q_n and q_p are the electric charges (C), and μ_n and μ_p are the mobilities of the electrons and holes (m^2/Vs), respectively. A higher carrier concentration allows for more charge to be transported through the material. Electrons and holes exhibit wave-like behavior while moving through a crystal structure and any perturbations or defects in the structure decrease the overall mobility of the charge carrier. Typically the mobility through a material decreases with increasing temperature due to increased lattice vibrations.

Traditionally, the electrical conductivity of intrinsic semiconductor materials has an exponential relationship with temperature due to the electrons in the valence band being thermally promoted to the conduction band with increasing temperature. Thus, there is a greater number of charge carriers at higher temperatures. The density of electron carriers with temperature can be expressed as:

$$n \propto e^{-E_g/2k_BT} \tag{2.12}$$

where E_g is the band gap (eV), k_B is Boltzmann's constant (eV/K), and T is the absolute temperature (K).

2.3.2.2 Thermal Conductivity

Thermal transport in an isotropic solid is given by Fourier's law:

$$q = -\kappa \nabla T \tag{2.13}$$

where q is the heat flux in a specific direction (W/m^2), ∇T is the temperature gradient (K/m), and κ is the thermal conductivity of the material (W/m.K). Electrons and phonons are the two main energy carriers which contribute towards a thermoelectric material's thermal conductivity. The phonon contribution describes the heat carried by lattice vibrations in the crystal structure and the electron contribution is the heat carried by mobile electrons. The two are summed together as shown here:

$$\kappa = \kappa_l + \kappa_e \tag{2.14}$$

where κ_l is the lattice contribution and κ_e is the electron contribution. Phonons are quantized lattice vibrations and are generally viewed as having quasiparticle behavior. Kinetic theory for phonon transport in a solid yields the following equation:

$$\kappa = \frac{1}{3} C v \Lambda \tag{2.15}$$

where C is the volumetric specific heat of the material (J/m^{3}K), v is the average speed of sound (m/s), and Λ is the mean free path (m). The mean free path of a phonon is determined by the phonon's scattering when making contact with boundaries,

imperfections, and other phonons. Thermal conductivity at low temperatures (typically <100 K) is dominated by its specific heat according to the Debye model ($C \propto T^3$) and increases with increasing temperature. Once the specific heat reaches a maximum with increasing temperature (Dulong-Petit Law, $C \propto 3 \times gas\ constant$), the scattering effects become dominant and the thermal conductivity begins to decrease with increasing temperatures.

Since electrons carry both heat and charge, the two are related by the Wiedemann-Franz law:

$$\kappa_e = L\sigma T \tag{2.16}$$

where L is the Lorentz number ($W\Omega K^{-2}$), σ is the electrical conductivity ($\Omega^{-1}m^{-1}$), and T is the temperature (K). Based on the assumption that the electrons in a solid behave like an electron gas and scatter elastically, L = 2.44 x 10^{-8} $W\Omega K^{-2}$.

However, if electrons and holes are both contributing carriers in the material, κ_e surpasses a summation of the two. This is known as ambipolar or bipolar thermal conductivity where both electrons and holes diffuse independently down a temperature gradient, without any net movement of charge, while transporting thermal energy which is realized when they annihilate each other. The result is a thermal conductivity which rises steeply with increasing temperature [48]–[50]. This phenomenon is possible in semimetals and semiconductors with multiple band structures.

The thermal conductivity of a material can be measured using a variety of techniques which include steady state comparative methods and

2.3.2.3 Seebeck Coefficient

The Seebeck coefficient incorporates both charge transport and heat transport and is the measure of voltage potential when a temperature gradient is placed across a material as illustrated in Equation (2.17).

$$S = \frac{\Delta V}{\Delta T} \tag{2.17}$$

where S is the Seebeck coefficient (V/K), ΔV is the voltage difference (V), ΔT is the temperature difference (K). The voltage and temperature difference are both measured at the same location on the material in order to get an accurate Seebeck coefficient.

Chapter 3 Synthesis and Structure

3.1 Introduction

The controllable production of metastable materials is one of the most exciting and challenging aspects of materials processing science [52]. The allure of metastable phases is that they can have radically different properties compared to their more stable counterparts and thus potentially be used for new applications.

Bulk metastable trigonal polymorph of Mg_2Sn has been synthesized through high pressure and temperature melting since 1964 [28]–[30], [53]. The synthesis conditions between each study varied wildly with pressures and temperatures ranging from 2.5 to 8 GPa and 600 to 1400 °C. Each of these studies synthesized their material using high pressure belt apparatuses. These custom machines allow for the application of extremely high pressures (>10 GPa) and temperatures (>2000 °C) [54]. However, these systems are usually optimized for a specific range of operating conditions and are not generally used for low temperature and pressure studies.

The metastable trigonal polymorph of Mg_2Sn has also been synthesized in powder form through high energy ball milling methods [8], [55]–[59]. High energy ball milling methods have been extensively used in powder synthesis to produce nano-structured, amorphous, and metastable phase powders [60]. While these powder studies are useful to show that the metastable trigonal Mg_2Sn polymorph can be synthesized without high pressure equipment, the bulk properties cannot be measured in powder form.

A detailed diffraction and structural computational study done by Range *et al* [30] calculated the crystal structure from a single crystal specimen synthesized at 5 GPa and 1400 °C. They concluded that the high pressure phase of Mg_2Sn crystallized in the trigonal structure with the space group R3. The trigonal structure showed a composition of Mg_9Sn_5 which contains an excess of Sn when compared with stoichiometric Mg_2Sn. Whether the trigonal structure can accommodate the Mg_2Sn stoichiometry as opposed to the Mg_9Sn_5 stoichiometry, one thing is clear, the crystal structures between the stable cubic and metastable trigonal polymorphs are extremely different.

This chapter shows the detailed studies carried out in order to synthesize the trigonal Mg_2Sn polymorph without high pressure equipment using a powder synthesis and consolidation route.

3.2 Experimental Details

3.2.1 Powder Synthesis and Consolidation

Elemental magnesium and tin powders (Alfa Aesar, 99+% metal purity) with stoichiometric ratio of 19:10 and 9:5 were planetary ball milled (PBM) using a Fritsch Pulverisette 7 (Figure 3.1) at 450 RPM using stainless steel jars and balls for a total of 48 hours at room temperature. Due to its ductility, 200-300 mg of magnesium powder was added incrementally every 2 hours until reaching the targeted stoichiometric proportions to avoid agglomeration of the magnesium on the walls of the jars [61]. The final ball to

powder weight ratio was 10:1. All powders and milling media were handled under an argon atmosphere. These powders will be referred to as Powders 1 and 2 (see Table 3.1).

Table 3.1 Preparation methods and stoichiometry of the Mg-Sn powders.

Powder designation	Preparation Method	Initial Mg:Sn stoichiometry
Powder 1	PBM	19:10
Powder 2	PBM	9:5

Figure 3.1 Fritsch Pulverisette 7 planetary ball mill unit with jars. (http://www.fritsch-international.com/sample-preparation/milling/planetary-mills/details/product/pulverisette-7-premium-line/)

The current activated pressure assisted densification (CAPAD, aka spark plasma sintering (SPS)) method was used to consolidate the powders. Graphite die and punch sets were loaded with the powders while a heating current was applied to the system under a mechanical load. A custom built CAPAD device was used to consolidate the powders into bulk materials [35]. Graphite plunger and die sets similar to the high pressure setup described by Anselmi-Tamburini et al. [62] were used to produce 9.52 mm diameter disks. All samples were processed under vacuum ($< 10^{-2}$ Torr) with an applied mechanical pressure ranging from 0 to 112 MPa and temperatures up to 600 °C with a heating rate of 200 °C/min. One plunger was removed in the 0 MPa case in order to ensure that no load (and therefore no pressure) was transferred to the powder. The maximum heating currents were varied between 400 and 1200 A. All samples were processed within 20 minutes.

XRD phase characterization was performed with a PANalytical Empyrean diffractometer using a Cu K-alpha x-ray source (($\lambda_{K\alpha1}$ = 1.54056 Å and $\lambda_{K\alpha2}$ =1.54440 Å). Densities of the CAPAD processed samples were measured using the Archimedes method. Samples densified from Powder 2 (see Table 3.1) were analyzed using neutron diffraction.

3.2.2 Neutron Diffraction

Time-of-flight neutron diffraction experiments were performed at the NPDF (Neutron Powder Diffractometer, Figure 3.2) beamline of the Manuel Lujan, Jr. Neutron Scattering Center, Los Alamos National Laboratory [63]. The CAPAD synthesized/densified bulk sample (from Powder 2, processed as described in Section 3.2.1) was crushed into a fine powder in an argon-filled glove-box. The resulting powder was then sealed in a low background vanadium can measuring 0.63 cm in diameter. The sample was then mounted on the neutron diffractometer for room temperature data collection. High-resolution data was collected for about 14.5 hours simultaneously using four groups of detector banks with nominal diffraction angles of ±46°, ±90°, ±119°, and ±148°. The mass of powder used was 2.5g.

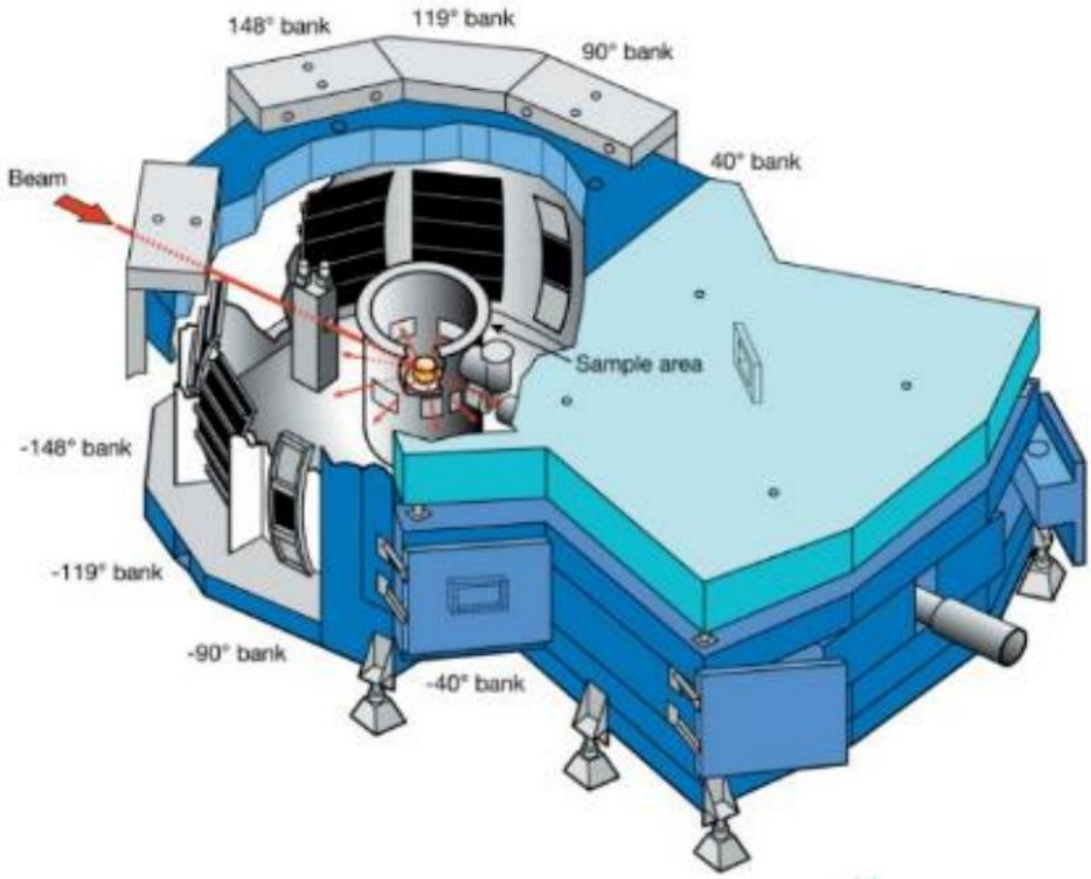

Figure 3.2 The Neutron Powder Diffractometer (NPDF) instrument at the Manuel Lujan, Jr. Neutron Scattering Center, Los Alamos National Laboratory. (http://lansce.lanl.gov/lujan /instruments/NPDF.shtml)

The obtained neutron data was analyzed using the Rietveld method with the General Structure Analysis System (GSAS) program of Larson and Von Dreele [46]. The starting structural parameters were taken from the single-crystal X-ray diffraction study of Range et al. (Space group: R3 (No.146), a = 13.222 Å, c = 13.150 Å) [30]. Since the sample contains a small portion of MgO, we included periclase as a secondary phase in the analysis (Space group: Fm-3m (No.225), a = 4.217 Å). All four datasets from the

detectors at 2Θ = ±46°, ±90°, ±119° and ±148° were simultaneously analyzed. The refinements proceeded as follows: after the scale factor and four background terms (Shifted Chebyshev function) for each histogram had converged, lattice parameters and phase fractions were added and optimized. Eight or fourteen additional background terms were then added for each histogram, and the peak profiles were fitted to a TOF profile function [64].

3.2.3 SEM/EDS Microscopy

Scanning Electron Microscopy (SEM) and Energy Dispersive Spectroscopy images and measurements were made using a JEOL JSM 6360LV microscope at an accelerating voltage of 15-20 kV coupled to an Oxford Instruments EDS detector for elemental mapping experiments. A CAPAD processed Mg_9Sn_5 sample was mechanically cleaved and was immediately introduced into the vacuum chamber. The sample was mounted upon copper tape with no further sputter treatment necessary.

3.3 Results and Discussions

3.3.1 Synthesis and Densification

Figure 3.3 presents the XRD phase analysis of the two starting elemental powders (Mg and Sn) and the planetary ball milled powders with 19:10 and 9:5 Mg:Sn stoichiometric ratios. The two ball milled powders both show the presence of two phases,

Mg2Sn and Mg9Sn5, after 48 hours of milling. No crystalline Mg and Sn peaks can be detected. The integral peak intensities of the highest intensity cubic Mg_2Sn peaks (111) are one third of the highest trigonal Mg_9Sn_5 peaks (300) in each of the two powders. The metastable phase is formed after the planetary ball milling due to the repeated impact, fracturing, and cold welding of the powder. These powders were dull blue/grey color in appearance. Similar results were reported by Urretavizcaya *et al*. [57] where they produced trigonal Mg_9Sn_5 after 150 hours using a magnetic field assisted high energy ball milling approach.

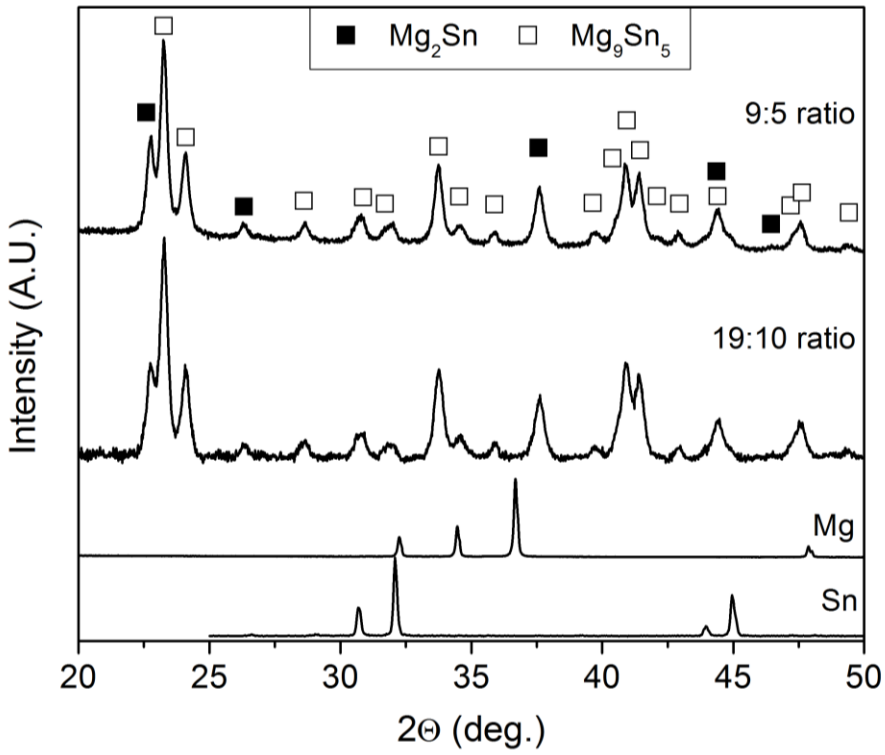

Figure 3.3 XRD powder patterns of the starting elemental powders and planetary ball milled powders with Mg:Sn stoichiometric ratios of 9:5 and 19:10 (Powders 2 and 1, respectively). Dark squares represent the cubic Mg_2Sn phase. Open squares represent the trigonal Mg_9Sn_5 phase.

Figure 3.4 is the XRD analysis of two samples processed using CAPAD from the 9:5 ratio batch of powder (Powder 2). The samples were processed using 0 and 112 MPa of applied pressure at 600 °C. The sample processed at 112 MPa shows only the presence of the Mg9Sn5 phase while the sample processed at 0 MPa still shows both Mg_2Sn and Mg_9Sn_5, indicating an effect of pressure on the formation of the metastable phase. It is not surprising that the pressure plays a significant role since as mentioned earlier, the phase is usually synthesized under high pressures. It is worth emphasizing however, that 112 MPa is significantly lower pressure than previously reported. It is also noteworthy that the peaks in the ball milled powder are considerably broader than those of the CAPAD processed samples. This is likely due to residual stress and/or fine crystal size of the PBM powder.

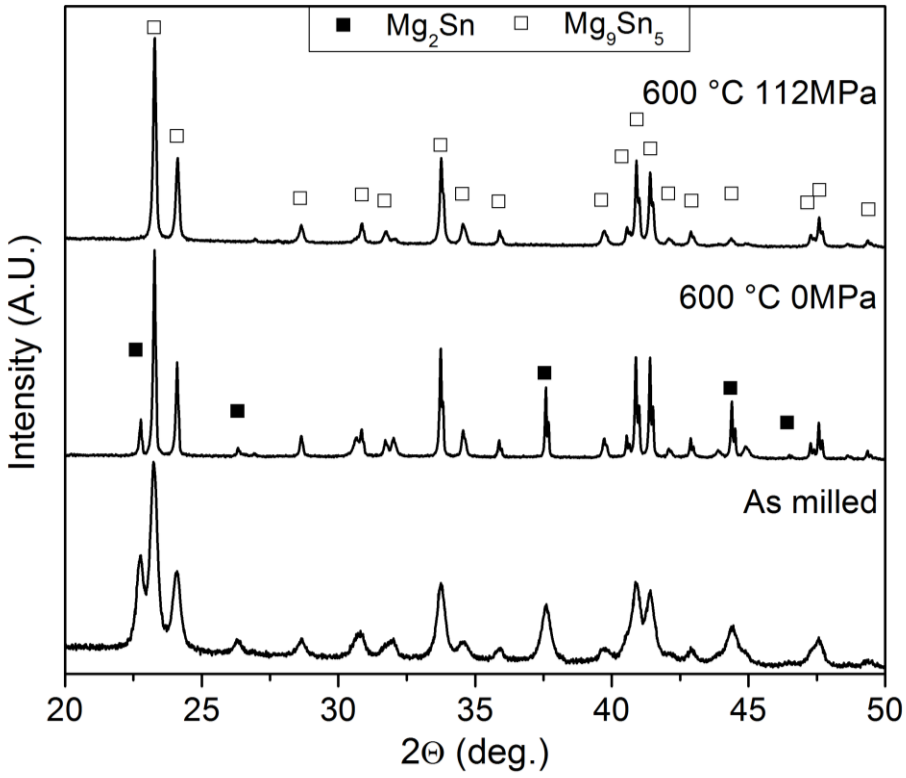

Figure 3.4 XRD patterns of the 9:5 ratio powder (Powder 2) processed at 600 °C with 112 and 0 MPa. Dark squares represent the cubic Mg_2Sn phase. Open squares represent the trigonal Mg_9Sn_5 phase.

In order to find the optimum processing conditions for producing bulk dense trigonal Mg_9Sn_5, seven samples from the 19:10 ratio powder batch were processed using CAPAD at different temperatures with 112 MPa of applied mechanical pressure. Processing temperatures ranged from 100 °C to 600 °C. The effect of these processing temperatures on the phase composition of the samples is shown in Figure 3.5. Samples processed below 400 °C show relatively little change in composition from XRD analysis. Once the processing temperature exceeds 400 °C, the peak intensities for the cubic

Mg_2Sn phase begin to disappear. By 500 °C, the Mg_2Sn peaks are no longer detectable from the XRD data. The transformation occurring at temperatures higher than 400°C is consistent with Dyuzheva et al. [29]. It should be noted that the pressure used in this previous preparation is significantly higher than the one we have used.

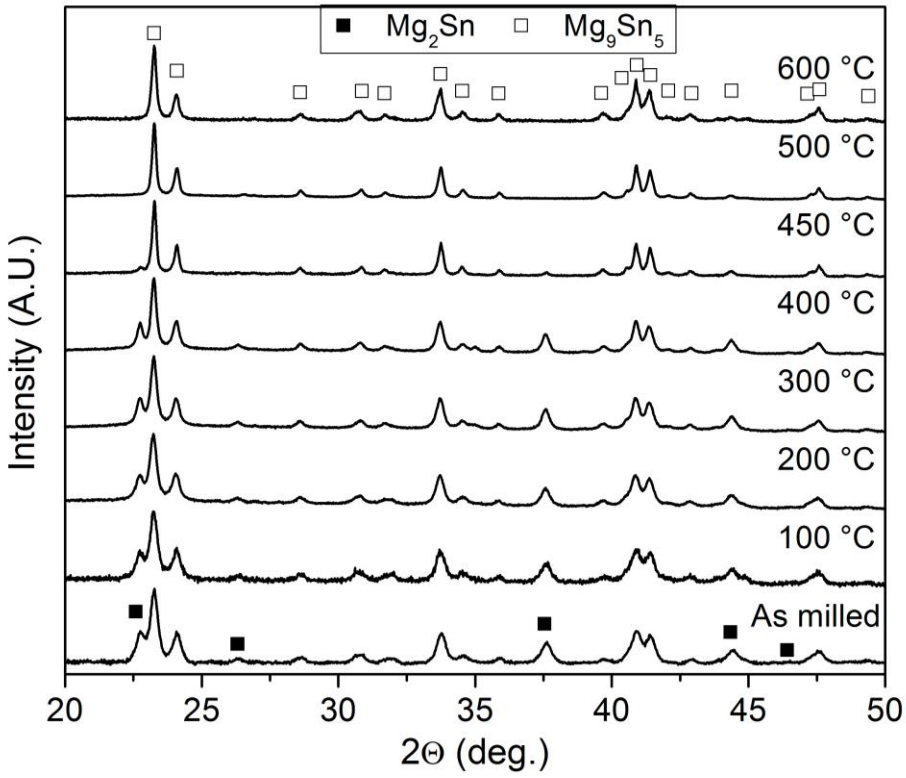

Figure 3.5 XRD powder patterns of the starting 19:10 ratio ball milled powder and CAPAD processed samples at various temperatures. Dark squares represent the cubic Mg_2Sn phase. Open squares represent the trigonal Mg_9Sn_5 phase.

The effect of CAPAD temperature on the transformation from the as-ball milled two phase (Mg_2Sn + Mg_9Sn_5) powder to a single phase Mg_9Sn_5 powder can be appreciated in Figure 3.6, where we plot the integral intensity ratios of the Mg_9Sn_5 (300)

peak to the Mg_2Sn (111) peak, which are the highest intensity peaks for the respective phases. As mentioned previously, the intensity ratio of the as-ball milled powder (25 °C data point) was 0.33. The data in Figure 3.6 reveal that the intensity ratio remains constant up to 450 °C of processing temperature. The intensity ratios of the samples produced at 500 °C and higher fall to zero indicating complete conversion to the Mg_9Sn_5 phase. For comparison, we also plot the intensity ratios of 9:5 stoichiometry PBM powder samples processed using 2 different pressures. As expected, the sample processed using 112 MPa falls directly on top of the 600 °C point from 19:10 stoichiometry. The sample processed without applied pressure demonstrates an incomplete conversion to Mg_9Sn_5.

The conversion from two phases (Mg_2Sn and Mg_9Sn_5) to a single Mg_9Sn_5 phase with an applied pressure of 112 MPa and temperatures exceeding 500 °C indicate that Mg_9Sn_5 is more stable than Mg_2Sn under our processing conditions. It is interesting to note that Mg_9Sn_5 is still metastable compared to the Mg_2Sn at ambient temperature and pressure since as mentioned before, it is not found on the traditional temperature composition phase diagram (See Figure 1.2). Previous reports of synthesis of bulk single crystals of this phase started with either elemental Mg and Sn or the Mg_2Sn phase [28]–[31], [53], [65] and required an order of magnitude higher pressure (GPa vs 100 MPa) to obtain the Mg_9Sn_5 phase. It is likely that the Mg_9Sn_5 present in our PBM starting material acts as a seed or template for further conversion of Mg_9Sn_5. Further studies are on underway to establish a mechanism for the conversion as well as to analyze the kinetics of the process.

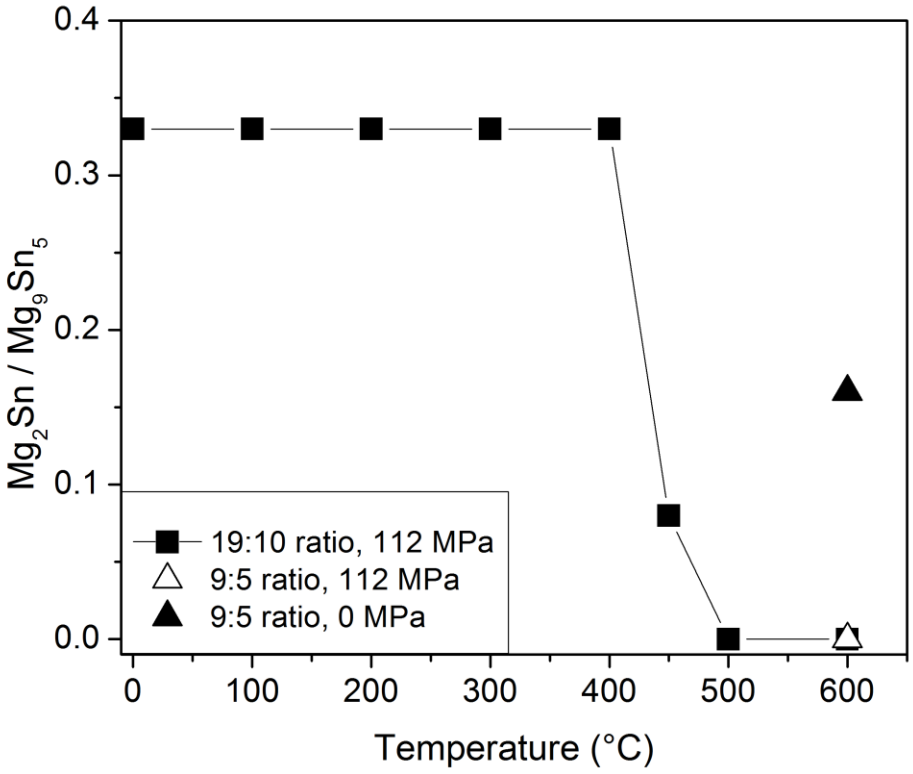

Figure 3.6 Integral intensity ratios of trigonal Mg_9Sn_5 (300) and cubic Mg_2Sn (111) vs processing temperature (Powder 1, 19:10 ratio starting powder).

The effect of hold time at 400 °C was also investigated. Samples were held at 0, 5, 10, and 20 minutes upon reaching 400 °C as shown in Figure 3.7. There is very little change in the XRD patterns of the samples held for times shorter than 20 minutes. The sample held at 20 minutes shows a decrease in the Mg_2Sn (111) peak intensity. The intensity ratios plotted in Figure 3.8 reinforces these findings.

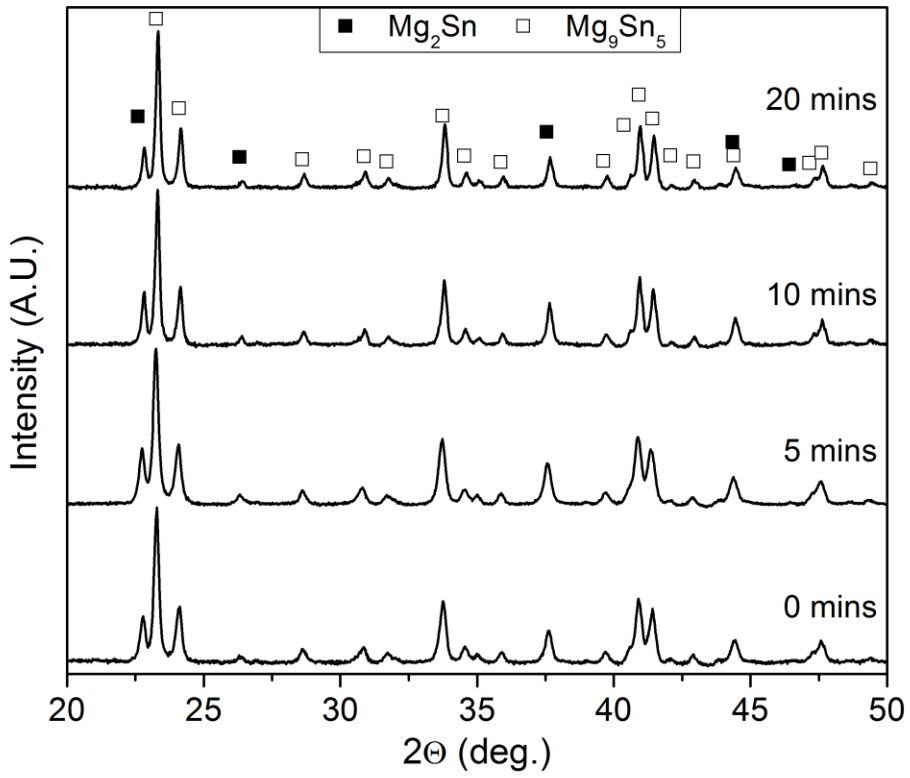

Figure 3.7 XRD patterns of 19:10 ratio ball milled powder (Powder 1) processed at 400 °C with varying hold times. Dark squares represent the cubic Mg_2Sn phase. Open squares represent the trigonal Mg_9Sn_5 phase.

One of the main goals of this work is to create bulk and dense materials using CAPAD. Since densification mechanisms are highly temperature dependent, the densities are expected to increase up to the theoretical maximum with increasing temperature. From Figure 3.9, we can see increasing sample densities with increasing processing temperature. The densities of the samples reach a plateau of ~3.8 g/cm^3 with temperatures

exceeding 400 °C. In addition to the densification mechanisms (decreasing porosity), the transformation of the crystal structure contributes to the density increase. Mg_9Sn_5 with a calculated density of 3.99 g/cm^3 is a denser phase compared to Mg_2Sn with a density of 3.6 g/cm^3. Comparison of the 9:5 stoichiometry powder processed with 0 MPa and 112 MPa emphasize the drastic effect of pressure on the densification; with 0 MPa the sample density remains comparable to the green density, 2.25 g/cm^3. In other words, the sample is still a powder, not a dense bulk solid with mechanical integrity.

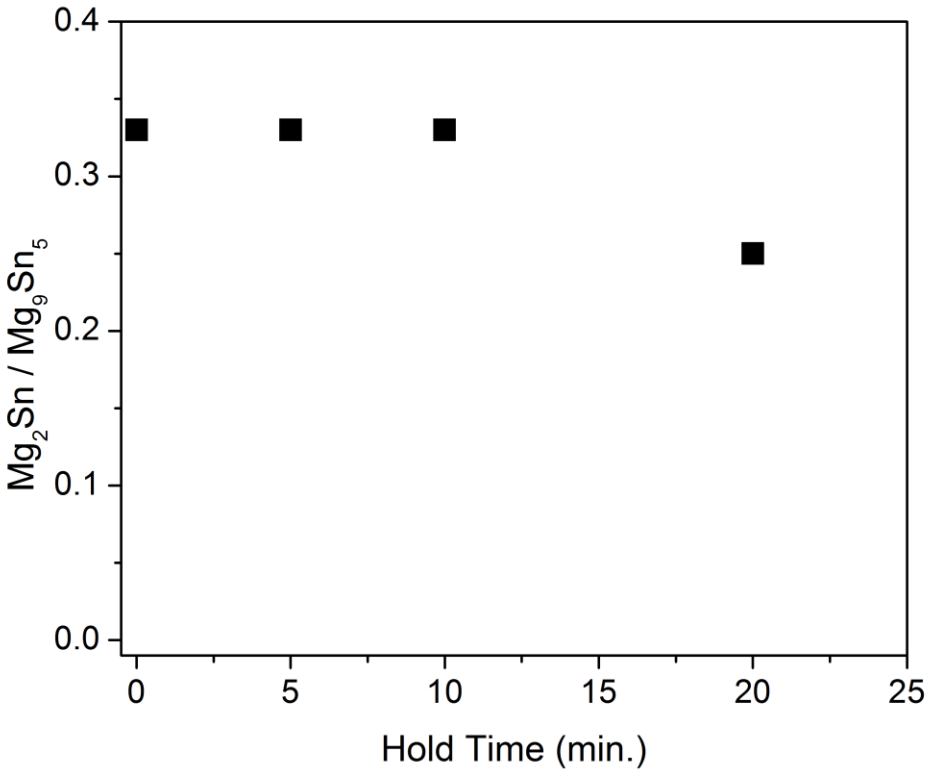

Figure 3.8 Integral intensity ratios of Mg_9Sn_5 (300) and Mg_2Sn (111) of samples processed at 400 °C with varying hold times (Powder 1, 19:10 ratio starting powder).

Typically, hold time also plays a role in final densities. Samples processed at 400 °C and 112 MPa were held for 0, 5, 10, and 20 minutes. Hold times at this temperature and time range did not have a significant effect; all samples had a density of approximately 3.8 g/cm^3 as shown in Figure 3.10.

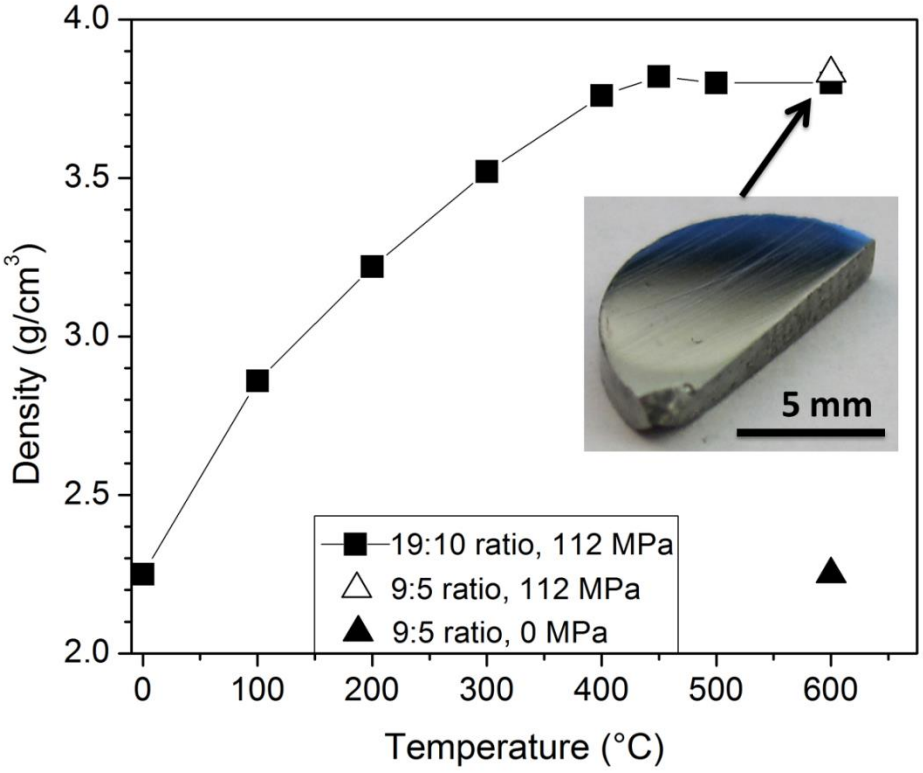

Figure 3.9 Green body density and densities of the CAPAD processed powder compacts. A photograph of a polished sample (9:5 ratio, 112 MPa, 600 °C, open triangle) is included for visual aid.

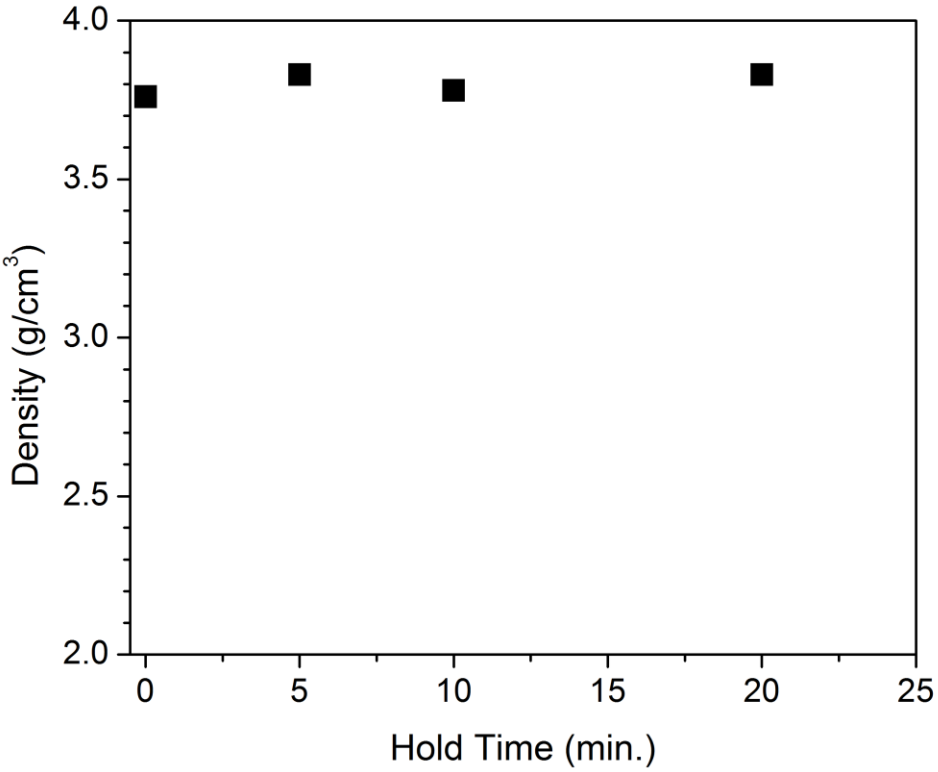

Figure 3.10 PBM ratio 19:10 (Mg:Sn) sample processed at 400 °C and held for different amounts of time.

3.3.2 Morphology and Chemical Composition Characterization

The morphology and chemical composition of the CAPAD processed Mg_9Sn_5 material was interrogated via SEM and EDS. A solid, densified sample of Mg_9Sn_5 that was CAPAD processed at 600 °C and 112 MPa was mechanically cleaved and immediately introduced into the vacuum chamber of the electron microscope. Figure 3.11

shows electron micrographs at both high (20,000 X) and low (5,500 X) magnification. In the low magnification image, the cleaving process shows both inter- and intra-granular fractures. Two domain sizes were observed, one large with smooth areas on the order of 1-2 μm. The second domain size, with smaller grains, is on the order of 100s of nanometers.

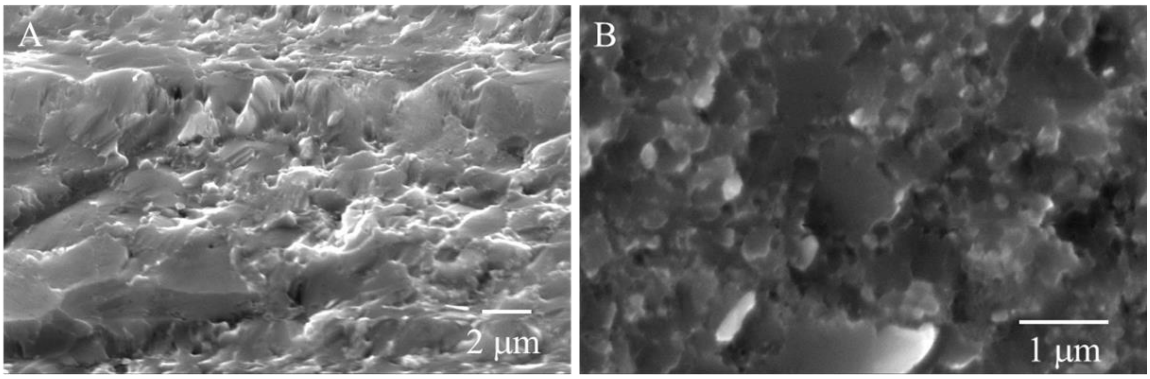

Figure 3.11 SEM images of freshly cleaved densified trigonal Mg_9Sn_5 after CAPAD treatment at 600 °C and 112 MPa at low magnification (A, 5,500X) and at high magnification (B, 20,000X).

The elemental map shows the material is composed solely of magnesium and tin and is homogeneously distributed throughout the sample, Figure 3.12. Also, the minor peaks observed between ~0.3 to 0.5 keV can be attributed to C, N, and O or to the weakly held outer shell electrons of tin (~0.4 to 0.5 keV). While every attempt was made to minimize environmental artifacts, the sample is mounted on copper tape, which has an organic-based adhesive. In addition to phase identification via powder XRD, quantification of the Mg/Sn signal ratio corresponds well to the 9:5 stoichiometry

confirming not only the stoichiometry but also a lack of any amorphous phases that would not be detected by diffraction methods.

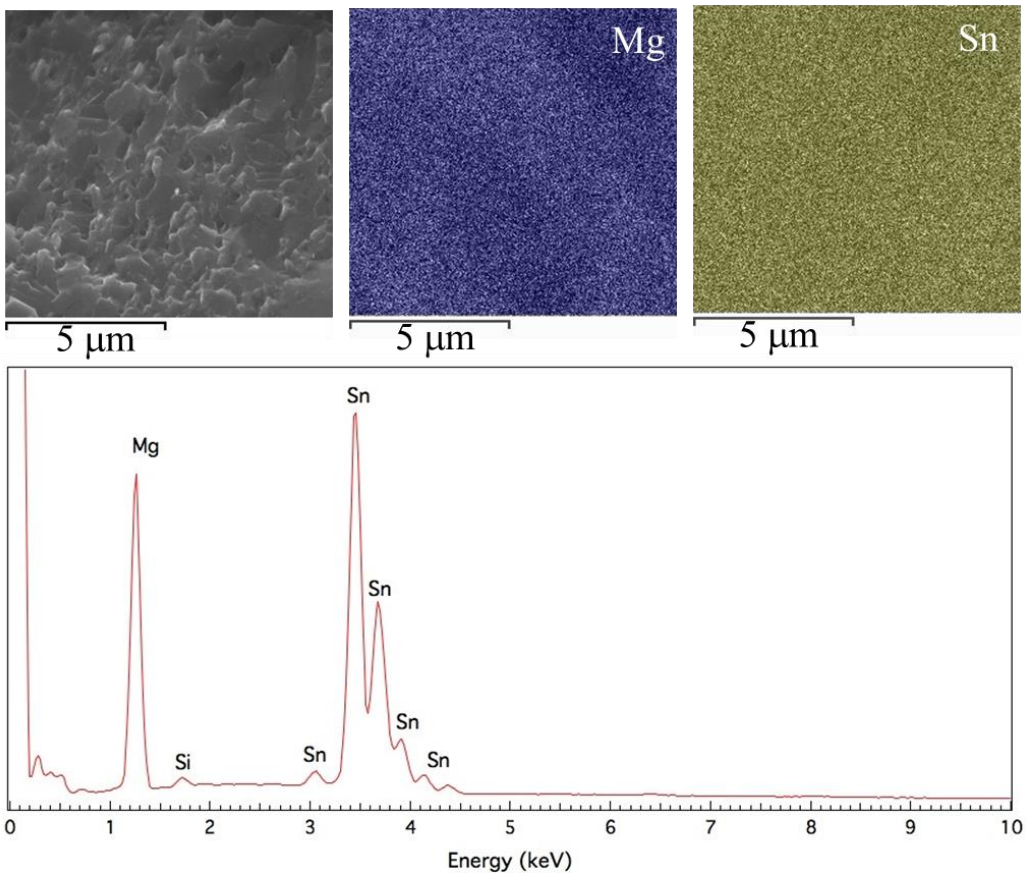

Figure 3.12 The homogeneous nature of the sample is demonstrated by SEM. (Top) SEM/EDS mapping images of freshly cleaved densified trigonal Mg_2Sn after CAPAD treatment at 600 °C and 112 MPa. (Bottom) Total EDS spectra from mapping experiment showing exclusively Mg and Sn. The Si peak at 1.8 keV is a detector artifact.

3.3.3 Crystal Structure Refinement

On convergence of the parameters given in experimental procedure (section 3.2.2), atomic coordinates and atomic displacement parameters (constrained to be

equivalent on all six Mg sites and, separately, all Sn sites) were refined yielding an R_{wp} value of 2.13%. The fitted patterns are shown in Figure 3.13. Our Rietveld analysis of the obtained neutron diffraction data indicates that the synthesized major phase adopts the same structure as the Mg_9Sn_5 phase prepared at high pressure [30]. Neutron patterns also reveal the existence of an MgO impurity in the sample, and its content is determined to be ~4.4 wt.%. Existence of oxide phases in Mg-Sn alloys is not surprising since they are known to be oxygen sensitive [14], [28], [66]. Although the procedure was done in Ar, the crushing of the bulk dense material into powder and transportation could have contributed to oxide formation in powder analyzed by neutron diffraction. The significantly higher surface area of the powder compared to bulk can lead to more rapid oxide formation.

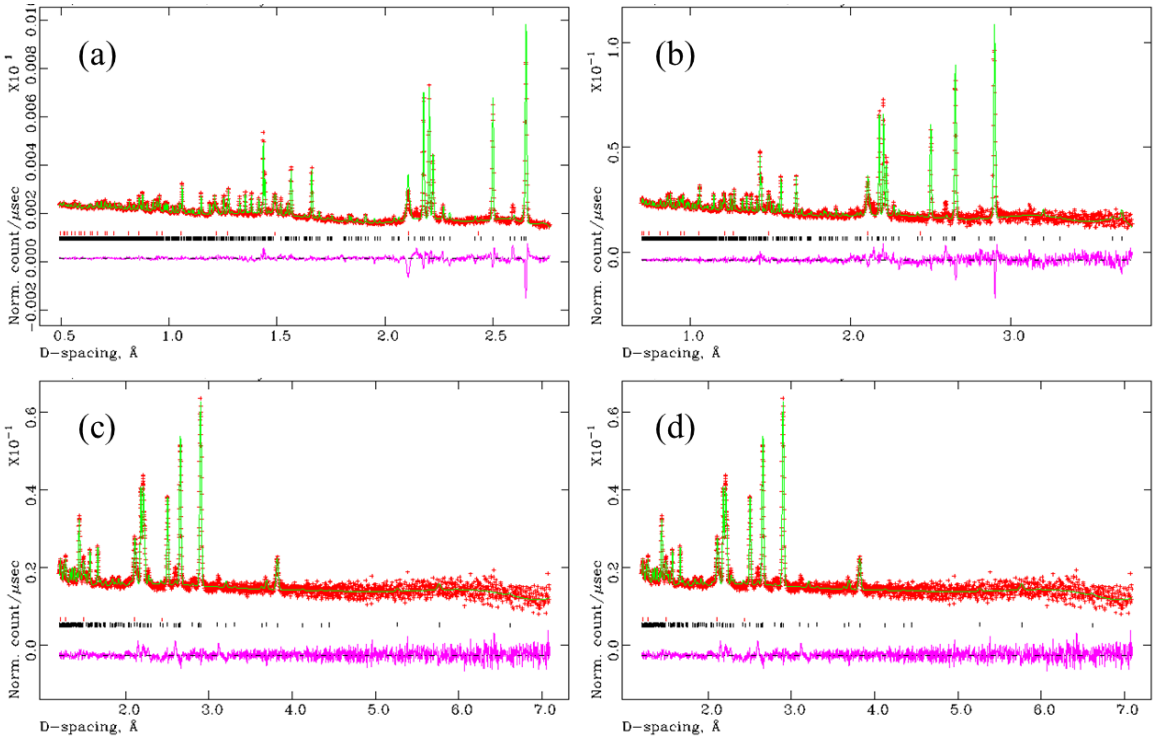

Figure 3.13 Fitted neutron diffraction patterns collected at (a) 2Θ = 148°, (b) 2Θ = 119°, (c) 2Θ = 90° and (d) 2Θ = 46°. Data are shown as red plus signs, and the solid green curve is the best fit to the data based on the structure model. Black and red tick marks below the pattern show the positions of allowed reflections for Mg_9Sn_5 and impurity phase MgO, respectively. The lower pink curve represents the difference between the observed and calculated profiles.

The refined unit-cell parameters, atomic positions and isotropic displacement parameters are listed in Table 3.2 and Table 3.3, respectively, and the refined structure is shown in Figure 3.14. Similar to the structure of the high-pressure synthesized Mg_9Sn_5 phase, the structure of this phase is comprised of a three-dimensional framework of Mg atoms with Sn situated in the structural tunnels parallel to the c-axis. In each unit cell, there are six crystallographically distinct sites for Sn (Table 3.3). Sn1 and Sn2 occupy

tunnels with a trigonal cross-section, whereas other Sn atoms (Sn3, Sn4, Sn5 and Sn6) occupy tunnels with a hexagonal cross-section (Figure 3.14(a)).

Table 3.2 Unit-cell parameters and refinement agreement indices of Mg_9Sn_5 (space group R3).

a (Å)	*c* (Å)	*c/a*	*V* (Å^3)	R_{wp} (%)	R_p (%)	χ^2
13.2359(2)	13.3432(3)	1.008	2024.41(9)	2.13	1.31	4.28

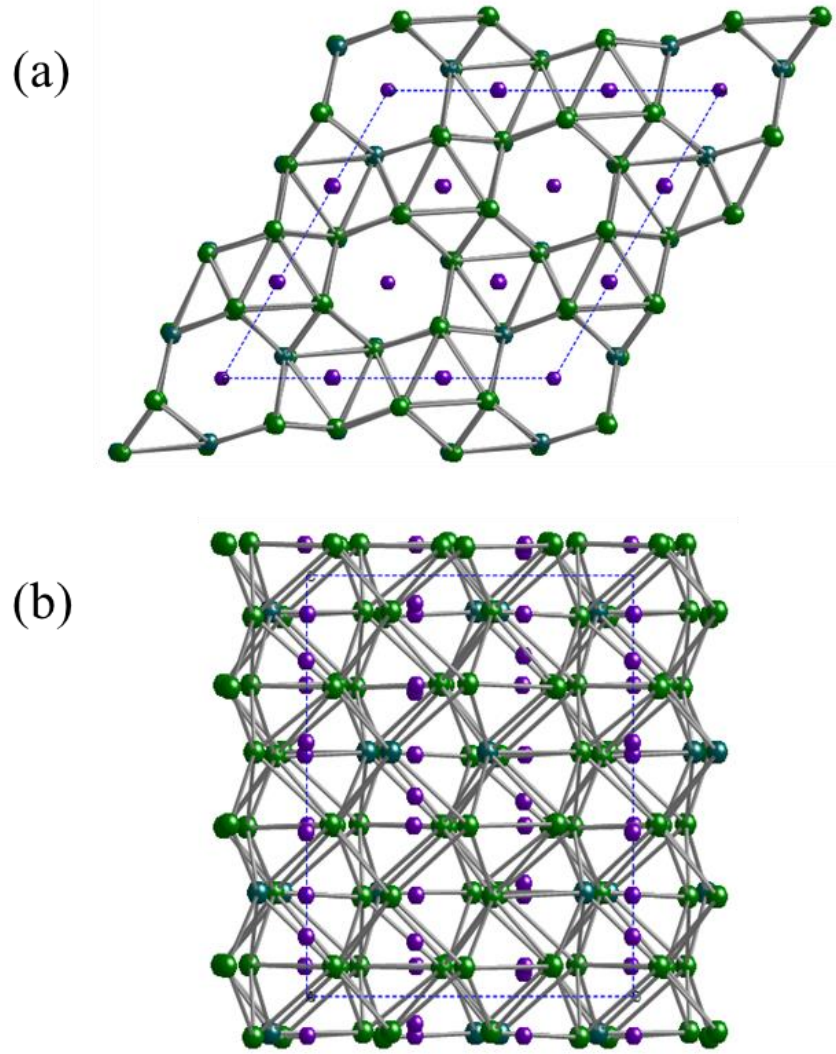

Figure 3.14 Crystal structure of Mg_9Sn_5 projected along (a) the c-axis and (b) the a-axis. Green balls represent Mg atoms, purple balls represent Sn atoms, and dashed blue lines outline a unit cell.

Table 3.3 Atomic coordinates and atomic thermal parameters of Mg_9Sn_5.

Atom	*x*	*y*	*z*	U_{iso} (Å^2/100)
Mg1	0.245(1)	0.164(1)	0.0713(8)	1.03(4)
Mg2	-0.237(1)	-0.162(1)	-0.0976(10)	1.03(4)
Mg3	0.516(1)	0.414(1)	0.0671(9)	1.03(4)
Mg4	0.482(1)	-0.408(1)	-0.0872(9)	1.03(4)
Mg5	0.494(1)	0.593(1)	0.2474(8)	1.03(4)
Mg6	-0.495(1)	0.407(1)	-0.2576(8)	1.03(4)
Sn1	0.335(1)	0.336(1)	0.2396(6)	0.69(3)
Sn2	-0.336(1)	-0.338(1)	-0.2605(6)	0.69(3)
Sn3	0	0	0.3902(8)	0.69(3)
Sn4	0	0	-0.3991(8)	0.69(3)
Sn5	0	0	0.1425(8)	0.69(3)
Sn6	0	0	-0.2033(8)	0.69(3)

Range *et al*. [30] pointed out that their high-pressure synthesized Mg_9Sn_5 phase is similar to the so-called "dense form Mg_2Sn" that had been reported earlier by Cannon and Conlin [28] and Dyuzheva *et al*. [29]. However, there are differences in c/a ratio between these phases. While the c/a ratios of "dense form Mg_2Sn" are 1.027 and 1.007 (from Cannon and Conlin [28] and Dyuzheva *et al*., [29] respectively), that of the high-pressure synthesized Mg_9Sn_5 phase is 0.9946 (Range *et al*. [30]). Note that the c/a ratio of our Mg_9Sn_5 phase is 1.008, similar to one of the values for "dense form Mg_2Sn". These differences are probably due to subtle differences in Mg/Sn ratio among these samples.

3.4 Conclusions and Summary

We were able to synthesize bulk polycrystalline Mg_9Sn_5, a metastable polymorph of Mg_2Sn, using a combination of mechanical alloying and CAPAD processing. This phase was synthesized at significantly lower pressures (112 MPa compared to 2-6 GPa) and temperatures (< 500 °C compared to 600-1200 °C) than previously reported. This is the first instance (that we know) of this phase produced in a dense polycrystalline form. It is also the first time that the Mg_9Sn_5 phase has been confirmed and detailed via neutron diffraction refinement.

Large polycrystalline samples like those presented here are excellent for property measurements and are easy to integrate into devices and applications. We expect the processing procedures developed here to be translatable to other alloy systems, opening the door for the production of other metastable alloys that are difficult to synthesize by other methods.

Chapter 4 Transformation Kinetics

4.1 Introduction

The Mg-Sn system is a promising material system that is currently being studied as a low cost and high performing material for renewable energy applications [4]–[8], [58]. The intermetallic Mg-Sn system has two compounds: Mg2Sn (cubic anti-fluorite, Fm3m), a line compound [14] that appears in the binary phase diagram, and a metastable phase (trigonal, R3) which is not found in the phase diagram. The trigonal phase in the Mg-Sn system has been reported and synthesized by different methods, but many aspects surrounding this phase, e.g., its relation to the stable cubic phase, remain unclear. This phase has been assigned the stoichiometry of Mg_9Sn_5 and identified as having a trigonal symmetry with the space group R3 [30]. It was originally synthesized through high pressure and temperature melting with conditions exceeding 1 GPa and 1000 °C [28]–[31], [53], [65]. More recently, it has been found that solid state mechanical alloying from Mg and Sn elemental powders also produces the metastable polymorph in powder form [55]–[57]. It was shown in Chapter 3 that the metastable polymorph can also be synthesized in bulk form using a combination of high energy ball milling and the powder consolidation method: Current Activated Pressure Assisted Densification (CAPAD), [67]. We showed that, under these conditions, the cubic phase transforms to the trigonal phase upon CAPAD processing, i.e. the trigonal phase “grows” out of the cubic. Alloying and composite formation is a common strategy for producing high performance bulk

materials with thermoelectric applications [68]. The processing procedure outlined in Chapter 3 allows for the co-existence of cubic and trigonal Mg_2Sn phases which can provide a unique opportunity to make composite materials with distinctive properties.

This chapter presents a study of the cubic/trigonal phases in the Mg-Sn system with the aim of understanding the processing (both transformation and densification) kinetics, enabling control the phase fractions of the composite system. The densification event can be monitored with real time deformation data, while the rate of transformation can be evaluated using rate constant, *k*, which is related to the activation energy, *E*, by the well-known Arrhenius relationship:

$$k = Ae^{\frac{-E_T}{k_B T}} \tag{4.1}$$

where A is the pre-exponential factor, k_B is the Boltzmann constant and T is the temperature. The analysis is facilitated by considering the entire densification process as three different stages: a densification dominated stage and two different transformation dominated stages as follows: 1) Densification dominated stage in which the ball milled powder is densifying via reduction of porosity and phase transformation 2) Phase transformation that occurs while heating at constant heating rate 3) Phase transformation that occurs at the final hold temperature with varying hold times i.e. isothermal transformation.

4.2 Experimental Details

Elemental magnesium and tin powders (99.9+% purity, Alfa-Aesar, -325 mesh) were combined in a 9:5 (Mg:Sn) stoichiometric ratio. Stainless steel jars and milling media (4.7mm diameter balls, 10:1 ball to powder ratio) were used in a Fritsch Premium 7 planetary ball mill (PBM) for 48 hours at 450 RPM. The agglomeration of magnesium was mitigated by adding 200-300 mg of magnesium and tin powder incrementally every 2 hours until reaching the desired 9:5 Mg:Sn stoichiometric ratio. The powder was then sieved through a 325 mesh screen.

The planetary ball milled powders were consolidated using the Current Activated Pressure Assisted Densification (CAPAD) method [35] in graphite die and plunger sets (9.51 mm pellet diameter) similar to the high pressure setup described by Anselmi-Tamburini *et al.* [62]. The load in the system is applied using a universal test frame (Model #5584 Instron Inc., USA) with a displacement resolution of 0.0747 μm and a load measurement accuracy of 0.4%. The pressure was applied initially and then the material was heated at a rate of 200 K/min. The temperature was controlled using a type N thermocouple inserted into the outer die wall. All materials were processed in a vacuum of $< 10^{-2}$ Torr, under a uniaxial pressure of 112 MPa with temperatures ranging from 698 K to 873 K.

Two sets of CAPAD experiments were performed. In the first set, the samples were heated to a desired maximum temperature and cooled immediately upon reaching the temperature; we will refer to these as constant heating rate experiments. In the second

set, the samples were heated to a desired maximum temperature and held for varying times (between 300 and 10800 s) before cooling; these are referred to as isothermal experiments. A heating rate of 200 K/min was used to achieve the desired processing temperatures in both sets. The materials were cooled at a rate of ~150 K/min to preserve the phase composition. The densities of the samples were measured after densification using the Archimedes method. The real time deflection data was used to calculate densities and densification rates using a procedure presented by the Garay group [38].

The ball milled powders and densified samples were analyzed using powder X-ray diffraction (XRD) using a PANalytical Empyrean system with a Cu Kα X-ray source ($\lambda_{K\alpha1}$ = 1.5406 Å and $\lambda_{K\alpha2}$ = 1.5444 Å). The cubic and trigonal phase fractions were determined from Rietveld analysis of XRD data using the General Structure Analysis System (GSAS) program with the EXPGUI interface [46], [69]. The starting structural parameters for the cubic phase were taken from Pauling's study [70] and those for the trigonal phase from the previous structural characterization using neutron diffraction (Chapter 3) [67].

4.3 Results and Discussions

XRD analysis was used to understand the phase evolution in the system using the samples processed at temperatures ranging from 698 K to 873 K (with no hold at temperature). Figure 4.1 shows a clear change in phase composition, i.e. the cubic/trigonal phase ratio. The powder starts as a mixture of cubic and trigonal phases,

and as the processing temperature increases, the peak intensities from the cubic phase decrease relative to those from the trigonal phase. By 773 K, the material is almost pure trigonal phase.

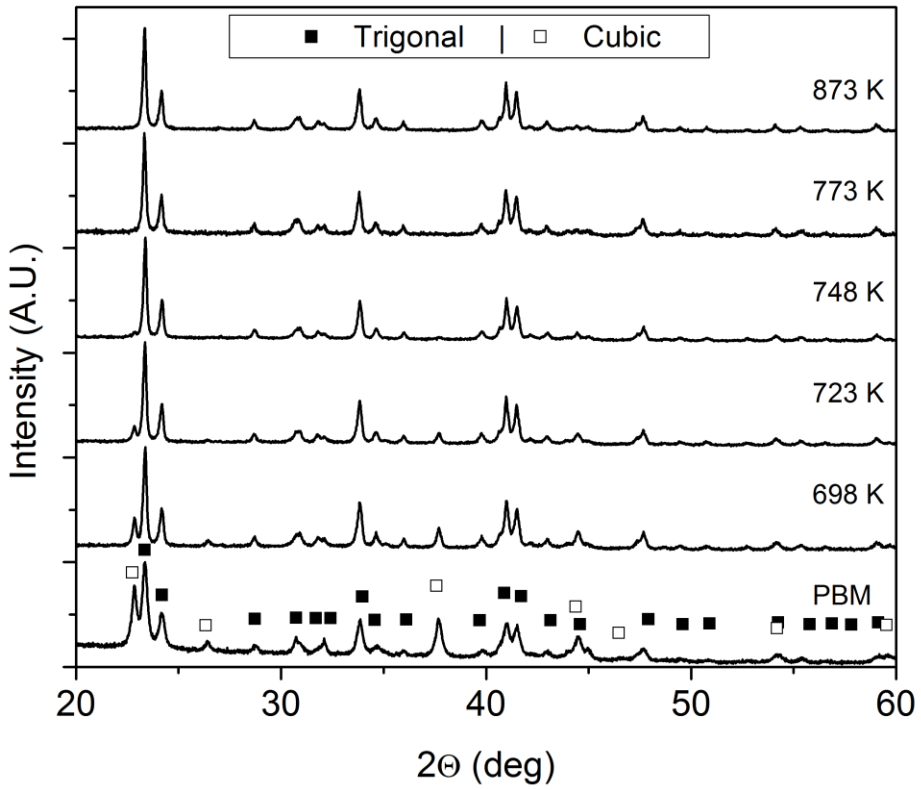

Figure 4.1 X-ray diffraction patterns of samples CAPAD-processed at varying temperatures with no-hold. The pattern from the starting planetary ball milled powder (PBM) is shown at the bottom. Diffraction peaks from the trigonal and cubic phases are labeled with closed square and open square symbols, respectively.

The densification behavior and phase evolution from a mixture of cubic and trigonal phases to a nearly pure cubic phase can be seen in Figure 4.2, showing the fraction of the trigonal phase determined from Rietveld analysis of the XRD data as well as measured densities of the materials. Roughly one third (from 64 to 78% which is compared with the 64 to 100% range) of the remaining transformation occurs at processing temperatures below 698 K. The overall density also changes drastically during this period. Samples processed at 698 K show a density approaching 3.8 g/cm3, with minimal change in density above that temperature. We will refer to temperatures below 650 K as the densification dominated stage. The densities of the cubic and trigonal phases are 3.6 g/cm^3 and 4 g/cm^3, respectively. The porosity can be estimated using a rule of mixtures to calculate the theoretical density of the composite. Using data in Figure 4.2, the material processed at 698 K has an estimated porosity of 2.9% and processing at 748 K results in an estimated porosity of 4.8%. We attribute this increase in porosity to the cubic phase transforming into the denser trigonal phase.

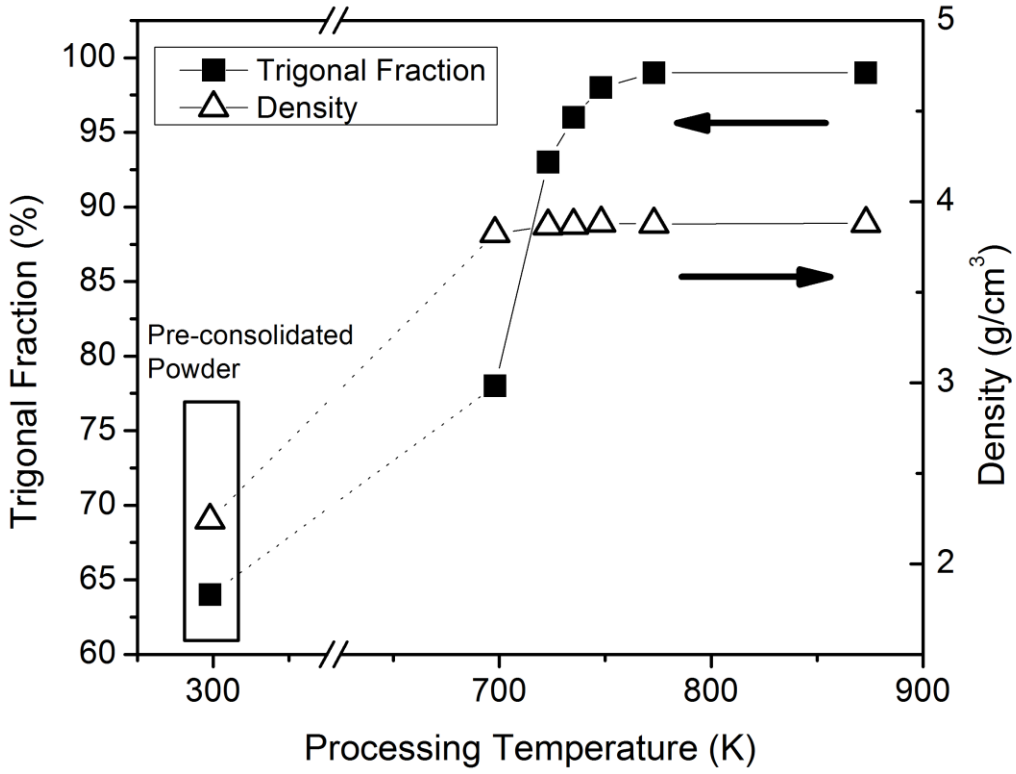

Figure 4.2 Trigonal phase fractions (closed squares) and measured densities (open triangles) of materials processed at temperatures varying from 698 K to 873 K with no hold at temperature.

4.3.1 Densification Kinetics

Figure 4.3a shows variation of the density of the material with processing temperature from a typical no-hold experiment. In the first section (marked as I), the pressure is increased up to 112 MPa and a low heating current is applied, bringing the temperature to stabilize the system at 373 K. The data shows that the material begins

densifying at processing temperatures below 350 K (T/T_m = 0.3). The melting temperature (Tm = 1043 K) of Mg_2Sn is used for reference [14]. In sections II and III of Figure 4.3, the pressure was constant at 112 MPa but the samples were continuously being heated at a rate of 200 K/min up to the hold temperature. The density continued to increase through section II; so sections I and II are considered to be densification dominated. In section III (shaded region in Figure 4.3a) we see an inflection point around 670 K which is caused by phase transformation as will be shown below. This will be referred to as the transformation dominated stage, as discussed later.

The variation of densification rate is presented in Figure 4.3b. The pressure loading portion (section I) causes an increase in densification rate but the maximum densification rate, is not reached until well after the maximum load has been applied (sections II and III). From the data in Figure 4.2, we know that simultaneous densification and phase transformation both occur at temperatures below 650 K, thus the main densification peaks are attributed towards densification caused by a combination of pore reduction and density changes caused by the cubic to trigonal transformation (the trigonal phase is denser than the cubic phase). In addition to the main densification peak, section II and also shows and a minor densification peak in Section II are mainly due to porosity reduction while the peak in Section III is dominated by phase transformation.

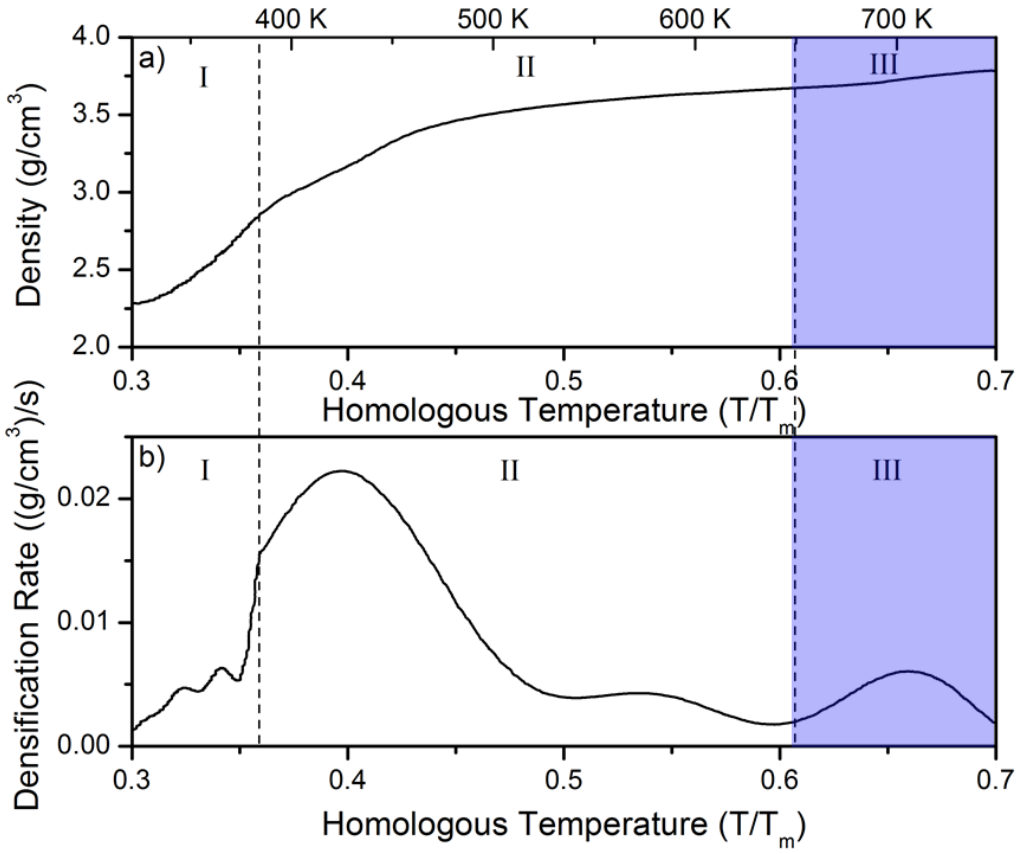

Figure 4.3 a) Density evolution during CAPAD processing as a function of homologous temperature. b) Densification rate variation as a function of homologous temperature. Section I shows the initial application of pressure to the material ranging from 0 to 112 MPa and slow heating from room temperature to 373 K. Sections II and III show the constant heating of the material at 200 K/min with a constant pressure of 112 MPa. Section III is highlighted to differentiate between densification and transformation dominated regions.

The highest densification rate is 2.2 ×10-2 g/(cm^3·s) and occurs at T/T_m ~0.4. Considering the theoretical densities of the cubic and trigonal phases are 3.6 g/cm^3 and 4 g/cm^3 respectively, the maximum relative densification rate, $\dot{\rho}_{Max}$, is ~ 5.5 ×10^{-3} s^{-1}. The magnitude of this maximum densification rate is very similar to those measured for Si, Al

and yttria-stabilized zirconia (YSZ) [38]. However, $\dot{\rho}_{Max}$ occurs at a significantly lower T/T_m for this Mg-Sn system compared to that of the Al, Si and YSZ systems [38]. This observation is consistent with previous work which shows that mechanically activated powders can be consolidated at significantly lower temperatures than non-activated powder [71]. Another major difference from the previously reported pure densification experiments is that this Mg-Sn curve shows 3 different peaks; Si and YSZ show only one and the metal Al shows only 2. We can attribute the additional peak to the densification caused by the cubic-to-trigonal phase transformation (which is absent in Al, Si and YSZ), as opposed to the traditional densification caused only by reduction in porosity.

4.3.2 Transformation Kinetics at a Constant Heating Rate

Since the material transforms from a mixture of cubic/trigonal phases to almost a pure trigonal phase, we will discuss the transformation progression relative to the trigonal phase, i.e. by considering the transformed fraction of the trigonal phase, α. Mg_2Sn is a line compound, not a sold solution in the phase diagram and thus is not expected to have a range of compositional variations. It is not known if the trigonal phase which is often assigned the stoichiometry of Mg_9Sn_5 is a line compound or if it has a range of compositional variations (although a range of composition may explain the inconsistencies in unit cell values [67]). Here, the cubic to trigonal transformation is treated as a polymorphic transformation i.e. we do not consider a change in stoichiometry. In order to decouple the changing material density with the phase

composition, the phase analysis is limited to processing temperatures of 698 K and above due to the similarities in overall material densities (see Figure 4.2).

Generally solid state transformations occur through a combination of nucleation and growth processes that typically show a sigmoidal response with temperatures (and time) i.e. they begin at a low transformed fraction, increase rapidly and then asymptote to 100% conversion (α = 100%). This sigmoidal type of curve is often referred as a Kolmogorov-Johnson-Mehl-Avrami (KJMA) curve. The acceleration and deceleration sections of the transformation process can be thought of as nucleation rate dominated and growth rate dominated sections, respectively.

Figure 4.2 shows that by processing the powder up to 698 K, the trigonal phase fraction, α, increases from 64% to 78%. The rest of the transformation (78% to 100%) occurs at processing temperatures exceeding 698 K. This portion occurs under a constant heating rate of 200 K/min. This heating rate is a commonly used heating rate in CAPAD experiments. Although, the magnitude of the heating rate could affect the kinetics, the effect of higher or lower heating rates is not known at this time.

Recently, Farjas and Roura modified the KJMA model to account for transformations occurring under constant heating rates [72]. According to their derivations, under a constant heating rate T', the transformed fraction can be described as:

$$\alpha = 1 - exp\left\{-\left[k_0 C \frac{E_{T'}}{T' k_B} p(x) \frac{E_{T'}}{k_B T}\right]^{m+1}\right\} \tag{4.2}$$

where k_0 and C are constants, k_B is the Boltzmann constant, T is the temperature, $(m + 1)$ is the Avrami exponent, $E_{T'}$ is the activation energy under the constant T' and $p(x)$ is a function that can be approximated with the equation:

$$p(x) \approx \frac{e^{-x}}{x^2} \tag{4.3}$$

The activation energy can be derived by fitting the experimental data to a logarithm version of Equation (4.2):

$$ln[-ln(1-\alpha)] = -1.051 \cdot (m+1)\frac{E_{T'}}{k_B T} + (m+1)\, ln\left(k_0 C \frac{E_{T'}}{T' k_B}\right) - 5.2813 \tag{4.4}$$

Equation 4 expresses a linear relation between $ln[-ln(1 - \alpha)]$ and the reciprocal temperature $(1/T)$ with a slope of $-1.051(m + 1)E_{T'}/k_B$. We use our data obtained under a constant heating rate (T'= 200 K/min) to construct such a plot (Figure 4.4). The data indeed shows excellent agreement with an adjusted correlation coefficient (R^2) of 0.973. The value of the activation energy is 77 kJ/mol using the Avrami exponent of $(m + 1) = 1$. This excellent linear fit suggests that our data follows the conditions for which the KJMA model was derived, i.e. for nucleation according to an exponential law (nucleation occurs as a random process rather than an instantaneous one) followed by rapid growth [73]–[76]. Thus it can be concluded that both nucleation and growth are important for the cubic-trigonal transformation at a constant heating rate. The Avrami exponent (shown here as $(m + 1) = 1$) also sheds some light on the type of growth that occurs during the transformation. Lower value exponents correspond to a linear growth whereas higher

values suggest a polyhedral growth [76]. Thus this suggests that the cubic to trigonal transformation proceeds via a linear growth mechanism under constant heating rate conditions.

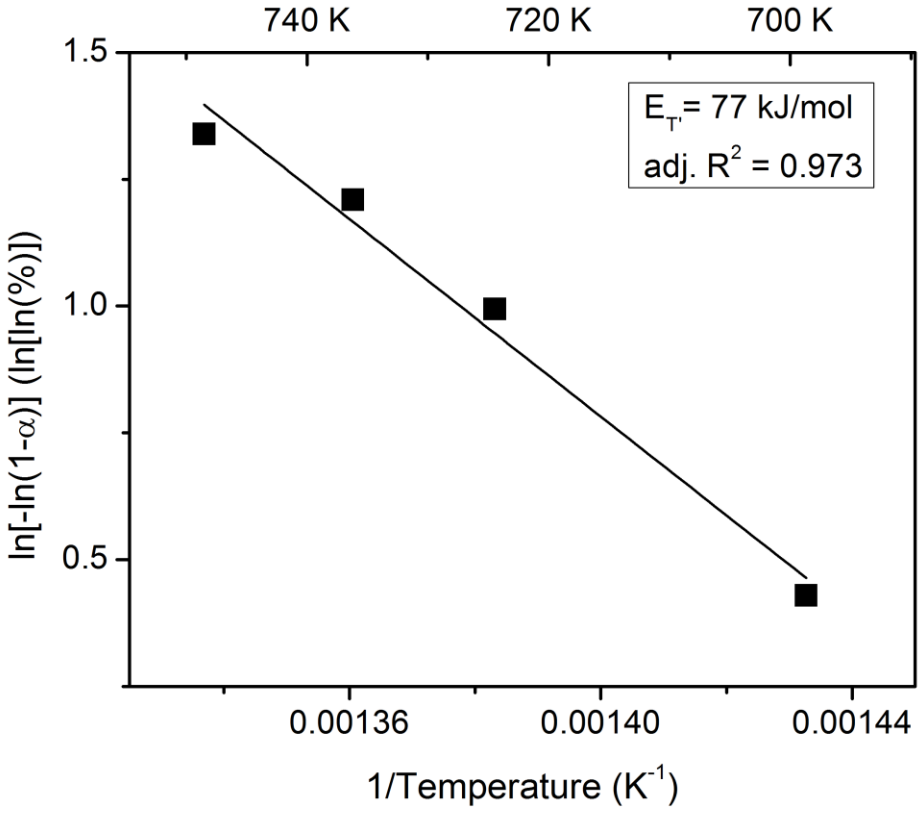

Figure 4.4 Temperature dependence (1/*T*) of the trigonal phase fraction (*ln*[*ln*(1 - α)]) for experiments conducted at a constant heating rate of 200 K/min. The activation energy is determined to be $E_{T'}$ = 77 kJ/mol with a correlation coefficient of 0.973.

Since most phase transformations require atomic/ionic diffusion, it is useful to compare our obtained activation energy for cubic-to-trigonal phase transformation with those for Mg/Sn diffusion. Unfortunately, there is no previous report on the Mg/Sn

diffusivities in the Mg-Sn system. Nevertheless, it is worth comparing our value with those of Mg/Sn diffusion in other systems. The activation energy of 77 kJ/mol is lower than the self-diffusion values of Mg (134 kJ/mol) [77] and Sn (106 kJ/mol) [78] for temperatures ranging from 741 to 900 K and 433 to 501 K, respectively. This difference is expected since the crystal structures of the pure metals are quite different from the anti-fluorite structure of Mg_2Sn with a dominant ionic character [16]. Oishi *et al* [79] has compiled a list of anion self-diffusion in materials with anti-fluorite structures which shows diffusion activation energies ranging from 74 - 130 kJ/mol for the extrinsic regime. The intrinsic regime energies are significantly higher (typically ~250 kJ/mol). The difference can be rationalized by considering that the activation energy for diffusion by vacancies, E_D, has two components: the energy of migration, E_M, and the energy of formation for vacancies, E_F, such that $E_D = E_M + E_F$. In the extrinsic case, the vacancies necessary for diffusion already exist requiring no E_F, i.e. $E_D = E_M$. The results are consistent with the low end of the extrinsic values for ED in fluorites. Xia *et al*. recently measured a similar activation energy (75 kJ/mol) to this study for the formation of precipitates in another Mg based system (Mg-Sm-Zn-Zr) using the same modified KJMA method that is used here [2]. They attributed the formation of their alloy to the vacancy migration in Mg. The relatively low activation energy measured suggests that the energy barrier for transformation is low and because of the similarities with extrinsic diffusivities it is hypothesized that the cubic to trigonal transformation is mainly governed by vacancy migration. Intrinsic diffusion occurs at higher temperatures where diffusion pathways are provided by thermally created defects. Extrinsic diffusion occurs at lower temperatures

where fewer thermal defects exist and the main diffusion pathway is through the constitutional defects in the lattice.

4.3.3 Transformation Kinetics at Isothermal Conditions

Three models are used to analyze the rate constants for the transformation from the cubic to trigonal phases under isothermal conditions (varying hold time experiments). They are as follows:

$$\alpha = 1 - ce^{-kt^{m+1}} \tag{4.5}$$

$$\alpha = 1 - (kt + c)^3 \tag{4.6}$$

$$\alpha = 1 - \frac{1}{kt + c} \tag{4.7}$$

where c is a constant, t is the time elapsed, and k is the rate constant. Equation (4.5) (KJMA model, $(m + 1) = 1$) is derived for nucleation according to an exponential law (nucleation occurs as a random process rather than an instantaneous one) followed by rapid growth [73]–[76]. Equation (4.6) is derived for rapid nucleation (nucleation happens virtually all at the same time and completes within a short period) followed by rapid growth on the surface of spherical particles. Equation (4.7) is derived empirically as a 2nd order kinetics model from the base form:

$$-\frac{d\alpha}{dt} = k\alpha^n \tag{4.8}$$

where n is an integer (n = 0, 1, 2, etc.) and n = 2 in this case.

Figure 4.5 shows increases in the trigonal phase fraction. Processing at lower temperatures, compared to higher temperatures, requires significantly longer times to progress the transformation. Each of the three models (Equations (4.5), (4.6), and (4.7)) is fitted to the experimental data using a non-linear least squares regression. A summary of the rate constants calculated using these models along with their correlation coefficients are listed in Table 4.1. Equation (4.6) shows the lowest correlation coefficients (ranging from 0.790 to 0.925) for each of the processing temperatures. Equation (4.5) shows an improved correlation (ranging from 0.836 to 0.958) with each processing temperature. And Equation (4.7) shows the highest correlation with the data (ranging from 0.923 to 0.969) for all processing temperatures.

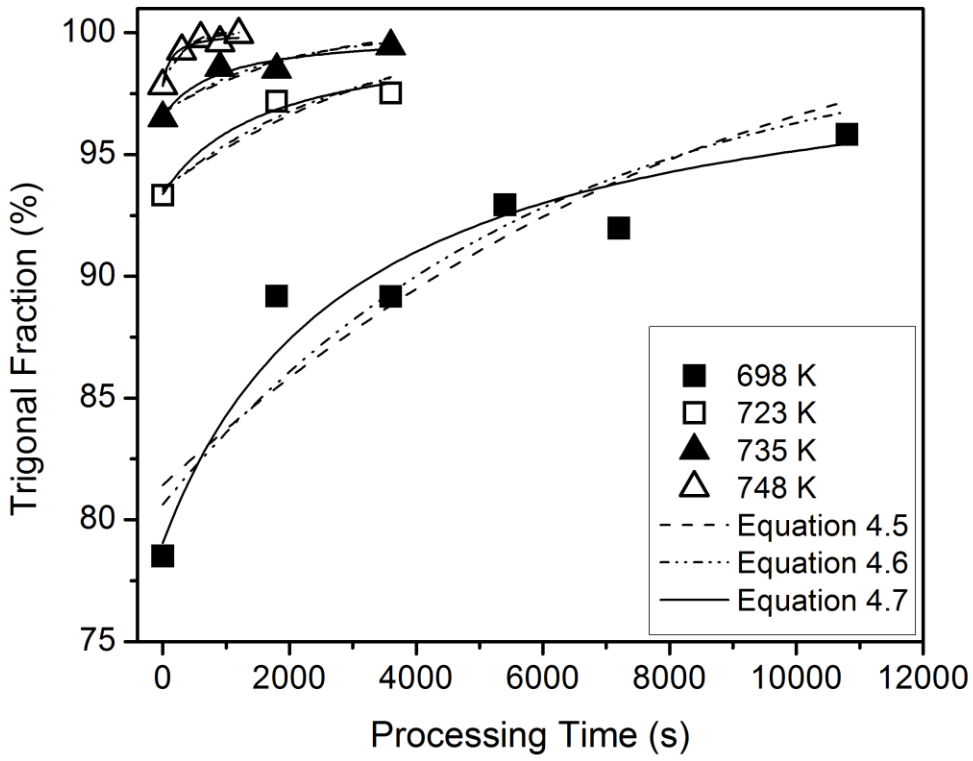

Figure 4.5 Trigonal phase fractions of materials processed isothermally with varying times. Equations 5, 6, and 7 are used to fit the data.

Since the R^2 values are low, we believe that Equations (4.5) and (4.6) do not adequately capture our measured data, i.e. the transformation according to these isothermal conditions does not follow the assumptions of these models. It should be noted that higher value exponents in Equation (4.5) were considered, but their correlation coefficients were lower than the ones presented here. It is likely that by the time that the materials have reached these temperatures (isothermal conditions of these experiments),

the vast majority of the nucleation of the product (trigonal) phase has already taken place, and only subsequent growth is operational.

By contrast, the correlation values for the fits using Equation (4.7) are uniformly high and thus this model adequately captures our data. Figure 4.6 shows an Arrhenius plot of the rate constants *k* calculated using Equation (4.7). The activation energy value obtained under isothermal conditions, E_T is 448 kJ/mol, with a correlation value of 0.901. These rate constants can also be used to estimate the amount of time required for the transformation to reach a 99% completion ($t_{99\%}$) at certain temperatures (Table 4.2).

The activation energy obtained under isothermal conditions using Equation (4.7) (E_T = 448 kJ/mol) is much higher than the one from experiments at a constant heating rate of 200 K/min ($E_{T'}$ = 77 kJ/mol). The difference is caused by the significantly different degree of completion of the transformation reaction. In the constant heating rate experiments, α ranges from 78 to 98%. While in the isothermal experiments, the reaction is significantly more advanced especially at higher temperatures. For example, the 735 K isotherm ranges from 96 to 99% and the 748 K isotherm encompasses only 98 to 100%. It is likely that at the latter stage of the reaction the reacted phases could have impinged on one another, making it more difficult for the reaction to proceed. As mentioned previously, Equation (4.7) was derived empirically and thus does not provide insight into the transformation mechanism. Nonetheless, the activation energy analysis is useful for understanding the phase transformation kinetics under varying hold times. Specifically

these results can potentially be used to tune the composition of dense biphasic composites.

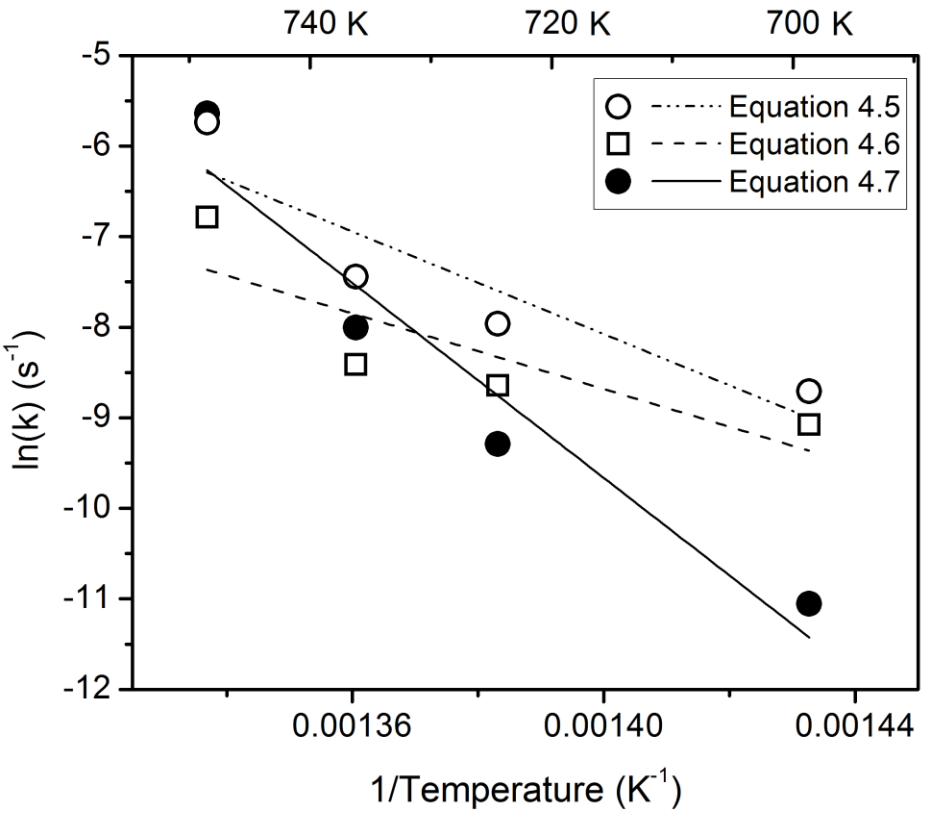

Figure 4.6 Temperature dependence for isothermal, varying time experiments. The rate constants were calculated according to Equation (4.7).

Table 4.1 Rate constants and adjusted correlation coefficients for the fitted curves.

Temperature (K)	Rate constants, k [s^{-1} x10^{-4}] (adj. R^2 values)		
	Eq. (4.5)	Eq. (4.6)	Eq. (4.7)
698	1.66 (0.836)	1.14 (0.790)	0.159 (0.923)
723	3.48 (0.845)	1.77 (0.781)	0.923 (0.948)
735	5.86 (0.856)	2.22 (0.803)	3.35 (0.925)
748	32.2 (0.958)	11.3 (0.925)	35.5 (0.969)

Table 4.2 Transformation time to 99% completion

Temperature (K)	Time to 99% completion, $t_{99\%}$ [s] Eq. (4.7)
698	59891
723	9200
735	2126
748	153

4.4 Conclusions

In summary, composite materials with varying ratios of the cubic and trigonal phases in the Mg-Sn system have been synthesized using a combination of ball milling and CAPAD. The process can be divided into densification dominated and transformation dominated stages. In the densification dominated stage the ball milled powder densifies via reduction of porosity and to a lesser extent from the phase transformation. The densification rate has the same order of magnitude as those determined previously on densifications without phase changes. However, we observe additional densification peaks, which are attributed to the cubic to tetragonal phase transformation. The majority of the phase transformation occurs during heating at a constant rate of 200 K/min. I used a modified KJMA model to derive the activation energy, which is 77 kJ/mol. Under isothermal conditions we find that the transformation follows a second order rate law and has a significantly higher activation energy.

Chapter 5 Transport Properties

5.1 Introduction

Utilizing waste heat from power generation sources remains a great challenge. Thermoelectric materials have the ability to directly convert heat energy into electrical energy. The efficiency of a thermoelectric device is determined by a dimensionless figure of merit, *ZT*:

$$ZT = \frac{S^2 \sigma T}{\kappa} \tag{5.1}$$

where S is the Seebeck coefficient, σ is the electrical conductivity, κ is the thermal conductivity (both lattice, κ_l and electrical, κ_e contributions), and T is the temperature. Higher *ZT*s are necessary to achieve higher conversion efficiencies. However, the three properties (S, σ, κ_e) are interdependent which makes improving *ZT* values difficult. Synthesizing a material with the ideal transport properties requires expertise in heavily doped semiconductors as well as the microstructural effects. One of the most successful approaches for achieving this has been to introduce nano-scale inclusions with coherent interfaces between inclusion and host material in order to reduce thermal conductivity while retaining a high electrical conductivity [80].

Mg based thermoelectric materials are attractive because they are composed of earth abundant elements and relatively non-toxic when compared to their state of the art counterparts, the Bi_2Te_3 and PbTe material systems. The $Mg_2Si_{1-x}Sn_x$ system (a solid

solution of cubic Mg_2Si and Mg_2Sn) has shown a promising figure of merit (~1.1) in the 600-870 K temperature range in recent years [4]. This is due to the low lattice thermal conductivity due to elemental alloy scattering effects, and unique band structure features.

However, the Mg_2X (X=Si,Sn,Ge) material systems have high pressure polymorphs first discovered by Cannon and Conlin in 1964 [28] which have not been studied for thermoelectric conversion. The Mg_2X material systems crystallize in the cubic anti-fluorite structure (Fm-3m) under ambient temperature and pressure conditions. Mg_2Sn was first shown to transform between the cubic and hexagonal crystal structures under pressure and temperature conditions exceeding 4 GPa and 400 °C [29]. In 1996, the crystal structure of the Mg_2Sn high pressure polymorph was shown to be trigonal (R3) with a stoichiometry of Mg_9Sn_5 [30]. More recently, the high pressure polymorph has been shown to form through a novel synthesis route combining high energy ball milling and powder consolidation at 600 °C and 112 MPa [67]. As of the time of this dissertation, no comprehensive study has been performed on the transport properties of the trigonal Mg_2Sn crystal structure.

Current activated pressure assisted densification (CAPAD) was chosen for this study because it is an excellent materials development platform. It is capable of a wide range of processing conditions which allow for the formation of non-equilibrium microstructures and phases [35], [67], [81], [82].

5.2 Experimental Details

Elemental Mg and Sn powders (Alfa Aesar, 99+% metal purity -325 mesh) in a 9:5 Mg:Sn stoichiometric ratio were planetary ball milled (Frisch Pulverisette 7) at 450 RPM using stainless steel jars and balls for a total of 48 hours at room temperature. The Mg powder, due to its ductility, was added in increments of ~200 mg until reaching the stoichiometric ratio in order to avoid agglomeration of the Mg with the walls of the jars [61], [67]. No intentional dopant powders were added to the system. The final ball to powder weight ratio was 10:1 and all powders and milling media was handled under an argon atmosphere.

A custom built CAPAD device was used to consolidate the powder into bulk samples [35]. Graphite die and punch sets similar to that described by Anselmi-Tamburini *et al* [62] were used to create 9.52 mm diameter disks. All samples were processed under vacuum ($<10^{-2}$ Torr) with an applied mechanical pressure of 112 MPa and temperatures ranging from 425 to 475 °C with a heating rate of 200 °C/min. The maximum heating currents were varied between 700 and 900 A.

XRD phase characterization was performed with a PANalytical Empyrean diffractometer using a Cu Kα X-ray source ($\lambda_{K\alpha1}$ = 1.54056 Å and $\lambda_{K\alpha2}$ = 1.54440 Å). Rietveld refinement was carried out using the GSAS program with the EXPGUI interface [46], [69]. The densities of the CAPAD processed samples were measured using the Archimedes method.

The thermal conductivities were measured using the steady state method where a heater is attached to one end of a rectangular bar and the temperature difference is measured by use of a differential thermocouple. The electrical conductivities were measured through use of a the 4-wire method. The rectangular bars were cut using a diamond saw and polished to a 800 grit surface finish. Copper lead wires were attached to the bars using a silver epoxy. A Stanford Research Systems SR830 lock-in amplifier with custom circuitry was used to analyze the electrical properties. Temperature was controlled in a specially fabricated vacuum cryo-chamber powered by a Stirling cooler.

5.3 Results and Discussions

5.3.1 Phase composition

Figure 5.1 shows the XRD patterns for the planetary ball milled powder and the bulk CAPAD processed samples at temperatures from 425 to 475 °C. Processing in this temperature range allowed for the greatest amount of Mg_2Sn cubic and trigonal structural sweep, considering the starting phase composition from the powder. The most intense Mg_2Sn cubic peak (111) at 23° 2Θ diminishes considerably with increasing processing temperature. By 475 °C, the cubic Mg_2Sn pattern is nearly extinguished. These results agree with the previous two chapters' (Chapter 3 and Chapter 4) results where CAPAD processing at temperatures above 500 °C produce a sample with a pure trigonal crystal structure. Figure 5.2 shows the Rietveld refinement calculated values for the amount of trigonal crystal structure obtained at each processing temperature. The sample processed

at 425 °C is composed of 78% of the trigonal structure while the sample processed at 475 °C is composed of 98% of the trigonal structure. Thus, the composition of the trigonal/cubic composites ranges from 78/22 to 98/2.

This temperature range was also chosen based on the previous chapter's (Chapter 4) results where the material displays only minor density change with CAPAD processing temperatures above 400 °C. The measured densities of each of these composite materials were 3.82 ± 0.02 g/cm^3.

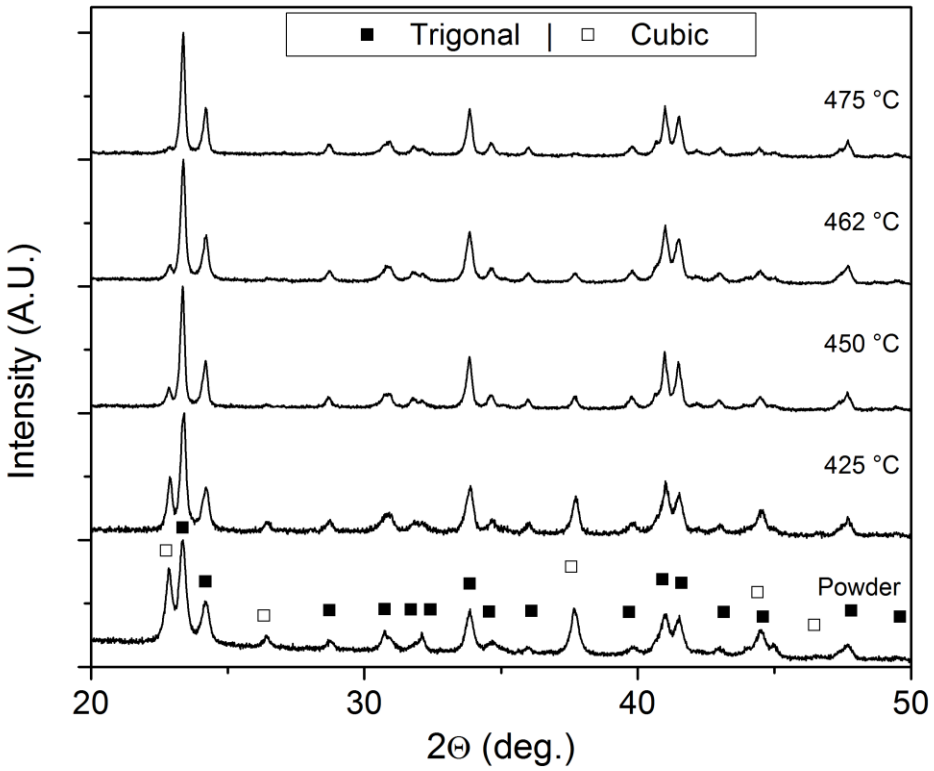

Figure 5.1 XRD patterns of the planetary ball milled powder and CAPAD bulk samples.

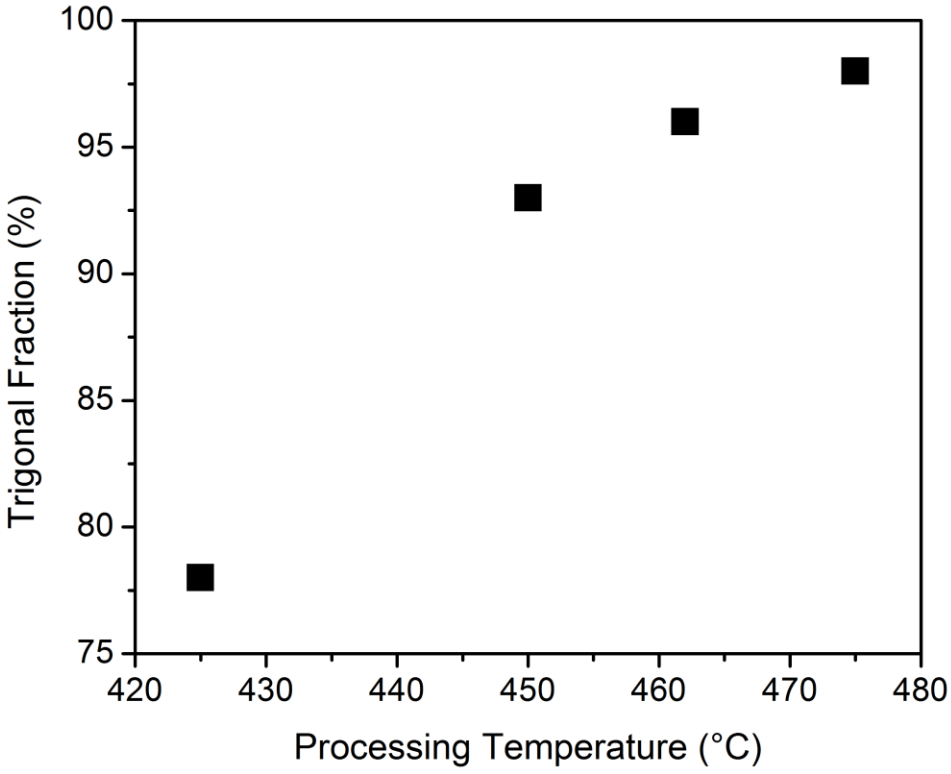

Figure 5.2 Trigonal fraction of the samples as a result of CAPAD processing temperature. The composition of the trigonal/cubic composites ranges from 78/22 to 98/2.

5.3.2 Electrical Conductivity

Intrinsic (non-doped) cubic Mg_2Sn is a narrow band gap semiconductor with a reported gap of E_g= 0.16 to 0.33 eV [25], [83]–[86] using electrical, optical, and

photoconductivity measurement techniques. Intrinsic trigonal Mg_2Sn has been qualitatively described as having a semiconductor electronic behavior [28], [31] but no quantitative measurements are available.

Figure 5.3 shows the measured electrical conductivities of the trigonal/cubic composites synthesized in this study along with a values measured by Song *et al*. [7] for a nominally undoped polycrystalline cubic Mg_2Sn through a powder synthesis and consolidation route. We will henceforth refer to Song's material as 'pure cubic' to contrast our trigonal/cubic composites. The electrical conductivity of the 78% trigonal composite (blue triangles) shows an increasing conductivity (semiconducting behavior) throughout the 160 to 425 K temperature range. The samples with 93 and 96% trigonal phase show a slight increase in electrical conductivity from 160 to 425 K. The sample with 98% trigonal phase shows a decreasing electrical conductivity (metallic behavior) from 160 to 373 K and leveling out to 425 K. It appears that as the trigonal phase fraction increases, the composite system's electrical conductivity evolves from a semimetal to a more metallic behavior. The values of the electrical conductivities are all higher compared to the intrinsic cubic Mg_2Sn study published by Song *et al.* [7].

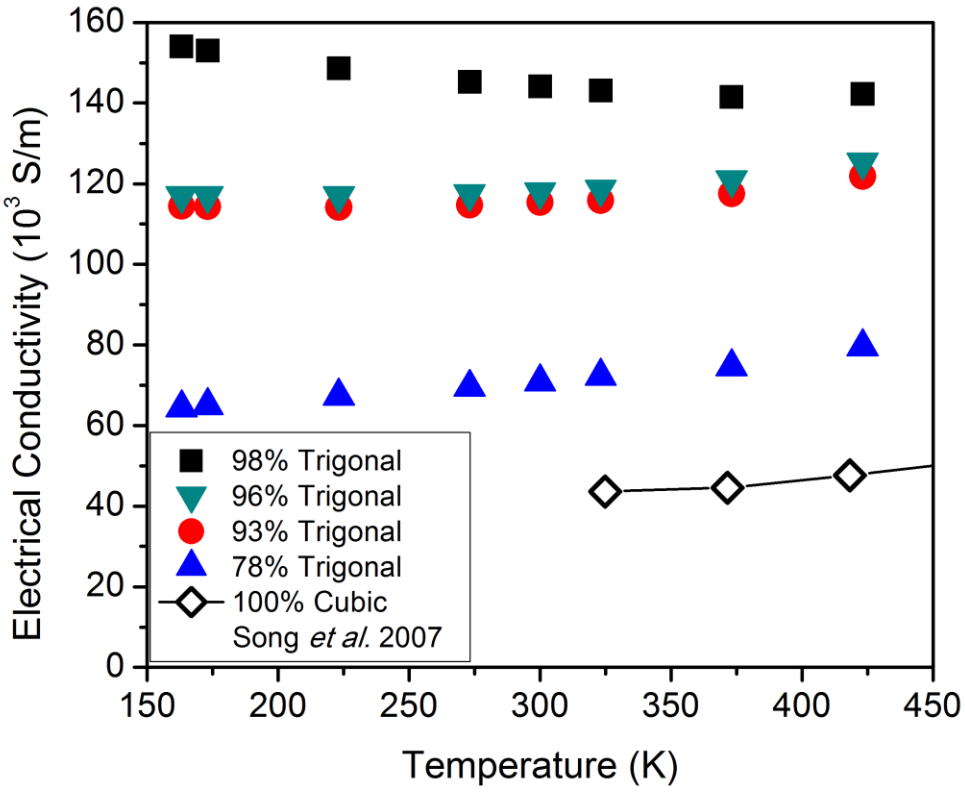

Figure 5.3 Electrical conductivities with temperature for the materials with different phase compositions.

One useful relationship for analyzing a semiconductor's electronic behavior with temperature is the Arrhenius relationship. For a single carrier (electrons or holes) intrinsic semiconductor, the change in electrical conductivity is related to its band gap (E_g) using the following relationship:

$$\sigma = \sigma_0 e^{-E_g/2k_BT} \tag{5.2}$$

where σ_0 is the material's reference electrical conductivity at a specific temperature, k_B is the Boltzmann constant, and T is the temperature of the material. This equation can be rearranged to show $ln(\sigma)$ vs $1/T$ as shown in Figure 5.4 for the 78% trigonal sample. Ideally, the data should show a linear decreasing trend with $1/T$; however, this is not the case for the 78% trigonal sample. Since the other samples (93, 96, and 98% trigonal) show mixed semiconducting and semimetallic behaviors, it is likely that multiple charge carriers (i.e. both electrons and holes) are responsible for the total electrical conductivity.

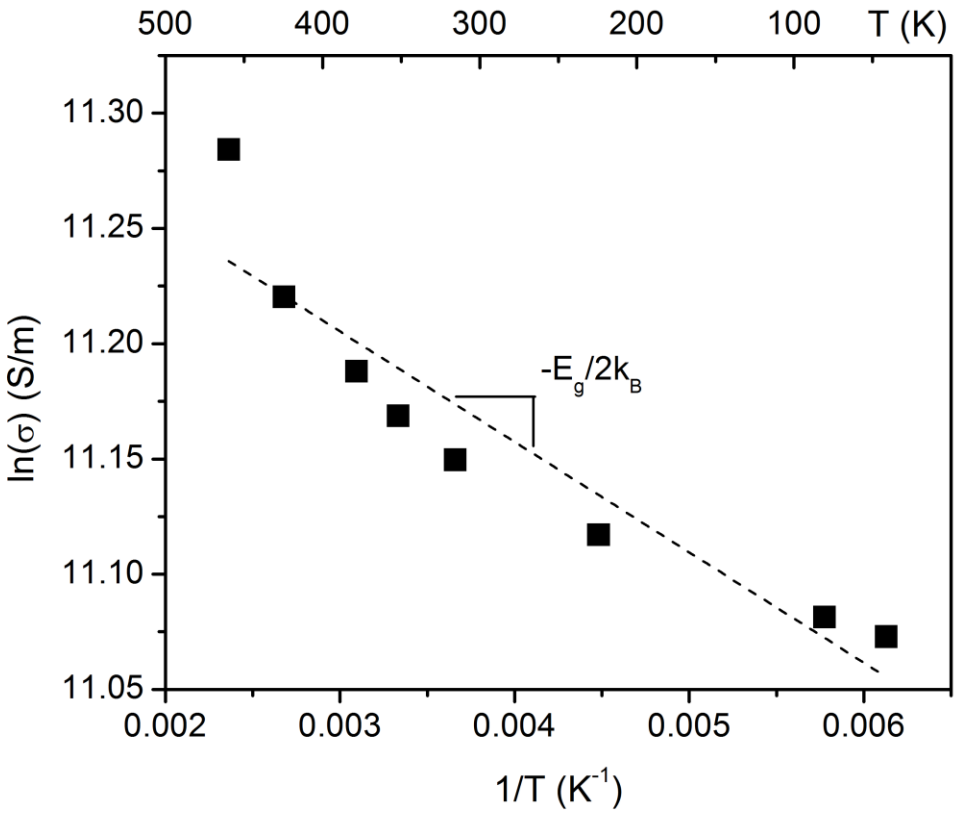

Figure 5.4 Arrhenius plot of the 78% trigonal sample.

5.3.3 Thermal Conductivity

The thermal conductivities of all trigonal/cubic composites show an increasing value from 160 to 425 K (Figure 5.5). The thermal conductivities of the samples range from 2.1 to 2.4 W/m.K at 163 K with the 96% trigonal sample having the lowest value and the 78% trigonal sample showing the highest value. At 423 K, the 78% trigonal sample has the lowest value (4.1 W/m.K) while the 93% trigonal sample has the highest value (4.7 W/m.K). This increasing trend with temperature of the composites is the opposite compared to pure cubic Mg_2Sn from Song *et al.* [7] (polycrystalline, black line).

It is not uncommon for thermoelectric materials with high electrical conductivities to have a measurable electronic contribution to the thermal conductivity. The Wiedemann-Franz Law dictates that the thermal conductivity arising from charge carriers is proportional to its electrical conductivity such that:

$$\kappa_e = L\sigma T \tag{5.3}$$

where L is the Lorentz number ($L = 2.44 \times 10^{-8}$ $W\Omega K^{-2}$ for an ideal conductor).

The electronic contributions to the thermal conductivities for the samples are shown in Figure 5.6 using the Equation (5.3). The electronic thermal conductivities show an increase ranging from 0.6 to 0.9 W/m.K for the 78% and 98% trigonal. This is less than half of the overall thermal conductivity increase for the samples whose values increase more than 2 W/m.K in this temperature range.

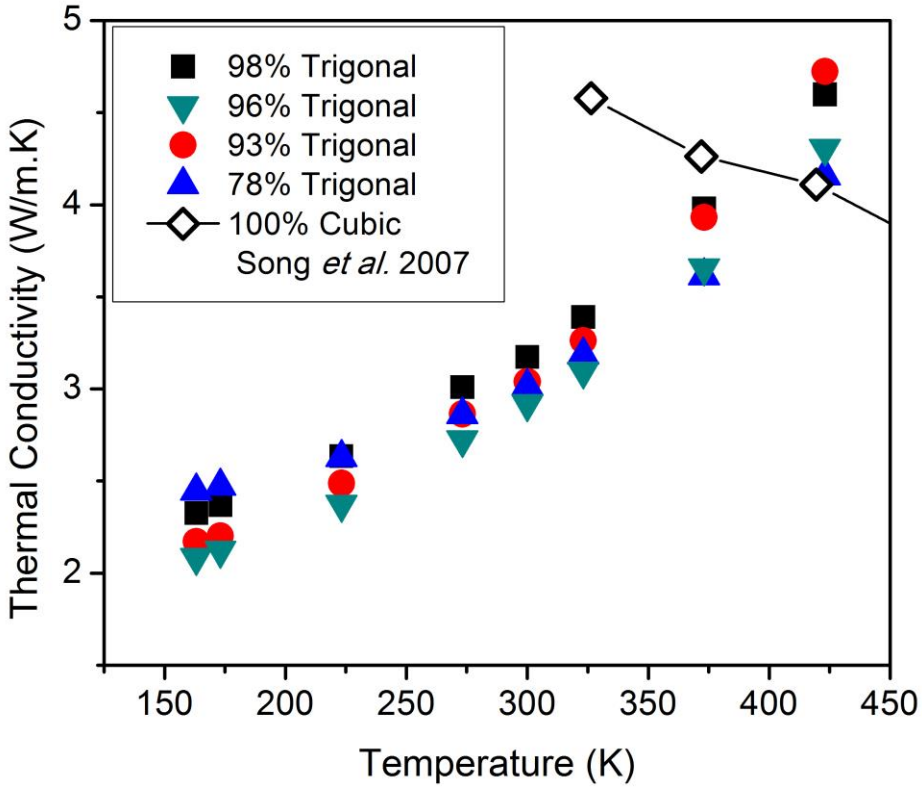

Figure 5.5 Thermal conductivities with temperature for the materials with different phase compositions.

The large increase in thermal conductivity shows behavior similar to ambipolar or bipolar conduction theories where both the majority and minority carriers (electrons and holes) contribute towards heat conduction in a manner greater than the sum of the two [87]–[93]. In this case, the charge carriers both travel down the temperature gradient and heat is released upon their recombination. In the acoustic scattering case between

electrons and holes, the total electronic thermal conductivity (both the ordinary Wiedmann-Franz law and the bipolar term) can be expressed as [26]:

$$\kappa_e = \left(\frac{k_B}{q}\right)^2 \left[2 + \frac{\left(4 + E_g/k_B T\right)^2 n_n n_p b}{\left(b n_n + n_p\right)}\right] \sigma T \tag{5.4}$$

where k_B is Boltzmann's constant, q is the electric charge, E_g is the band gap, T is the temperature, n_n and n_p are the electron and hole concentrations, b is the mobility ratio between electrons and holes, and σ is the electrical conductivity. Reports on pure cubic Mg_2Sn have also show the bipolar thermal conductivity behavior, but at higher temperature ranges [5], [26], [94], [95].

The bipolar term can also be expressed in terms of the partial electrical conductivities and Seebeck coefficients of each type of charge carrier [96]:

$$\kappa_e = \kappa_{e,n} + \kappa_{e,p} + \frac{\sigma_n \sigma_p}{\sigma_n + \sigma_p}\left(S_n + S_p\right)^2 T \tag{5.5}$$

where the first two terms ($\kappa_{e,n}$ and $\kappa_{e,p}$) are the thermal conductivities representing the kinetic energy transferred by both charge carriers. The last term incorporates the transport of energy due to the recombination of the electron and hole pairs. The recombination energy is normally expected to be one to two orders of magnitude higher than the kinetic energy terms in intrinsic semiconductors with band gaps ranging from 0.1 to 1.0 eV.

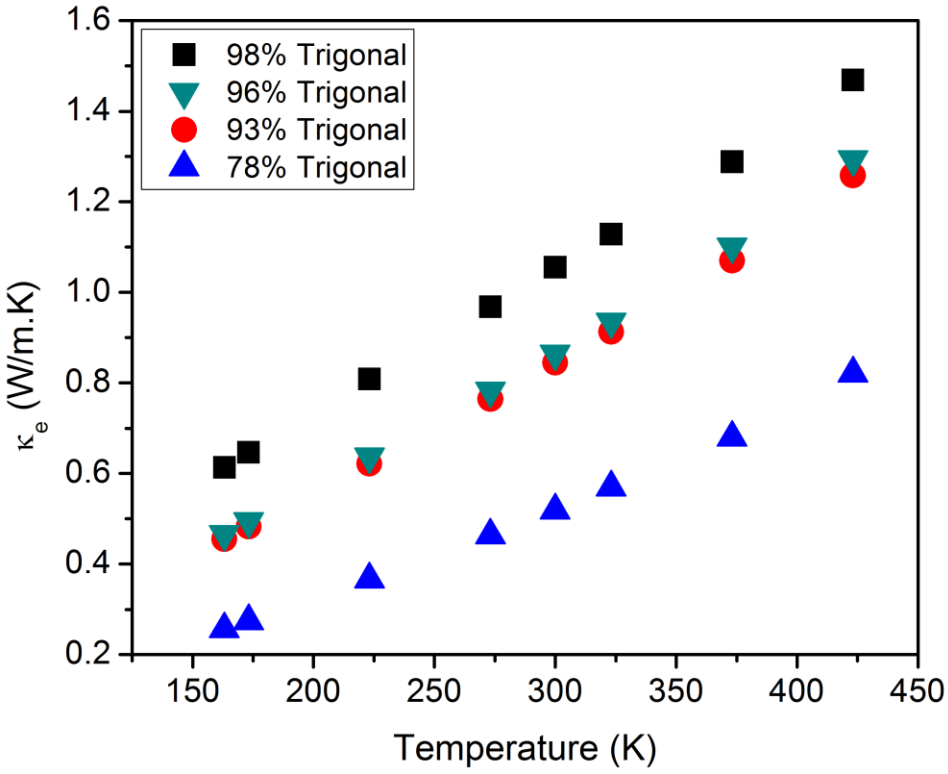

Figure 5.6 Electronic contribution to the thermal conductivity using the Wiedemann-Franz Law.

5.3.4 Seebeck Coefficient

Figure 5.7 shows that the Seebeck coefficients for the trigonal increase with increasing temperature. The maximum value obtained is 48 μV/K at 423 K. This trend is opposite of the pure cubic Mg_2Sn where the Seebeck coefficient decreased with increasing temperature [7].

For highly doped semiconductors, the Pisarenko relationship dictates that higher carrier concentrations decrease the Seebeck coefficient [97]. The carrier concentrations of the samples have not been measured at this time. However, a rough approximation can be made using the electrical conductivity where it is assumed that changes in the electrical conductivity receives negligible contribution from the carrier mobility and the overall values are dependent on the carrier concentration multiplied by a constant ($\sigma \propto n$). Figure 5.8 shows the Seebeck coefficients vs the electrical conductivities of the composites at various temperatures. These Seebeck coefficients decrease with increasing conductivity which is in agreement with the Pisarenko relation. The slopes of the curves can be indicative of any changes in charge carrier effective mass.

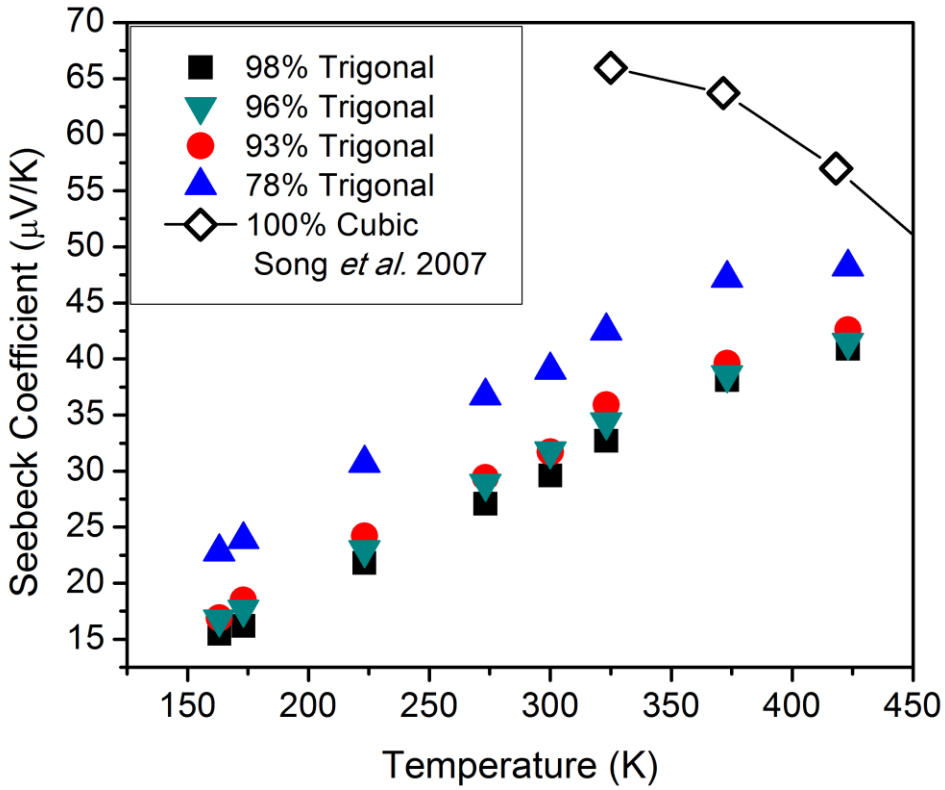

Figure 5.7 Seebeck coefficients with temperature for the materials with different phase compositions.

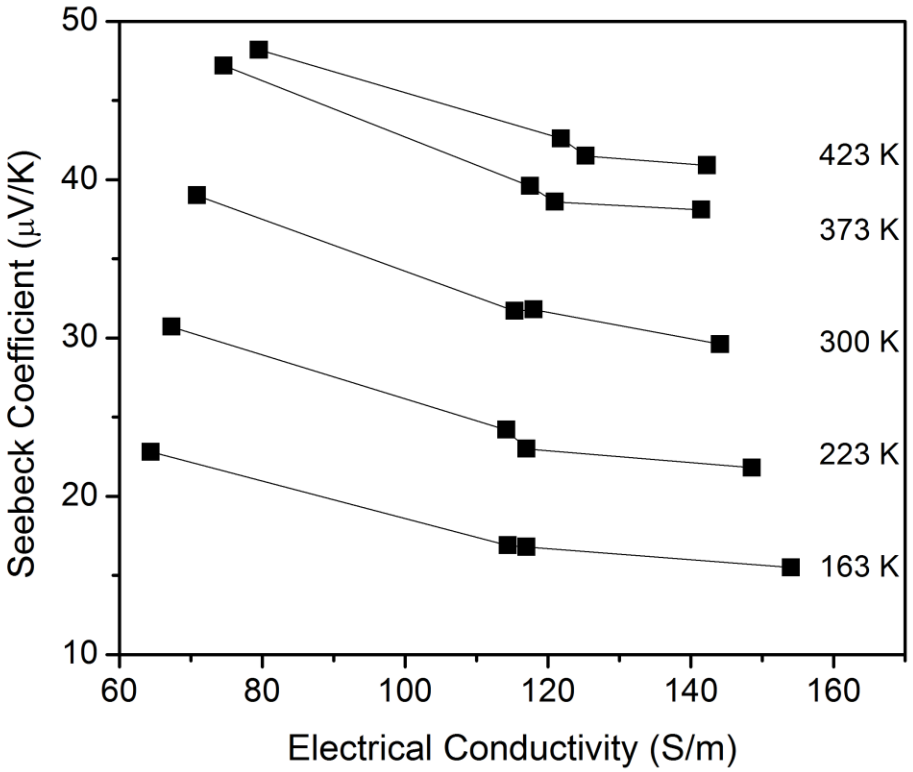

Figure 5.8 Pisarenko style plot at various temperatures

5.3.5 Figure of Merit

Figure 5.9 shows the ZT values for each of the trigonal and cubic Mg_2Sn phase composites with temperature. The ZT values for these composites increase with temperature within this range. At 423 K, the 98/2 composite shows an improvement of 13% over the 78/22 composition.

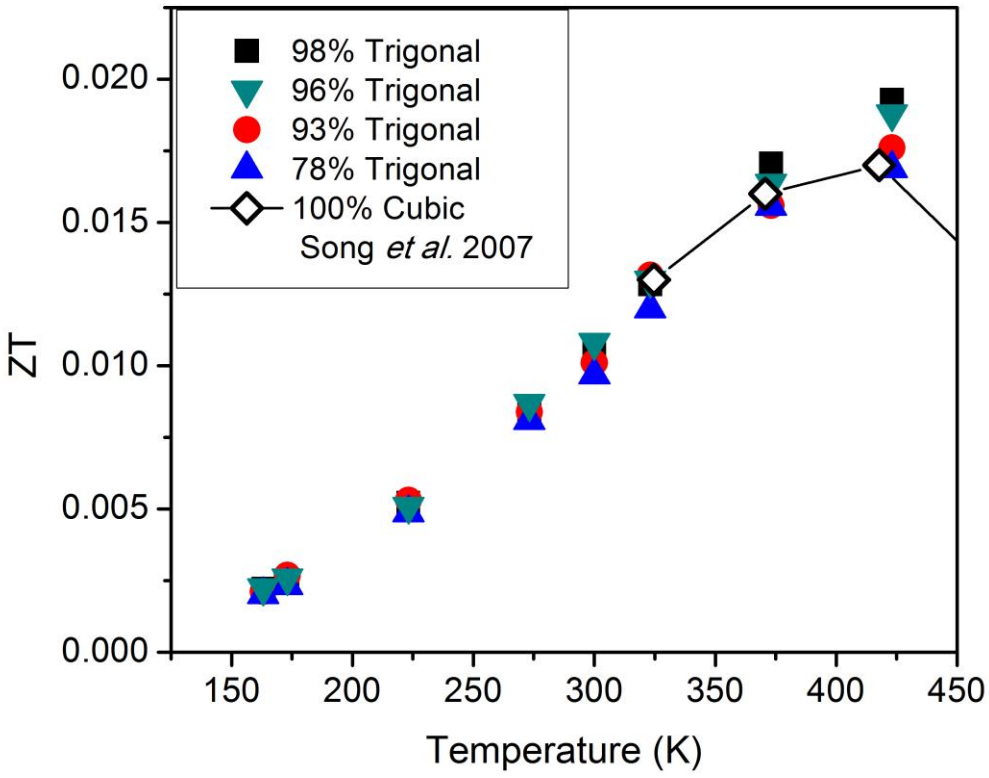

Figure 5.9 Figure of merit (ZT) with temperature for the materials with different phase compositions.

The effect of phase composition on the properties at 300 K can be readily seen in Figure 5.10. All of the properties show a perturbation in trend in the 96% trigonal composition sample. The electrical conductivity does not increase as drastically and the thermal conductivity is slightly lower as well as a slight increase in Seebeck coefficent. This may indicate a decrease in charge carriers at this composition. The ZT also changes

accordingly as seen in Figure 5.11 where the 300 K curve shows a local maximum with the 96% trigonal composition.

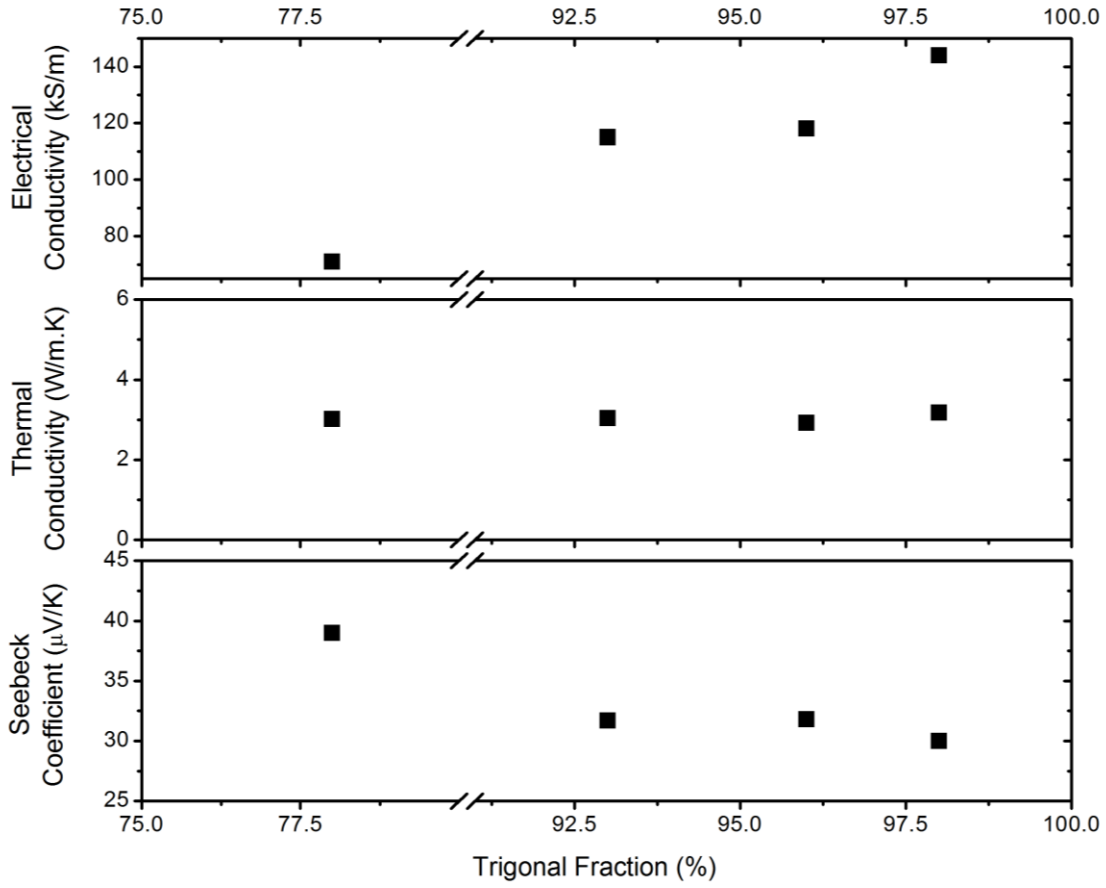

Figure 5.10 Electrical conductivity, thermal conductivity, and Seebeck coefficients vs. trigonal fraction at 300 K.

Figure 5.11 shows how ZT changes with composition at different temperatures. The curves for 373 and 423 K show an overall increase in ZT with an increasing phase

compositional amount of trigonal fraction. The difference in local ZT maxima for each temperature suggests that there are multiple competing mechanisms for the properties at different temperatures. The influence of charge carriers being promoted at different temperatures is evident based on Figure 5.3 where the 78% trigonal sample shows a semiconducting behavior with temperature while the 98% trigonal sample shows a semi-metallic behavior at lower temperatures.

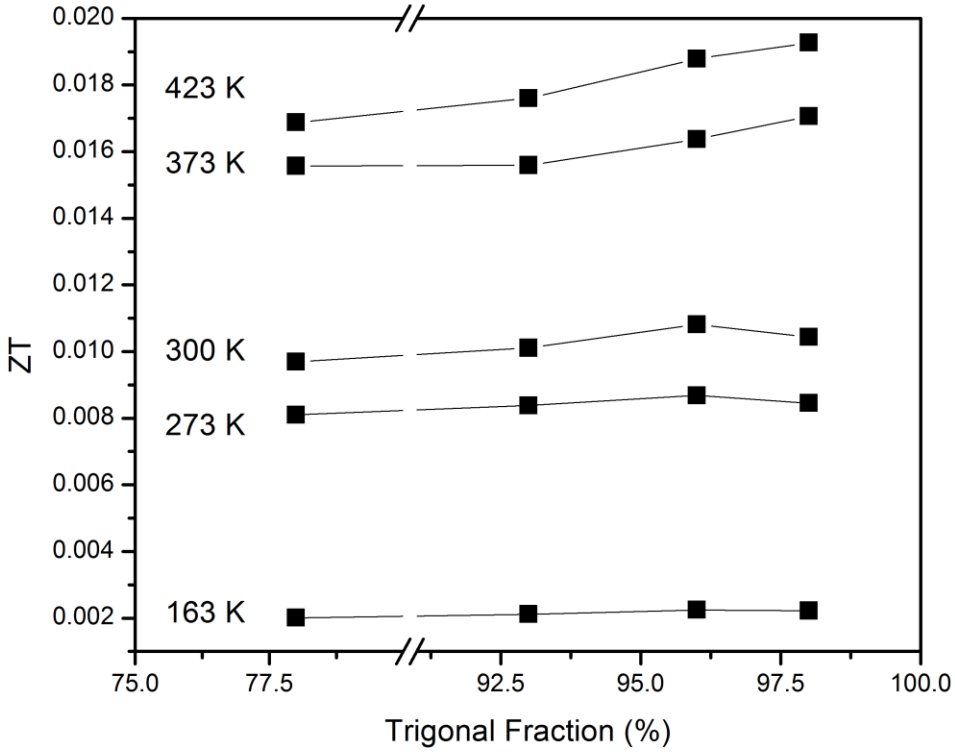

Figure 5.11 ZT at multiple temperatures as a function of trigonal fraction

5.4 Conclusions

This work contains the first report of transport properties for Mg_2Sn materials containing the metastable trigonal phase. The effect of processing conditions was investigated on the formation of the trigonal polymorph. A clear difference in electronic behavior in the samples with varying amounts of the trigonal phase show a semiconducting behavior to semi-metallic behavior. The thermal conductivity shows evidence of multiple charge carriers which contribute to a bipolar conductivity at lower temperatures than previously reported cubic Mg_2Sn based material systems. The Seebeck coefficients increase with increasing temperature which is commonly seen in heavily doped Mg_2Sn based material systems. Samples with higher amounts of the trigonal Mg_2Sn phase (98% vs 78%) show a13% increase of ZT at 423 K.

Chapter 6 Conclusions and Future Works

I am satisfied with the work that I have been able to accomplish during my tenure as a graduate student. The Mg-Sn material system has presented a great many challenges and revelations about the synthesis and processing of metastable materials.

Previous studies on the Mg-Sn material system have not shown the combined effects of powder ball milling and consolidation on the formation of the trigonal form of Mg_2Sn. As a result, my work contains the first reports on the transformation kinetics and transport properties of the metastable trigonal Mg_2Sn polymorph.

However, scientific work is never finished. There are always new phenomena to discover. I have not addressed the stability of the Mg_2Sn trigonal phase at elevated temperatures. Previous work reports that the trigonal phase transforms back into the cubic phase at temperatures above 400° C and ambient pressure [29]. I have taken my trigonal Mg_2Sn bulk samples to the NIST Center for Neutron Research (NCNR) and Argonne National Laboratory's Advance Photon Source (APS) for preliminary high resolution in-situ diffraction studies at high temperatures. The results from both institutions show that the trigonal crystal structure, once synthesized, is the dominant phase when heated to 600 °C at ambient pressure. Only when the material is cooled back to room temperature, does it transform back into the cubic phase (Figure 6.1). The transformation takes place in the temperature range from 500 to 400 °C.

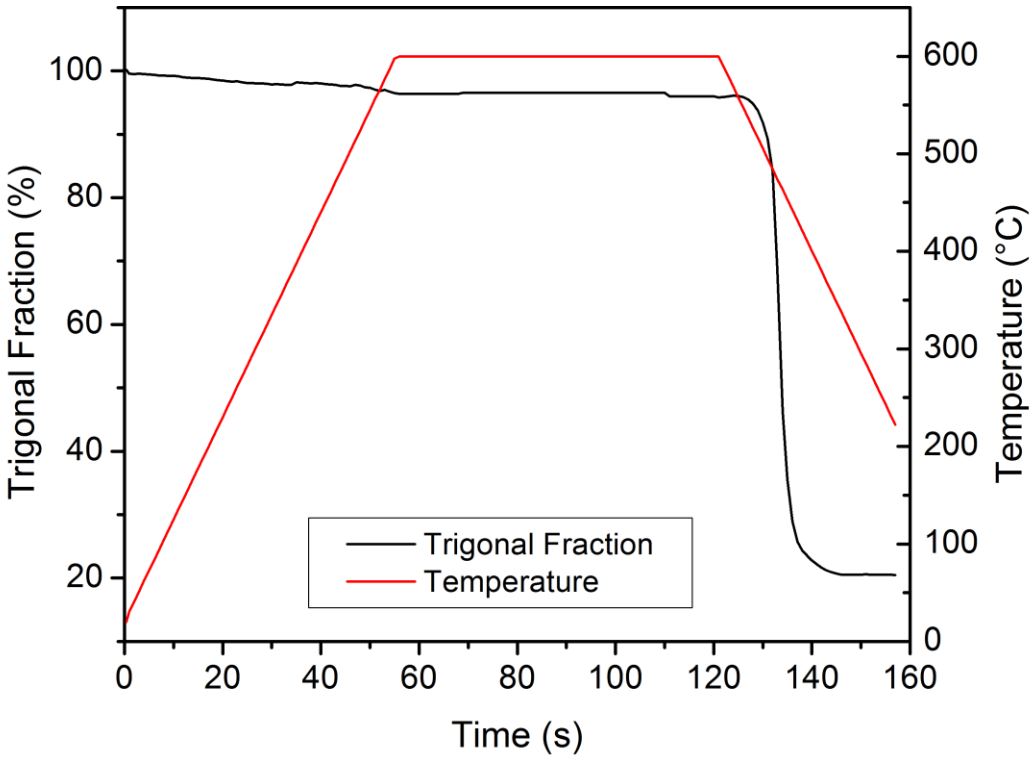

Figure 6.1 Trigonal fraction from in-situ high temperature diffraction experiment at APS

The heats of transformation can also be investigated through the use of high temperature calorimetry. There may be also an effect of the grain size which stems from high energy ball milling the starting powder.

Appendices

Appendix A. Thermal Annealing for Cubic Mg_2Sn

The cubic Mg_2Sn phase has been synthesized through a type of thermal annealing and reaction process known as Self-Propagating High-Temperature Synthesis (SHS) [19]. A similar reaction pathway was investigated to synthesize the cubic Mg_2Sn phase from elemental magnesium and tin powders. This was done as opposed to a more traditional melting synthesis in order to preserve the starting powder forms of the magnesium and tin.

The reaction temperature between magnesium and tin was analyzed using a TA Instruments SDT-Q600 which simultaneously measures weight change (thermogravimetric analysis – TGA) and differential heat flow (differential scanning calorimetry – DSC). Magnesium and tin powders with a stoichiometric ratio of 2.2:1 were pressed into a pellet with a rough density of ~2.0 g/cm^3 inside an argon filled glove box. The pellet was heated under a 50 mL/min flow of argon from 25 to 1000 °C at 10 °C/min.

Figure A-1 shows the weight change, heat flow, and temperature of the material during the heating process. The endothermic heat signal around 229.1 °C corresponds to the melting temperature of tin. The area under the curve does not match the heat of melting for tin which suggests that The large exothermic peak at 535.3 °C corresponds to

the heat of formation for 2 Mg + Sn → Mg_2Sn. The value is 75.4 kJ/mol which is in agreement with the reported literature values [14], [98]. The endothermic peaks correspond to the melting temperature of tin and heat of melting for Mg_2Sn at 229.1 °C and 766.59 °C, respectively. Mg_2Sn has been reported to melt congruently which was not seen during this SDT experiment [14]. One reason may be the drastic weight loss occurring just before the melting which indicates that magnesium may be evaporating. Another reason may be due to any local stoichiometric inhomogeneity from the solid state reaction. This SDT data was used to determine the thermal annealing temperature to synthesize the cubic Mg_2Sn intermetallic compound in powder form.

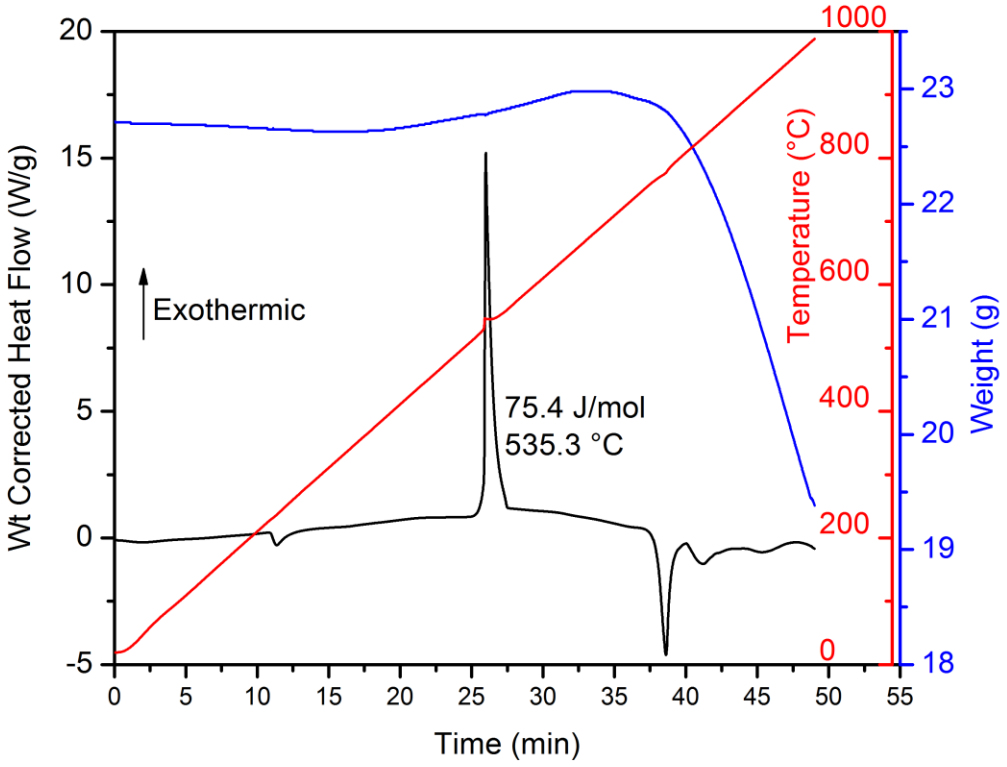

Figure A-1 SDT data showing heat flow, weight change, and temperature as a function of time.

Appendix B. Ball Milling

Cubic Mg_2Sn powder was synthesized using elemental magnesium and tin powders in a 2.2:1 stoichiometric ratio. The excess magnesium was added in order to mitigate any deficiencies due to the high rate of magnesium evaporation. The powders were well mixed in an argon atmosphere and heated in a graphite crucible under a flow of

argon. Based on the heat treatment results from Appendix A, the powder mix was brought up to 600 °C and held at temperature for 12 hours.

This cubic Mg_2Sn powder was planetary ball milled in order to investigate the effects of ball milling time on the transformation from cubic Mg_2Sn to trigonal Mg_2Sn. Figure B-1 is a series of XRD patterns which show the change in crystal structure of Powder 1 as it is processed in the planetary ball mill. The bottom diffraction pattern is the starting condition of the powder with a pure cubic Mg_2Sn crystal structure. After 1 hour of ball milling, the diffraction peaks for the trigonal phase begin to appear in the 24 to 25° 2Θ range. As the milling time increases, there is a gradual increases in the peak intensities. Between 36 hours and 48 hours there is a large change where the 100 percent peaks for the cubic and trigonal phases

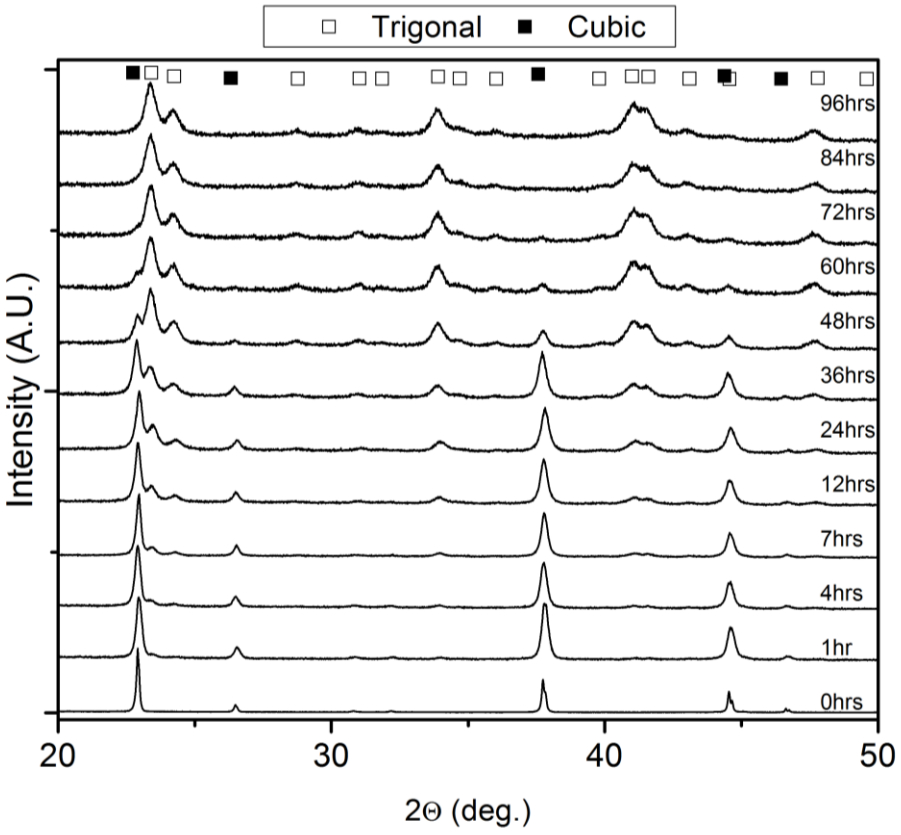

Figure B-1 The x-ray diffraction patterns of Powder 1 as the planetary ball milling time is increased. The powder begins at 0 hours with a pure cubic crystal structure.

Figure B-2 shows the amount of the metastable trigonal Mg_2Sn as a function of planetary ball milling time. The amount of trigonal fraction was calculated using Rietveld refinement of the patterns shown in Figure B-1. The fitted double Boltzmann sigmoidal curve suggests that multiple phenomena are affecting the transformation process during ball milling.

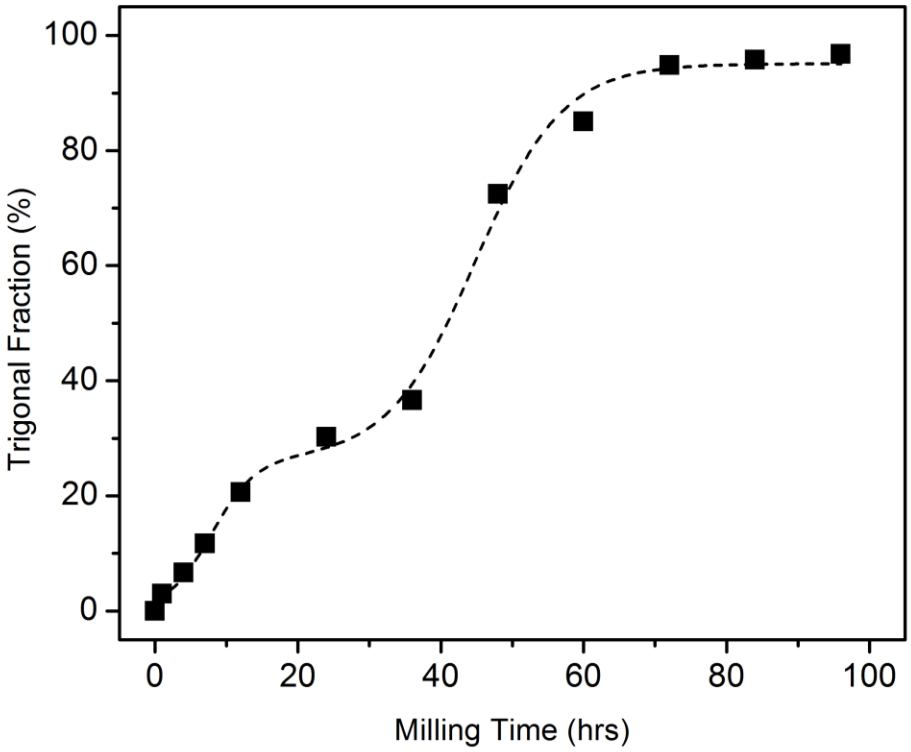

Figure B-2 The trigonal Mg_2Sn phase evolution as cubic Mg_2Sn is ball milled for a total of 96 hours. The dashed line represents a double Boltzmann sigmoid curve.

$$y = y_0 + B\left[\frac{p}{1 + e^{\frac{x-x_1}{k_1}}} + \frac{1-p}{1 + e^{\frac{x-x_2}{x_2}}}\right] \tag{B.1}$$

where y_0 is the starting amount of trigonal fraction, B is the final trigonal value, p is the ratio of the two Bolzmann sigmoidal curves, x_1 is the center point of the first sigmoid, x_2 is the center point value of the second sigmoid, k_1 and k_2 are the slopes of sigmoid 1 and 2 respectively. The double sigmoidal trend of the transformation from cubic to trigonal Mg_2Sn implies that a two-step process is taking place. A natural conclusion can be that the nucleation and growth dominated steps take place separately compared to a traditional

Kolmogorov-Johnson-Mehl-Avrami (KJMA) equation. The KJMA model was derived for an isotropic solid case of transformation. The transformation which takes place during the ball milling occurs in loosely packed powder. We must also consider that the grain size and lattice strain of the material is constantly evolving during the milling process as evidenced by the XRD peak broadening in Figure B-1.

Appendix C. Effect of CAPAD Pressure

The effect of processing pressure was also investigated on the transformation of the cubic to trigonal Mg_2Sn. Although cubic Mg_2Sn has been investigated through powder consolidation routes such as hot pressing and spark plasma sintering, there have been no reports on the trigonal phase [7], [8].

Heat treated cubic Mg_2Sn powder was low energy ball milled and passed through a 325 mesh sieve to ensure a uniform particulate size. This powder was loaded into a graphite die and plunger setup described in Chapter 2.2.2. The mechanical load was varied to produce pressures ranging from 56 to 112 MPa and processing temperatures ranged from 500 to 650 °C.

Figure C-1 shows the amount of transformation from cubic to trigonal Mg_2Sn as a function of processing temperature and pressures using XRD analysis. At 500 °C and 112 MPa there is no evidence of the trigonal phase while processing at 550 °C shows 4% of

the trigonal phase. This transition temperature where the trigonal phase begins forming is also seen at pressures of 84 MPa and 56 MPa at 600 °C and 650 °C respectively.

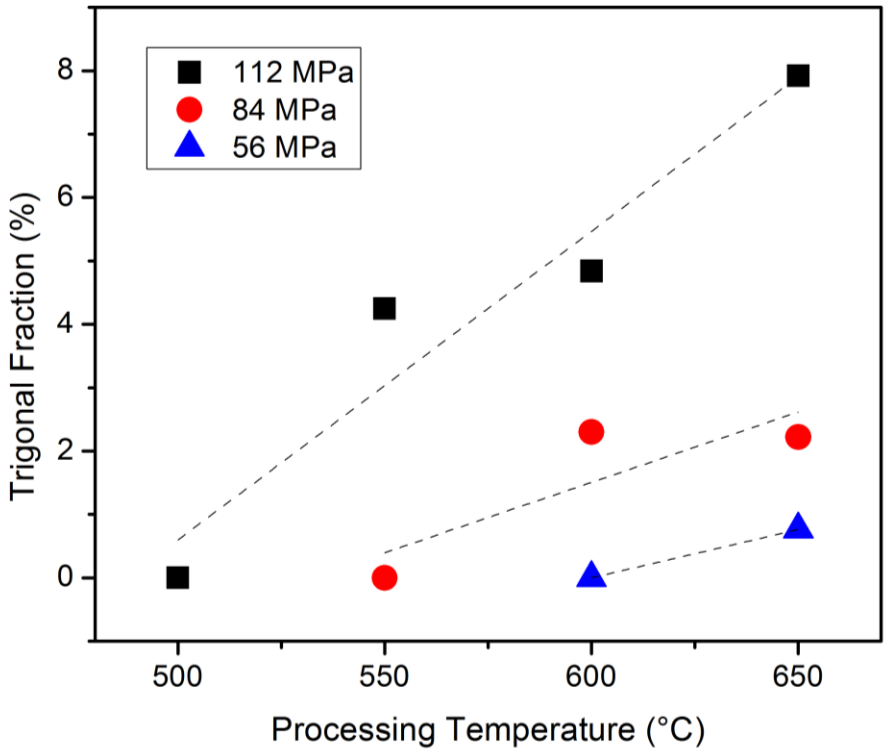

Figure C-1 CAPAD processing of heat treated cubic Mg_2Sn powder. The amount of the trigonal phase increases with increasing pressure and temperature. The dashed lines are to guide the eye.

Appendix D. Effect of CAPAD Heating Current

The effect of current on the transformation from cubic to trigonal Mg_2Sn was also considered. Because the graphite mold acts as both container and heater to the material, it is often difficult to isolate the material from the heating current. The phenomenon known

as electromigration is prevalent in the semiconductor industry where high current densities induce more diffusion and degrade the electronic circuits. In the report given by Anselmi-Tamburini [40], the amount of current flowing through the material system during the densification process effects the reaction kinetics and diffusion.

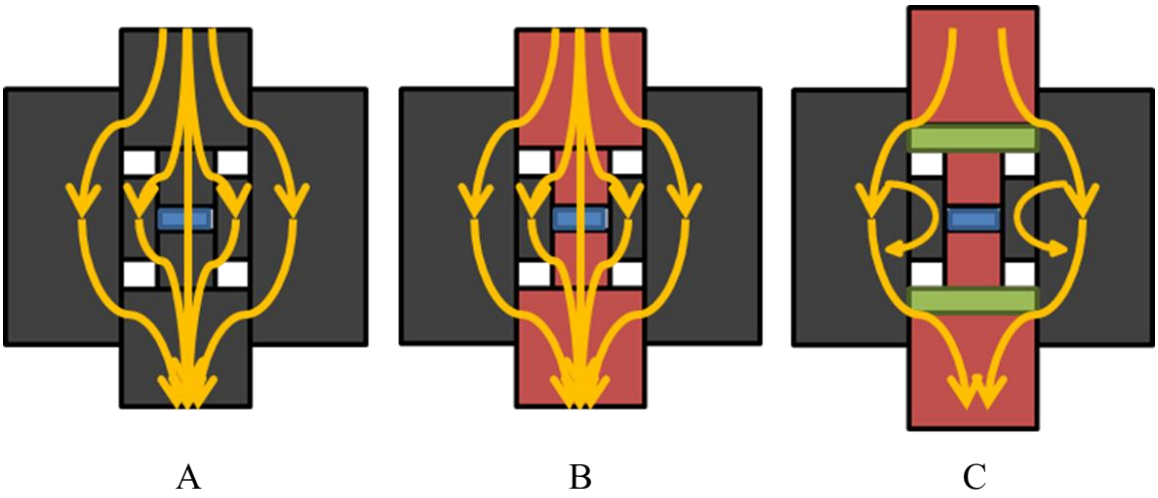

Figure D-1 Three separate die and plunger configurations with estimated electrical current paths through the system. Configuration A is the regular graphite (black) mini system setup. Configuration B replaces the graphite plungers with Co-WC plungers (red). Configuration C introduces alumina spacers (green) in order to divert the majority of the electrical current around the mini system.

Cobalt bonded tungsten carbide (Co-WC) plungers (Centennial carbide) were used in place of graphite for some experiments in order to vary the amount of current through the system (Figure D-1). Co-WC (6% Co) has been reported to have an electrical resistivity of 200 nΩ.m [99] while graphite (Ohio carbon blank) has a reported electrical resistivity of 13 μΩ.m. The amount of electrical current flowing through the Co-WC system in Figure D-1, B should be greater than configurations A and B due to Co-WC's

smaller electrical resistivity. Each sample was heated at a rate of 200 °C/min at a pressure of 112 MPa up to a temperature of 425 °C and immediately cooled to room temperature at a similar rate.

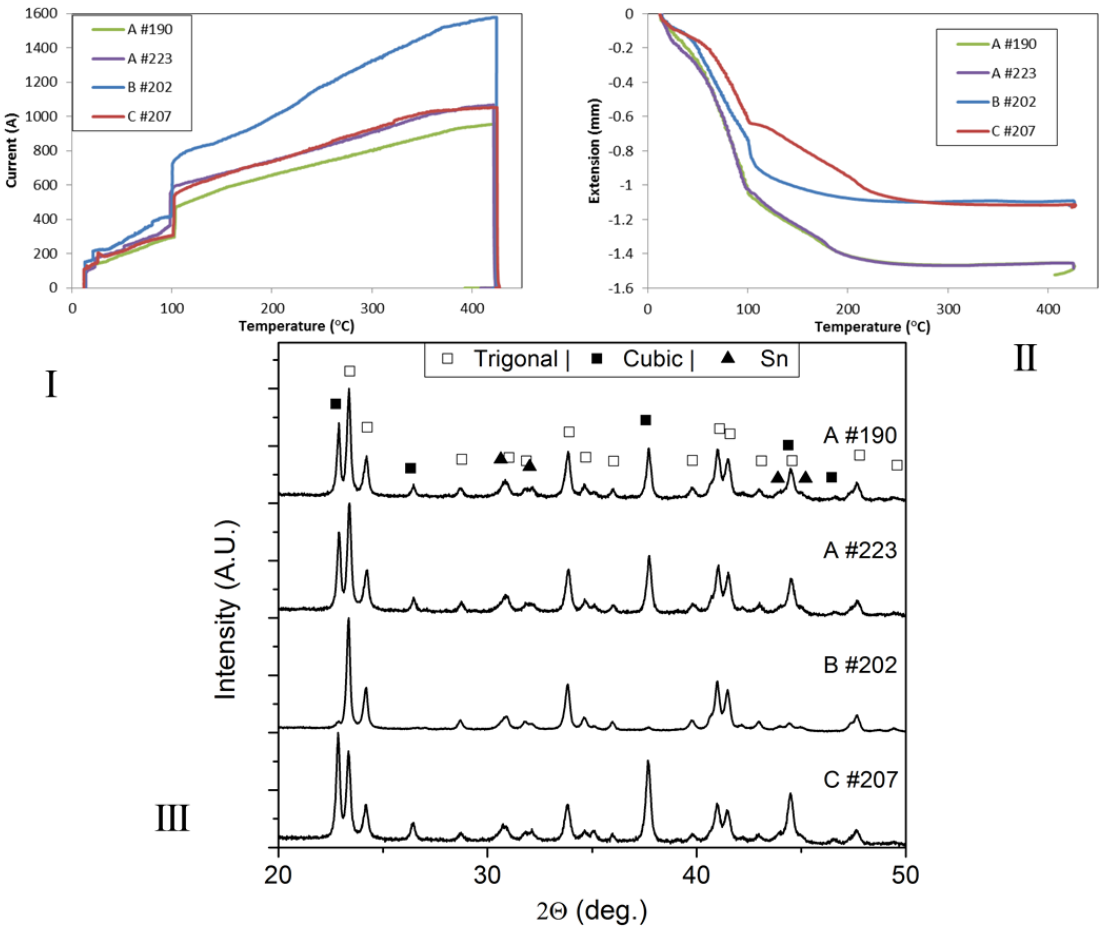

Figure D-2 I) The amount of heating current vs processing temperature for each of configurations A, B, and C. II) The overall extension vs processing temperature of each configuration. III) XRD plots of the samples after processing.

Figure D-2 I) shows the amount of heating current used to heat the samples up to a temperature of 425 C, II) shows the amount of powder displacement measured by the

extension of the CAPAD device, III) are the XRD plots showing the phase compositions of the samples made using the different configurations described in Figure D-1. Two samples were made using configuration A (A #190 and A #223) to establish the all graphite plunger and die setup and one sample each was made using configurations B (B #202) and C (C #207). The amount of heating current (Figure D-2 I)) used for each configuration varies, configurations A and C use about 900 to 1000 Amperes while configuration B uses a maximum of 1600 Amperes. The extension curves (Figure D-2 II)) are also quite different. The extension curves using configuration A are identical, C has a similar trend to A with an offset, while B is completely different showing an aggressive slope at 100 °C. The XRD plots (Figure D-2 III)) show that two samples using configuration A (A #190 and A #223) are extremely similar in terms of trigonal and cubic Mg_2Sn diffraction peaks, B #202 shows a mainly trigonal crystal structure, while C #207 shows more cubic diffraction intensity than trigonal diffraction intensity.

In the limiting case where all of the electrical current flows through the sample, the maximum current densities are 1404 and 2247 A/cm^2, for A #223 and B #202, respectively. However, it is likely that the majority of the current flows through the graphite die due to its larger cross sectional area.

While the current density through the sample cannot be accurately determined at this time, the heating current on the entire system effects the transformation of the cubic to trigonal Mg_2Sn at a pressure of 112 MPa and temperature of 425 °C. A higher amount of heating current shows a greater amount of transformation to the trigonal structure.

References

[1] D. H. Kang, S. S. Park, and N. J. Kim, “Development of creep resistant die cast Mg-Sn-Al-Si alloy,” *Mater. Sci. Eng. A*, vol. 413–414, pp. 555–560, 2005.

[2] X. Xia, A. A. Luo, and D. S. Stone, “Precipitation Sequence and Kinetics in a Mg-4Sm-1Zn-0.4 Zr (wt%) alloy,” *J. Alloys Compd.*, vol. 649, pp. 649–655, 2015.

[3] H. C. Zhong, H. Wang, L. Z. Ouyang, and M. Zhu, “Microstructure and hydrogen storage properties of Mg-Sn nanocomposite by mechanical milling,” *J. Alloys Compd.*, vol. 509, no. 11, pp. 4268–4272, 2011.

[4] V. Zaitsev, M. Fedorov, E. Gurieva, I. Eremin, P. Konstantinov, a. Samunin, and M. Vedernikov, “Highly effective Mg2Si1−xSnx thermoelectrics,” *Phys. Rev. B*, vol. 74, no. 4, pp. 2–6, Jul. 2006.

[5] S.-M. Choi, T. H. An, W.-S. Seo, C. Park, I.-H. Kim, and S.-U. Kim, “Doping Effects on Thermoelectric Properties in the Mg2Sn System,” *J. Electron. Mater.*, vol. 41, no. 6, pp. 1071–1076, 2012.

[6] H. Y. Chen and N. Savvides, “Eutectic Microstructure and Thermoelectric Properties of Mg2Sn,” *J. Electron. Mater.*, vol. 39, no. 9, pp. 1792–1797, Mar. 2010.

[7] R. B. Song, T. Aizawa, and J. Q. Sun, “Synthesis of Mg2Si1−xSnx solid solutions as thermoelectric materials by bulk mechanical alloying and hot pressing,” *Mater. Sci. Eng. B*, vol. 136, no. 2–3, pp. 111–117, Jan. 2007.

[8] M. Riffel and J. Schilz, “Mechanically alloyed Mg 2 Si/sub 1-x/Sn x solid solutions as thermoelectric materials,” *Thermoelectr. 1996., Fifteenth …*, pp. 4–7, 1996.

[9] J. M. Eldridge, E. Miller, and K. L. Komarek, “Thermodynamic properties of magnesium tin alloys by an improved isopiestic method,” *AIME MET SOC TRANS*, vol. 236, no. 1, pp. 114–121, 1966.

[10] G. Grube, “On the alloys of magnesium with tin and thallium,” *Zeitschrift fur Anorg. Chemie*, vol. 46, pp. 76–84, 1905.

[11] N. S. Kurnakow and N. J. Stepanow, “Über die Legierungen des Magnesiums mit Zinn und Blei,” *Zeitschrift für Anorg. Chemie*, vol. 46, no. 1, pp. 177–192, Aug.

1905.

[12] W. Hume-Rothery, “The system magnesium-tin and the compound Mg4Sn2,” *J. Inst. Met.*, vol. 35, pp. 336–347, 1926.

[13] W. Hume-Rothery, “Researches on Intermetallic Compounds. VI.-The Reaction Between Solid Magnesium and Liquid Tin,” *J. Inst. Met.*, vol. 38, pp. 127–131, 1927.

[14] A. Nayeb-Hashemi and J. Clark, “The Mg-Sn (Magnesium-Tin) system,” *J. Phase Equilibria*, vol. 5, no. 5, pp. 466–476, 1984.

[15] P. von Sustschinsky, “XIII. Untersuchung einiger künstlich dargestellten Verbindungen,” *Zeitschrift für Krist. - Cryst. Mater.*, vol. 38, no. 1–6, Jan. 1904.

[16] G. H. Grosch and K.-J. Range, “Studies on AB2-type intermetallic compounds, I. Mg2Ge and Mg2Sn: single-crystal structure refinement and ab initio calculations,” *J. Alloys Compd.*, vol. 235, no. 2, pp. 250–255, Mar. 1996.

[17] G. Busch and U. Winkler, “Elektrische Leitfahigkeit von Mischkristallen Intermetallischer Verbindungen,” *Helv. Phys. Acta*, vol. 26, no. 6, pp. 578–583, 1953.

[18] U. Winkler, “Electrical Properties of the Intermetallic Compounds Mg2Si, Mg2Ge, Mg2Sn, Mg2Pb,” *Helv. Phys. Acta*, vol. 28, no. 633, 1955.

[19] X. Su, F. Fu, Y. Yan, G. Zheng, T. Liang, Q. Zhang, X. Cheng, D. Yang, H. Chi, X. Tang, Q. Zhang, and C. Uher, “Self-propagating high-temperature synthesis for compound thermoelectrics and new criterion for combustion processing,” *Nat. Commun.*, vol. 5, p. 4908, 2014.

[20] W. Seith and O. Kubaschewski, “The heats of formation of several alloys,” *Z. Elektrochem*, 1937.

[21] O. Kubaschewski and A. Walter, “Experience and Results of High-Temperature Calorimetry of Alloys,” *Z. Elektrochem*, vol. 45, no. 9, pp. 732–740, 1939.

[22] A. Borsese, G. Borzone, R. Ferro, and R. Capelli, “Heat of Formation of Mg-Sn Alloys,” *Zeitschrift fur Met.*, vol. 66, no. 4, pp. 226–227, 1975.

[23] J. Sommer, J. J. Lee, and B. Predel, “Temperature Dependence of the Mixing Enthalpies of Liquid Magnesium-Lead and MAgnesium-Tin Alloys,” *Zeitschrift*

fur Met., vol. 71, no. 12, pp. 818–821, 1980.

[24] B. I. Boltaks, "The nature of electrochemical and magnetic properties of the intermetallic bonded Mg2Sn," *ZHURNAL TEKHNICHESKOI Fiz.*, vol. 20, no. 2, pp. 180–192, 1950.

[25] W. D. LAWSON, S. NIELSEN, E. H. PUTLEY, and V. ROBERTS, "XXV. The Preparation, Electrical and Optical Properties of Mg $_2$ Sn," *J. Electron. Control*, vol. 1, no. 2, pp. 203–211, 1955.

[26] J. J. Martin, "Thermal Conductivity of Mg2Si, Mg2Ge, and Mg2Sn," *J. Phys. Chem*, vol. 33, pp. 1139–1148, 1972.

[27] J. Martin and G. Danielson, "Thermal Conductivity of Magnesium Stannide from 4 to 300° K," *Phys. Rev.*, vol. 166, no. 15, 1968.

[28] P. Cannon and E. T. Conlin, "Magnesium Compounds: New Dense Phases," *Science (80-.).*, vol. 145, no. 3631, pp. 487–489, Jul. 1964.

[29] T. Dyuzheva, S. Kabalkina, and L. Vereshchagin, "Polymorphism of Mg 2 Sn at High Temperatures and Pressures," *Kristallografiya*, vol. 17, no. 4, pp. 804–811, 1972.

[30] K.-J. Range, G. H. Grosch, and M. Andratschke, "Studies on AB2-type intermetallic compounds. Part V1. The crystal structure of Mg9Sn5, a supposed high-pressure modification of Mg2Sn," *J. Alloys Compd.*, vol. 244, no. 1–2, pp. 170–174, Nov. 1996.

[31] N. Bolotina and T. Dyuzheva, "Growth of crystals, composite crystal structures and electrical resistance of high-pressure phases of Mg 2 B 1+ x(B= Sn, Ge)," *J. Alloys Compd.*, vol. 278, pp. 29–33, 1998.

[32] R. Abbaschian, H. Zhu, and C. Clarke, "High pressure-high temperature growth of diamond crystals using split sphere apparatus," *Diam. Relat. Mater.*, vol. 14, no. 11–12, pp. 1916–1919, 2005.

[33] V. N. Strekalov, "Lindeman's criterion: diamond graphitization temperature and its dependence on external pressure," pp. 3–8, Aug. 2012.

[34] M. Abdellaoui and E. Gaffet, "Mechanical alloying in a planetary ball mill : kinematic description," *Le J. Phys. IV*, vol. 04, no. C3, pp. C3–291–C3–296, Feb. 1994.

[35] J. E. Garay, “Current-Activated, Pressure-Assisted Densification of Materials,” *Annu. Rev. Mater. Res.*, vol. 40, no. 1, pp. 445–468, Jun. 2010.

[36] Y.-M. Chiang, D. P. I. Birnie, and W. D. Kingery, *Physical Ceramics*. New York: John Wiley & Sons, Inc., 1997.

[37] Z. Shen, M. Johnsson, Z. Zhao, and M. Nygren, “Spark plasma sintering of alumina,” *J. Am. Ceram. Soc.*, vol. 85, no. 8, pp. 1921–1927, 2002.

[38] J. E. Alaniz, A. D. Dupuy, Y. Kodera, and J. E. Garay, “Effects of applied pressure on the densification rates in current-activated pressure-assisted densification (CAPAD) of nanocrystalline materials,” *Scr. Mater.*, vol. 92, pp. 7–10, 2014.

[39] J. E. Garay, U. Anselmi-Tamburini, and Z. a. Munir, “Enhanced growth of intermetallic phases in the Ni-Ti system by current effects,” *Acta Mater.*, vol. 51, pp. 4487–4495, 2003.

[40] U. Anselmi-Tamburini, J. E. Garay, and Z. A. Munir, “Fundamental investigations on the spark plasma sintering/synthesis process: III. Current effect on reactivity,” *Mater. Sci. Eng. A*, vol. 407, no. 1–2, pp. 24–30, 2005.

[41] U. Anselmi-Tamburini, S. Gennari, J. E. Garay, and Z. A. Munir, “Fundamental investigations on the spark plasma sintering/synthesis process: II. Modeling of current and temperature distributions,” *Mater. Sci. Eng. A*, vol. 394, no. 1–2, pp. 139–148, Mar. 2005.

[42] W. Friedrich, P. Knipping, and M. V Laue, “Interference phenomena with Röntgen rays,” *Sitzber. Math-phys. Kl. bayer. Akad. Wiss. Manche*, vol. 22, p. 303, 1912.

[43] H. M. Rietveld, “Line profiles of neutron powder-diffraction peaks for structure refinement,” *Acta Crystallogr.*, vol. 22, no. 1, pp. 151–152, 1967.

[44] H. M. Rietveld, “The crystal structure of some alkaline earth metal uranates of the type M 3 UO 6,” *Acta Crystallogr.*, vol. 20, no. 4, pp. 508–513, 1966.

[45] H. M. Rietveld, “A profile refinement method for nuclear and magnetic structures,” *J. Appl. Crystallogr.*, vol. 2, no. 2, pp. 65–71, 1969.

[46] A. Larson and R. Von Dreele, “GSAS - General Structure Analysis System, Los Alamos National Laboratory Report No. LAUR 86-748,” Los Alamos, NM, 2000.

[47] L. Lutterotti, D. Chateigner, S. Ferrari, and J. Ricote, “Texture, residual stress and

structural analysis of thin films using a combined X-ray analysis," *Thin Solid Films*, vol. 450, no. 1, pp. 34–41, 2004.

[48] J. Rodríguez-carvajal, *Recent developments for the program FULLPROF*, vol. December 2, no. 26. 2001.

[49] J. BETHIN and W. S. WILLIAMS, "Ambipolar Diffusion Contribution to High-Temperature Thermal Conductivity of Titanium Carbide," *J. Am. Ceram. Soc.*, vol. 60, no. 9–10, pp. 424–427, Sep. 1977.

[50] R. T. Delves, "Thermomagnetic effects in semiconductors and semimetals," *Reports Prog. Phys.*, vol. 28, no. 1, pp. 249–289, 1965.

[51] H. J. Goldsmid, "Transport effects in semi-metals and narrow-gap semiconductors," *Adv. Phys.*, vol. 14, no. 55, pp. 273–326, 1965.

[52] G. S. Rohrer, M. Affatigato, M. Backhaus, R. K. Bordia, H. M. Chan, S. Curtarolo, A. Demkov, J. N. Eckstein, K. T. Faber, J. E. Garay, Y. Gogotsi, L. Huang, L. E. Jones, S. V. Kalinin, R. J. Lad, C. G. Levi, J. Levy, J.-P. Maria, L. Mattos, A. Navrotsky, N. Orlovskaya, C. Pantano, J. F. Stebbins, T. S. Sudarshan, T. Tani, and K. Scott Weil, "Challenges in Ceramic Science: A Report from the Workshop on Emerging Research Areas in Ceramic Science," *J. Am. Ceram. Soc.*, vol. 95, no. 12, pp. 3699–3712, Dec. 2012.

[53] T. Dyuzheva, N. Bendeliani, L. Dzhavadov, T. Kolobyanina, and N. Nikolaev, "Crystal growth of the high-pressure phase of Mg 2 Sn," *J. Alloys Compd.*, vol. 223, pp. 74–76, 1995.

[54] H. T. Hall, "Ultra-high-pressure, high-temperature apparatus: The 'belt,'" *Rev. Sci. Instrum.*, vol. 31, no. 2, pp. 125–131, 1960.

[55] C. Clark, C. Wright, C. Suryanarayana, E. G. Baburaj, and F. H. Froes, "Synthesis of Mg2X (X = Si, Ge, or Sn) intermetallics by mechanical alloying," *Mater. Lett.*, vol. 33, no. 1–2, pp. 71–75, Nov. 1997.

[56] J. Schilz, M. Riffel, and K. Pixius, "Synthesis of thermoelectric materials by mechanical alloying in planetary ball mills," *Powder Technol.*, vol. 105, no. 1–3, pp. 149–154, Nov. 1999.

[57] G. Urretavizcaya and G. Meyer, "Metastable hexagonal Mg2Sn obtained by mechanical alloying," *J. Alloys Compd.*, vol. 339, no. 1–2, pp. 211–215, Jun. 2002.

[58] R. Janot, F. Cuevas, M. Latroche, and a. Percheron-Guégan, “Influence of crystallinity on the structural and hydrogenation properties of Mg2X phases (X=Ni, Si, Ge, Sn),” *Intermetallics*, vol. 14, no. 2, pp. 163–169, Feb. 2006.

[59] H. Kim, Y.-J. Kim, D. G. Kim, H.-J. Sohn, and T. Kang, “Mechanochemical synthesis and electrochemical characteristics of Mg2Sn as an anode material for Li-ion batteries,” *Solid State Ionics*, vol. 144, no. 1–2, pp. 41–49, Sep. 2001.

[60] C. Suryanarayana, “Mechanical alloying and milling,” *Prog. Mater. Sci.*, vol. 46, no. 1–2, pp. 1–184, Jan. 2001.

[61] S. K. Bux, M. T. Yeung, E. S. Toberer, G. J. Snyder, R. B. Kaner, and J.-P. Fleurial, “Mechanochemical synthesis and thermoelectric properties of high quality magnesium silicide,” *J. Mater. Chem.*, vol. 21, no. 33, p. 12259, 2011.

[62] U. Anselmi-Tamburini, J. E. Garay, and Z. A. Munir, “Fast low-temperature consolidation of bulk nanometric ceramic materials,” *Scr. Mater.*, vol. 54, no. 5, pp. 823–828, Mar. 2006.

[63] T. Proffen, T. Egami, S. J. L. Billinge, A. K. Cheetham, D. Louca, and J. B. Parise, “Building a high resolution total scattering powder diffractometer – upgrade of NPD at MLNSC,” vol. 165, pp. 163–165, 2002.

[64] R. B. Von Dreele, J. D. Jorgensen, and C. G. Windsor, “Rietveld refinement with spallation neutron powder diffraction data,” *J. Appl. Crystallogr.*, vol. 15, no. 6, pp. 581–589, Dec. 1982.

[65] K. Seifert, “Pressure Crystal Chemistry of AX 2 Compounds,” *Fortschr. Miner.*, vol. 45, pp. 214–280, 1967.

[66] V. Zaitsev, “Thermoelectrics on the Base of Solid Solutions of Mg2BIV Compounds (BIV = Si, Ge, Sn),” in *Thermoelectrics Handbook*, vol. 2, CRC Press, 2005, pp. 29–1–29–12.

[67] A. Y. Fong, H. Xu, K. Page, M. R. Dirmyer, Y. Kodera, S. J. Obrey, and J. E. Garay, “Synthesis and structural characterization of dense polycrystalline Mg9Sn5 , a metastable Mg–Sn phase,” *J. Alloys Compd.*, vol. 616, pp. 333–339, 2014.

[68] M. S. Dresselhaus, G. Chen, M. Y. Tang, R. G. Yang, H. Lee, D. Z. Wang, Z. F. Ren, J.-P. Fleurial, and P. Gogna, “New Directions for Low-Dimensional Thermoelectric Materials,” *Adv. Mater.*, vol. 19, no. 8, pp. 1043–1053, Apr. 2007.

[69] Brian H. Toby, “EXPGUI, a graphical user interface for GSAS,” *J. Appl. Cryst.*, vol. 34, pp. 210–213, 2001.

[70] L. Pauling, “The Crystal Structure of Magnesium Stannide,” *J. Am. Chem. Soc.*, vol. 45, no. 12, pp. 2777–2780, Dec. 1923.

[71] R. Orrù, J. Woolman, G. Cao, and Z. A. Munir, “Synthesis of dense nanometric MoSi2 through mechanical and field activation,” *J. Mater. Res.*, vol. 16, no. 05, pp. 1439–1448, May 2001.

[72] J. Farjas and P. Roura, “Modification of the Kolmogorov – Johnson – Mehl – Avrami rate equation for non-isothermal experiments and its analytical solution,” *Acta Mater.*, vol. 54, pp. 5573–5579, 2006.

[73] P. W. M. Jacobs and F. C. Tompkins, “Classification and Theory of Solid Reactions,” in *Chemistry of the Solid State*, W. E. Garner, Ed. London: Butterworths Scientific Publications, 1955, pp. 184–212.

[74] R. D. Shannon and J. A. Pask, “Kinetics of the Anatase-Rutile Transformation,” *J. Am. Ceram. Soc.*, vol. 48, no. 8, pp. 391–398, 1965.

[75] M. Avrami, “Kinetics of Phase Change. I General Theory,” *J. Chem. Phys.*, vol. 7, no. 12, p. 1103, 1939.

[76] M. Avrami, “Kinetics of Phase Change. II Transformation-Time Relations for Random Distribution of Nuclei,” *J. Chem. Phys.*, vol. 8, no. 2, p. 212, 1940.

[77] P. Shewmon and F. Rhines, “Rate of self-diffusion in polycrystalline magnesium,” *J. Met.*, 1954.

[78] C. Coston and N. H. Nachtrieb, “Self-Diffusion in Tin at High Pressure,” *J. Phys. Chem.*, vol. 68, no. 8, pp. 2219–2229, 1964.

[79] Y. Oishi, Y. Kamei, M. Akiyama, and T. Yanagi, “Self-diffusion coefficient of lithium in lithium oxide,” *J. Nucl. Mater.*, vol. 87, no. 2–3, pp. 341–344, 1979.

[80] J. R. Sootsman, D. Y. Chung, and M. G. Kanatzidis, “New and old concepts in thermoelectric materials,” *Angew. Chemie - Int. Ed.*, vol. 48, no. 46, pp. 8616–8639, 2009.

[81] E. Penilla, Y. Kodera, and J. Garay, “Simultaneous synthesis and densification of transparent, photoluminescent polycrystalline YAG by current activated pressure

assisted densification (CAPAD)," *Mater. Sci. Eng. B*, 2012.

[82] Z. Wang, J. E. Alaniz, W. Jang, J. E. Garay, and C. Dames, "Thermal conductivity of nanocrystalline silicon: importance of grain size and frequency-dependent mean free paths.," *Nano Lett.*, vol. 11, no. 6, pp. 2206–13, Jun. 2011.

[83] R. Blunt, H. Frederikse, and W. Hosler, "Electrical and Optical Properties of Intermetallic Compounds. IV. Magnesium Stannide," *Phys. Rev.*, vol. 571, no. 1954, 1955.

[84] H. G. Lipson and A. Kahan, "Infrared Absorption of Magnesium Stannide," *Phys. Rev.*, vol. 133, no. 3A, pp. A800–A810, Feb. 1964.

[85] F. Vazquez, R. Forman, and M. Cardona, "Electroreflectance Measurements on Mg 2 Si, Mg 2 Ge, and Mg 2 Sn," *Phys. Rev.*, vol. 176, no. 3, pp. 905–908, 1968.

[86] B. D. Lichter, "Electrical Properties of Mg[sub 2]Sn Crystals Grown from Nonstoichiometric Melts," *J. Electrochem. Soc.*, vol. 109, no. 9, p. 819, 1962.

[87] J. S. Rhyee, E. Cho, K. Ahn, K. H. Lee, and S. M. Lee, "Thermoelectric properties of bipolar diffusion effect on In4 Se3-xTex compounds," *Appl. Phys. Lett.*, vol. 97, no. 15, pp. 95–98, 2010.

[88] W.-S. Liu, B.-P. Zhang, J.-F. Li, H.-L. Zhang, and L.-D. Zhao, "Enhanced thermoelectric properties in CoSb[sub 3-x]Te[sub x] alloys prepared by mechanical alloying and spark plasma sintering," *J. Appl. Phys.*, vol. 102, no. 10, p. 103717, 2007.

[89] E. Toberer, C. Cox, and S. Brown, "Traversing the Metal- • Insulator Transition in a Zintl Phase: Rational Enhancement of Thermoelectric Efficiency in Yb14Mn1-xAlxSb11," *Adv. Funct. ...*, pp. 2795–2800, 2008.

[90] B. Poudel, Q. Hao, Y. Ma, Y. Lan, A. Minnich, B. Yu, X. Yan, D. Wang, A. Muto, D. Vashaee, X. Chen, J. Liu, M. S. Dresselhaus, G. Chen, and Z. Ren, "High-Thermoelectric Performance of Nanostructured Bismuth Antimony Telluride Bulk Alloys," *Science (80-.).*, vol. 320, no. 5876, pp. 634–638, May 2008.

[91] H. Ning, G. D. Mastrorillo, salvatore Grasso, B. Du, T. Mori, C. HU, Y. Xu, kevin Simpson, G. Maizza, and M. Reece, "Enhanced Thermoelectric Performance of Porous Magnesium Tin Silicide Prepared using Pressure-less Spark Plasma Sintering," *J. Mater. Chem. A*, pp. 17426–17432, 2015.

[92] W. Liu, X. Tan, K. Yin, H. Liu, X. Tang, J. Shi, Q. Zhang, and C. Uher, "Convergence of conduction bands as a means of enhancing thermoelectric performance of n-type Mg 2Si 1-xSn x solid solutions," *Phys. Rev. Lett.*, vol. 108, no. 16, pp. 1–5, 2012.

[93] H. J. Goldsmid, "Transport effects in semi-metals and narrow-gap semiconductors," *Adv. Phys.*, vol. 14, no. 55, pp. 273–326, Jul. 1965.

[94] J.-H. Bahk, Z. Bian, and A. Shakouri, "Electron transport modeling and energy filtering for efficient thermoelectric Mg 2 Si 1 −x Sn x solid solutions," *Phys. Rev. B*, vol. 89, no. 7, p. 075204, Feb. 2014.

[95] K. Yin, Q. Zhang, Y. Zheng, X. Su, X. Tang, and C. Uher, "Thermal stability of Mg 2 Si 0.3 Sn 0.7 under different heat treatment conditions," *J. Mater. Chem. C*, vol. 3, no. 40, pp. 10381–10387, 2015.

[96] C. Wood, "Materials for thermoelectric energy conversion," *Reports Prog. Phys.*, vol. 51, no. 4, pp. 459–539, Apr. 1988.

[97] J. P. Heremans, M. S. Dresselhaus, L. E. Bell, and D. T. Morelli, "When thermoelectrics reached the nanoscale," *Nat. Nanotechnol.*, vol. 8, no. July, pp. 471–473, 2013.

[98] W. D. Robertson and H. H. Uhlig, "Chemical Properties of the Intermetallic Compounds Mg[sub 2]Sn and Mg[sub 2]Pb," *J. Electrochem. Soc.*, vol. 96, no. 1, p. 27, 1949.

[99] Y. C. Lin, L. R. Hwang, C. H. Cheng, and P. L. Su, "Effects of electrical discharge energy on machining performance and bending strength of cemented tungsten carbides," *J. Mater. Process. Technol.*, vol. 206, no. 1–3, pp. 491–499, 2008.